

BEng (Hons) Electrical and Electronic Engineering
Final Year Project Report

Name: Wael Mahlous

ID: 100143166, **e-mail:** w.mahlous@se10.qmul.ac.uk

Project Supervisor: Dr Robert Donnan

Project Title: *Application of a Transmissometer for the Refractive Index Study of Dental Enamel at IR energies*

Abstract

PURPOSE: Dental erosion, which is results from the direct attack by acids on the outer enamel layer on the teeth causing it to lose minerals (de-mineralisation), is a widespread medical condition affecting all age categories. Despite being a very common condition, methods of its early detection are limited. This has led to an increased interest in developing methods for early discovery to aid dentists in the prevention of this condition before it is too late.

A recent publication has found strong, linear positive correlations between the mineral content of enamel and its refractive index measured using Optical Coherence Tomography (OCT) [1]. One of the research projects at the School of Medicine and Dentistry department at QMUL is to build a hand-held OCT probe which can be inserted directly into the patient's mouth to obtain 3D images of the teeth. Images can tell a lot about the extent of mineral loss, if there's any, which can allow the dentist to suggest dietary changes to the patient or give them general advice on how to prevent tooth erosion. One of the challenges in making this probe is that of accurately quantifying the mineral loss and associating it with the images.

This project aims to establish whether or not a quasi-optical circuit operating in the millimetre-wave range and driven by a Vector Network Analyser (VNA), which has been used to measure dielectric properties (one of which is refractive index) for decades, can be used to detect mineral changes in enamel samples. If detection is possible with the results being repeatable and within sustainable error, refractive index measurements using this technique can be used to provide a quantitative measure of the mineral content in enamel. Raw data from OCT which is used to form the images can also be used to measure refractive index and thus results from both techniques could be compared in the future and linked to OCT images for use in the probe to detect mineral loss.

METHOD: 4 experiments were conducted, out of which the main one was: Bovine enamel samples supplied by GlaxoSmithKline were treated with a 1 % concentration, 3.5 pH Citric Acid solution and used for the measurements. The 3 samples were measured first without the addition of acid. After that measurements were taken throughout a 5 hour period while varying the volume of acid applied and the time it was left to set before wiping it off and taking the next measurement.

RESULTS: After every experiment S-parameter data (which is a direct output of the measurements by the VNA) were processed through Matlab scripts, which were written specifically for this project, that implement a least squares algorithm to obtain the frequency-dependent refractive index by comparing the measured data to user-defined theoretical data. Writing these codes took a considerable amount of time in this project because of the relative novelty of the programming method used. The refractive index graphs showed variations which couldn't be possibly linked to the de-mineralising effects of acid due to the absence of a trend in the results.

CONCLUSION: Analysing the results and re-tracing the experimental procedure identified possible reasons why the mineral loss in the enamel samples couldn't be detected, of which the main 'suspects' were: **1)** the samples being too thick, **2)** the frequency test range being too small, **3)** the significant errors in the measurement results due to the presence of standing waves (caused by the relatively large thickness of the samples) in the quasi-optical circuit which could have been reduced if directional couplers to suppress the standing waves were available.

Table of Contents

Abstract.....	1
Introduction.....	3
Background Research / Literature Review.....	10
Implementation and Results.....	33
Discussion/Analysis of Results.....	69
Conclusion.....	79
References.....	81

Introduction

Two of the most common types of dental disease are **tooth decay** (caries) and **tooth erosion** [2].

DENTAL CARIES

Caries is Latin for 'rot' or 'rotten' and so 'dental caries' means rotten teeth. Caries is the noun which refers to the disease: tooth decay. It is the second most common disorder (after common cold) [3] and is one of the most widespread health problems in the UK affecting approximately 31% of adults and children starting school [4]. It is also the third most common reason for children to be admitted to hospital [5].

It can be defined as the chronic progressive deconstructive disease of hard dental tissues caused by specific bacteria. It is a reversible multifactorial process of tooth de-mineralisation and re-mineralisation. It involves enamel, dentin and cementum [6] which, combined with pulp, constitute the four main components of teeth. Enamel, which is the most highly mineralised tissue in the human body, is made up of 96% mineral and 4 % water [7].

During tooth decay, the enamel is de-mineralised, i.e. minerals are removed from it in the form of ions. This is mostly caused by acids which are a by-product of the conversion of left-over food sugars into energy by the naturally occurring oral bacteria called plaque that feed on these sugars. The human body combats this process by re-mineralising the enamel through saliva which also acts to neutralise the acids as well as to make up for the lost minerals. However, this can be a very slow process depending on the extent of the de-mineralisation which may overpower it resulting in carious (decaying) lesions in the tooth [8]. To prevent tooth decay either the de-mineralisation process should be slowed down (brushing teeth/cutting down excess sugary food intake) or the re-mineralisation process should be speeded up (by external re-mineralisation factors such as calcium or fluoridated toothpaste [9]).

Tooth decay is induced by various factors and the process that leads to it is complex and involves a vast number of stages. Researchers within the field of dentistry continue to study the caries process and devise methods of preventing and curing it. Tooth decay can be treated by restoration which is usually in the form of fillings, or by completely extracting the affected tooth [10].

DENTAL EROSION

Tooth erosion, also known as "non-carious tooth surface loss" is a less serious problem [11] and is found largely in young people [12]. Over half of all children aged 15 to 18 in the UK have some form of dental erosion [13]. It is caused by the irreversible wearing away of the enamel (and possibly the dentine layer below it) from attack by acids other than those formed by bacteria in tooth decay. These acids usually come from fizzy drinks or fruit juices, particularly those containing citric acid found naturally in lemons and oranges.

Although these two conditions are similar they are different mainly in the fact that dental erosion is often described solely as a surface phenomenon which is irreversible, unlike caries where it has been established that the destructive effects involve both the surface and the subsurface region [14].

This project specifically focuses on dental erosion due to the nature of the tests performed. Since this project is mainly an **explorative project**, erosion was chosen as it is simpler to simulate on the samples that were available. Acid was applied to the enamel samples on the surface only and left to set for some time before wiping off excess and taking the measurements, which are described later on in the report. This is similar to what happens in erosion when the outer layer of enamel on the teeth is de-mineralised. In the case of tooth decay, the acid formed by bacteria similarly softens the enamel and dissolves it away, but then proceeds to the underlying dentin and pulp destroying them and causing cavities. Sometimes the acid and bacteria reaches beneath the enamel and forms these cavities while the enamel on top gets re-mineralised.

Thus, simulating caries is a bit more complicated as it should involve both de-mineralising (acid) and re-mineralising agents (calcium/phosphate) to be studied accurately. It should also involve samples containing at least both enamel and dentine, as well as applying acid not to the whole surface but only to a small part of it in order to cause cavities. This can be realised by coating a small area with nail varnish to prevent the acid from reaching the enamel and then removing the varnish with acetone once the acid is wiped off. The de-mineralisation of enamel in erosion is also a part of decay and thus the results of the experiments in this project could be used later on for planning similar experiments for dental caries study.

Because interest in dental erosion has increased significantly over the last few years, one of the major issues that research in this area is focused on is the development of accurate diagnostic tools that can be used efficiently in the clinic to detect erosion and prevent it. A prominent research field in both caries and erosion research includes efficient ways of detecting them in their earlier stages and understanding the process which leads to them in order to improve treatment.

Below are extracts from some publications that refer to this gap in dental decay and erosion treatment:

“Review of the clinical evidence indicates that there is a need for further research on this topic, particularly on the diagnosis and prevention of dental erosion.” [15]

“A number of indices have been proposed to diagnose and quantify dental erosion, but there is a need for standardization of indices and for the development of practical diagnostic tools.” [15]

“...the first and the most important step in a preventive strategy would be the development of and training of dental professionals on techniques for the early diagnosis and monitoring of the progress of dental erosion... hence, there is a need for development of a diagnostic device, which can detect an early eroded lesion and quantifiably monitor the progress of the lesion on a longitudinal basis.” [16]

“It is now universally recognized that the development of new technologies for early detection and quantitative monitoring of dental decay at an early stage of formation could provide health and economic benefits ranging from timely preventive interventions to reduction in the time required for clinical trials of anticaries agents.” [17]

“...all these factors necessitate the need for the development of new techniques for early diagnosis of carious lesions. Researchers have been trying to develop various instruments based on optical spectroscopic techniques for detection of dental caries during the last two decades. These optical spectroscopic techniques facilitate non-invasive and real-time tissue characterization with reduced radiation exposure to patient, thereby improving the management of dental caries. Nonetheless, a cost effective optical system with adequate sensitivity and specificity for clinical use is still not realized and development of such a system is a challenging task... Recent years have seen an increase in research activity directed towards the development of several diagnostic methods, particularly in the assessment of early caries lesions.” [18]

This gap arises from the fact that current practices diagnose decay and erosion mostly based on morphological changes and/or pain in the teeth:

Tooth decay symptoms

Decay in the early stage may have no symptoms and up to a certain point they can only be visually detected by the dentist [19] who can then check for damaged areas using an instrument called an *explorer* to look for discoloured spots or holes. As the cavity deepens, patients experience toothache that intensifies upon contact with hot or cold food/beverages and swelling of the adjacent gum may occur.

Tooth erosion symptoms

Teeth start to look glazed and smooth and with time start to turn yellow due to the dissolved enamel exposing the slightly darker dentine layer below it. In the late stages of erosion chipping of the front teeth edges occurs which results in them having a square shape. Similar to tooth decay, eroding teeth experience increased sensitivity to hot or cold foods and beverages.

It is these changes that dentists recognize during check-ups or after the patient arranges an appointment due to experiencing these symptoms. In most cases by the time a carious/eroded lesion is detected it is too late and restorative measures have to be taken. Because destroyed tooth structure doesn't fully re-generate, restorative materials such as fillings and crowns are used to retain the tooth structure. Tooth erosion is more expensive to treat especially if a significant amount of enamel is lost. Cosmetic treatments such as veneers [20] can be used to replace the lost enamel and restore the tooth structure.

However, dental erosion does not always need to be treated. With regular check-ups the dentist can prevent the problem getting any worse and the erosion going any further [21]. In order to fill this gap in the clinical dentistry practice, research in the area of developing accurate diagnostic tools that can be used in the clinic to change the so-called “**restorative**” dentistry into “**preventive**” dentistry has increased in the last few years. If such a device is developed, it could be incorporated into routine check-ups in order to advise patients who exhibit enamel de-mineralisation at an early stage to change their diet in a specific manner or to take more preventative care measures in order to avoid further damage. This is largely because personal dental hygiene and diet play a significant role in both dental caries and dental erosion [22].

Some of the techniques studied and developed in the last 2 decades are listed below:

- ***Fibre-optic transillumination:*** which is based on the fact that carious (decaying) enamel has a lower index of light transmission than sound (healthy) enamel [23]. This property of enamel is used similarly in this project.
- ***Digital imaging fibre-optic transillumination.*** [24] [25] [26] [27] [28] [29]
- ***Quantitative light-induced fluorescence.*** [30] [31] [32]
- ***DIAGNOdent laser system.*** [33] [34] [35]
- ***Electrical caries monitor.*** [36] [37]
- ***Midwest Caries I.D.*** [38]
- ***Polarization-sensitive optical coherence tomography*** [39] [40] [41] [42]: Optical Coherence Tomography is the main tool used for dental caries and erosion research in the School of Medicine and Dentistry at QMUL.
- ***CarieScan.*** [43]
- ***Frequency-domain infrared photothermal radiometry and modulated luminescence.*** [44]
- ***Cone beam computed tomography.*** [45]

These methods all have their disadvantages and disadvantages, mainly related to sensitivity to small changes in mineral content and to the feasibility in using them practically [14]. Out of all these techniques, Optical Coherence Tomography based detection has proven to be very powerful in the early discovery of de-mineralisation [17].

OPTICAL COHERENCE TOMOGRAPHY

Optical coherence tomography (OCT) is a technology that has gained acceptance as a non-invasive (no damage to living tissue) method for characterizing soft tissue and other turbid media [46]. It has widely been explored for use as a diagnostic tool in clinical medicine and biomedical imaging [47], with commercial devices now available in ophthalmology [48], dermatology [49] and interventional cardiology [50]. It is maturing as a powerful imaging modality in medical and non-medical fields [51] and is becoming more and more popular in the field of biomedicine [52].

OCT is analogous to ultrasound imaging, except that it mostly uses near-infrared light instead of sound [53] [54]. OCT can provide cross-sectional images of tissue structure on the micron scale *in situ* and in real time [55]. It can capture three-dimensional images from within optical scattering media at micrometre-resolution. It uses the coherent properties of light [56] passing through samples which scatter and/or absorb electromagnetic radiation to produce the high-resolution cross-sectional images through the samples. A signal source creates a beam which is split into 2, one beam goes through the sample and the other goes to a “reference mirror”. OCT uses interferometry techniques to build these images based on the extent of the interference of light that is reflected from particles in the sample under study with incident light that is reflected from the reference mirror.

OCT has proven to be able to efficiently detect changes in bone mineral density (BMD) of bone samples, in addition to detection of differences in mineral content of de- and re-mineralised enamel samples. Minerals in enamel play the same role in tooth decay as they do in bones. A reduction of BMD leads to a bone disease called osteoporosis which causes the risks of bone fracture to be highly increased. Thus a measurement of the mineral content in enamel/bone can tell whether decay/erosion/osteoporosis is occurring and give an indication on what stage it is in. The figures below show graphs from two such research efforts, one with enamel and the other with bone. De- and re-mineralised samples studied under OCT have distinct differences in light penetration through the sample (**Figure 2**).

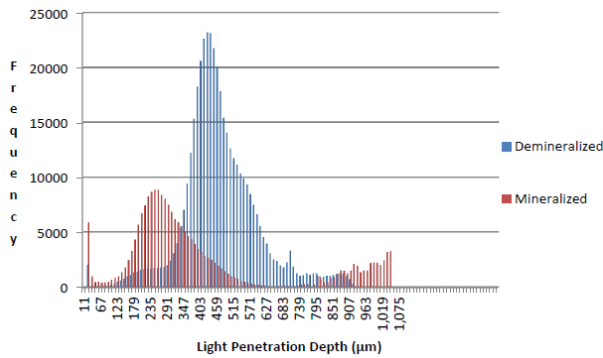


Figure 1 [57]: The large difference in the depth of light penetration in mineralised and de-mineralised bone.

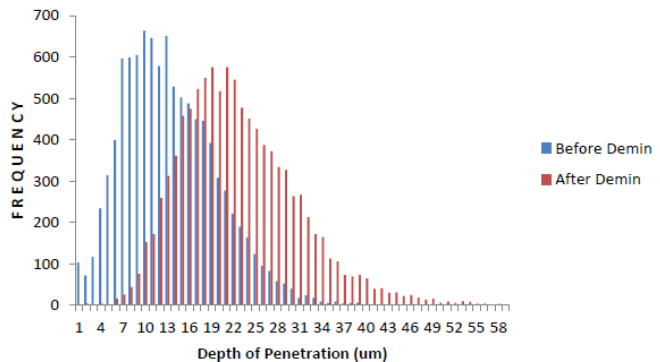


Figure 2 [58]: The difference in the depth of light penetration in mineralised and de-mineralised enamel.

Without going into further detail into the above researches it is enough to summarise that OCT can be used to detect changes in mineral content and with specific regard to enamel it can be thus used in the early detection of carious/eroded lesions within the teeth.

A very recent research [1] has rejected a null hypothesis which stated that there is no correlation between the refractive index and mineral content of enamel.

As seen before in the graphs, there was a difference in light penetration of de- and re-mineralised samples which suggests that the structure of the samples (deep inside) changes with the addition/depletion of minerals. The refractive index (n) is an important parameter in light propagation through biological tissues including teeth. The refractive index of the tissue can serve as an indicator of its scattering properties, as scattering itself is the end result of its local n variation [56].

By using OCT the relation between n and MC was found. This was achieved by studying sound (healthy), de- and re-mineralised dental enamel samples (and dentin samples) using OCT to measure their refractive indices and relating them to mineral content (of the same samples) by using TMR. Transverse microradiography (TMR) has been used before to determine mineral density of samples in-vitro. However, the refractive index was never thought to (or at least not proven to) have a direct relationship to mineral content (MC). This research therefore has opened up a new way to estimate the MC of enamel by finding out its refractive index. De-mineralised and re-mineralised enamel samples therefore have different refractive indices due to the difference in their mineral densities. A different mineral density means a difference in structure of the enamel samples and in turn, means a difference in the scattering properties of both samples. This can be picked up by OCT to measure the refractive index at various stages of de- and re-mineralisation.

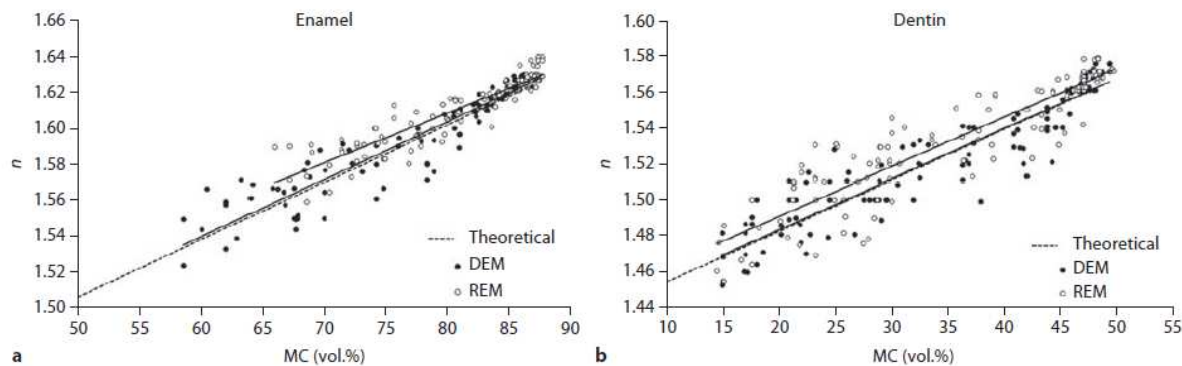


Figure 3: Relationship between n and MC measurement for de-(DEM) and remineralised (REM) enamel [1].

CONTRIBUTION OF THIS PROJECT

The gap in the clinical dentistry practice of diagnosing tooth decay/erosion by means of a detection tool which was mentioned earlier on has been a topic of research for some time at the School of Medicine and Dentistry in QMUL. One of the most recent topics within caries/erosion research, specifically within the early detection area is the design of such a diagnostic tool in the form of a hand-held probe which can be clinically feasible.

One of the challenges in designing a hand-held probe (current subject of research at SMD) using OCT to be deployed efficiently in the clinic is the issue of quantifying the received data and relating it directly to the mineral content. OCT is mainly used for imaging but these images are formed from raw data which depends on the reflection of the light from the sample under test. The refractive index of the sample could be computed as [1] have done and be used to provide a certain degree of quantification to supplement the 2D and 3D images that are formed in order to accurately assess the de-mineralisation and get an idea about the stage it is in in order to base clinical advice on.

Because the relationship between refractive index and mineral content has now been established, methods other than OCT for refractive index measurements can be studied in order to cross-check and justify OCT results. Measuring refractive index using other methods may be easier or more feasible than OCT, in addition to the possibility of them being more accurate or the devices being more sensitive to mineral loss than OCT. Although no other method can compete with OCT's high resolution imaging, it is possible that the measurement of the refractive index could be more accurate/more sensitive to mineral changes.

This project is one of three projects each using different devices to examine the effects of mineral loss in enamel on its refractive index. The system used in this project operates in the frequency range of roughly 50 to 325 GHz while the other two projects cover frequencies higher than this range all the way up to Infra-Red (IR) frequencies. This choice of using different systems covering different frequency ranges and using different methods of obtaining the refractive index of the sample will therefore tell which is the most suitable and effective for this purpose.

METHOD

For the purpose of measuring refractive index, a quasi-optical “Z bench” with a W band transmitter/receiver head pair feeding into a Vector Network Analyser were used. Microwave frequency propagation through materials has been used for a long time to measure dielectric properties of materials and characterise them for a variety of purposes such as identification or optimising them for use in certain applications. Dielectric property measurement using a VNA takes various forms, each suited to both the type of material and the results to be obtained. In this project, the scattering (S) parameters of the enamel samples were processed in Matlab scripts containing algorithms to extract the refractive index based on the S parameters. Details on the system used in this project will follow in the next section.

OBJECTIVES

The main objectives of this project are:

- Measuring refractive index of dental enamel samples at different stages of de-mineralisation to determine whether or not the transmissometer can pick up changes in mineral content.
- Identifying sources of error in the measurement procedure so that if research in this area continues, i.e. using the transmissometer to study dental enamel samples in the future, it could be done in a more accurate way and provide more reliable results.

REPORT STRUCTURE

The remainder of the report is structured as follows:

Background Research: this section contains multiple definitions and keywords that are essential to the understanding of this report. Almost all research carried out in order to undertake this project is shown in this chapter. It also contains many references to related papers and sources that describe similar work to that undertaken in the project and how everything is pieced together to enable this project to fit in the on-going research which aims to solve the problem presented in this section.

Implementation and Results: outlines the experimental procedures and the results obtained throughout.

Discussion/Analysis of Results: contains a detailed analysis of the results obtained and discusses their importance/relevance to the objectives specified. An “error analysis” section contains all possible sources of error that may have affected measurement results.

Conclusion: this is the final section of the report in which the summary of the whole project is presented and what can be deduced from the project. The extent to which the objectives were met is included in this section in addition to how well the project contributed to solving the “bigger problem”. Future work that may be conducted based on the proceedings of this project is also discussed as well as a summary of the main points in the error analysis section.

Background Theory

In this section of the report, a number of keywords and background information essential to the reader's understanding of this project are presented. Information in this section will enable the reader to grasp onto the material within the rest of the report and provide them with the basic theories and terms referred to throughout the report. This information is far from detailed but will most definitely help the reader identify specific keywords related to the material in this report and allow for further individual research.

THE TRANSMISSOMETER

The **transmissometer** mentioned briefly in the previous section which is the system used to measure the refractive index of enamel in this project can be broken down into two main parts:

1. *The Vector Network Analyser (VNA).*
2. *The quasi-optical (QO) circuit.*

The Vector Network Analyser will be discussed first, with the transmissometer discussed towards the end of this section.

1) The Vector Network Analyser:

The function of the VNA in this project is to measure scattering (**S**) **parameters** of the network. The basis of this lies in **two-port network theory** which is very common and widely used in RF (radio frequency) design and microwave electronics. In this model a network (system) is considered a "black box" with complete disregard to the contents of the box which could be anything from a transmission line, an amplifier or a filter, to an integrated circuit. In this project the black box was, surprisingly, a dental enamel sample. Thus the enamel sample was treated like a system which acts upon the incident signal while reflecting part of it and transmitting another part. A number of parameters are used to characterise the network based on its input(s) and output(s) which are usually signals with frequencies in the radio and microwave parts of the electromagnetic spectrum. The transmitted and reflected waves both have a different amplitude and phase to that of the incident wave.

A two-port network has one input port and one output port, each made up of a pair of terminals. A set of parameters can then be used to characterize the performance of this network, such as **Y** - parameters, **Z** - parameters, **T** - parameters and **ABCD** – parameters. Of specific interest to this project is the **S - parameters** of the network. These are different than the other sets of parameters used to characterize microwave frequency networks in a sense that they are only concerned with the incident, reflected and transmitted waves of the system. These waves are of particular interest in this project due to the relationship between them and the scattering properties of the material under study. Knowledge of the scattering properties of the material can lead to knowledge of the refractive index of the material (more on this later) which is beneficial for this project (as explained in the Introduction) for estimating the mineral content of the samples.

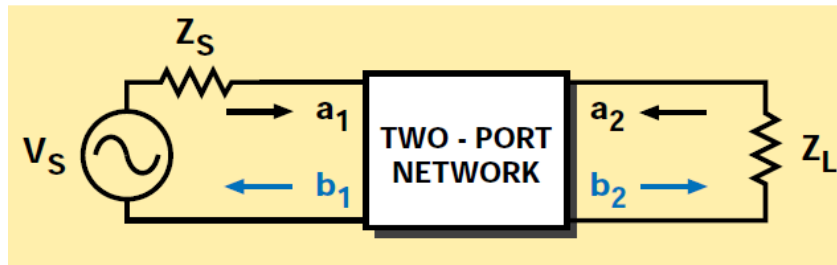


Figure 4 [59]: A general two-port network. V_s is the source which has a source impedance Z_s . Z_L is the load impedance. a_1 and b_1 are the incident and reflected signals at port 1 (respectively). a_2 and b_2 are the incident and reflected signals at port 2.

In the above illustration of a two-port network model **a1** and **a2** represent the incident waves. **b1** and **b2** represent either the reflected waves or the transmitted waves depending on the context they are used in, i.e. which port the incident wave is coming from. A network can have n-ports and that will result in 2^n S-parameters. Because two-port network theory is the most widely used model and it resembles the majority of devices it is sufficient for use in this project as the enamel sample has (although not literally) one input and one output. Thus a total of $2^2 = 4$ S parameters are used to describe the network.

These are written as S_{11} , S_{12} , S_{21} and S_{22} .

To fully know all 4 parameters the system has to be excited from both ports, i.e. by applying a signal on one port while the other port is idle and then reversing.



Figure 5 [60]: The 'black box' two port network model, with the incident wave applied to port 2.

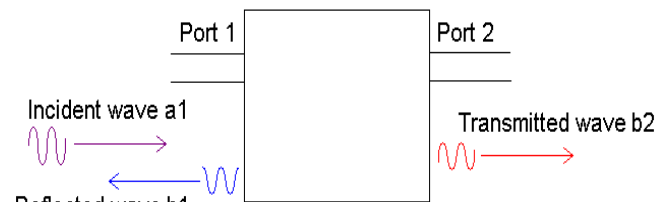


Figure 6 [60]: The 'black box' two port network model, with the incident wave applied to port 1.

S_{12} refers to the effect that the incident wave **a2** has on port 1, i.e. the ratio of the incident and transmitted waves. S_{12} is thus the ratio: $b2/a1$. This parameter is usually called the transmission coefficient as it describes the relationship between the ports and the effects they have on each other.

S_{22} is the ratio of the reflected wave **b2** and incident wave **a2** and thus holds information about the reflection properties of the system. $S_{22} = b2/a2$. This parameter (along with S_{11}) is normally called the reflection coefficient.

Reversing the process and applying the incident wave to port 1 allows the other two parameters to be calculated in the same method:

$$S_{21} = b2/a1, \quad S_{11} = b1/a1$$

These four parameters are complex and contain both magnitude and phase angle. They are usually represented in matrix form in what is called a scattering matrix:

$$\begin{bmatrix} V_1^- \\ \vdots \\ V_N^- \end{bmatrix} = \begin{bmatrix} S_{11} & \cdots & S_{1N} \\ \vdots & \ddots & \vdots \\ S_{N1} & \cdots & S_{NN} \end{bmatrix} \cdot \begin{bmatrix} V_1^+ \\ \vdots \\ V_N^+ \end{bmatrix}$$

Figure 7 [61]: The scattering matrix of an n-port network.

The above diagram represents the scattering matrix of an n-port network. The notation V represents the “backward” travelling wave and this representation is often used in transmission line theory. V_1^- in the diagram is the same as b_1 and V_1^+ is the same as a_1 .

One of the interesting things about this project is that S-parameters are usually used to characterise and evaluate the performance of microwave devices and circuits (modelled as two-port networks) and the reflected energy is due mostly to impedance mismatch between the source and load/transmission line. They are of use to RF/microwave engineers who design such systems and are concerned mostly with the complete transfer of power from source to load. This project deals with another use which relates the reflected (and transmitted) energy to the scattering properties of the material itself and its internal composition.

Having covered the basics about S-parameters the question now is: *How are they measured?* The most common device used to measure S-parameters is a network analyser. A network analyser is used for measuring network parameters of electrical networks and in the case of an RF/microwave network (high frequencies) the most common parameters measured are the S-parameters discussed earlier due to the relative ease of measuring them at these frequencies.

There are two main types of network analysers: the **Vector Network Analyser (VNA)** and the Scalar Network Analyser (SNA). As can be inferred from its name, the VNA measures both amplitude and phase properties of the network parameters. As S-parameters are complex numbers it is good to have a device that can measure them fully and not just the magnitude. The SNA can be used in cases where only the magnitude is required, for example when the **Device Under Test (DUT)** is an amplifier and the gain (which can be completely known from just the amplitude as the phase is of not much importance) is the matter of concern.

Vector Network Analysers consist of three main components, which are a signal source, a receiver and of course the display. The signal source can usually provide signals at a range of frequencies in order to measure the frequency response of the sample at varying frequencies. Every time the S-parameters are calculated for one frequency after receiving the transmitted/reflected signals, the signal source steps up the frequency of the incident signal and the calculation is done again.

The VNA available in the Terahertz division of the Antenna Laboratory at QMUL has a frequency band of 10 MHz to 43.5 GHz [62]. This means that it is capable of generating test signals with all frequencies in this band which enables the DUT to be probed at different frequencies and thus gives an idea about the frequency response of the system over that frequency range. S-parameters measured over a range of frequencies provide a complete characterisation of the system and modifications can be then made to improve it for optimal performance in “real-life” situations.

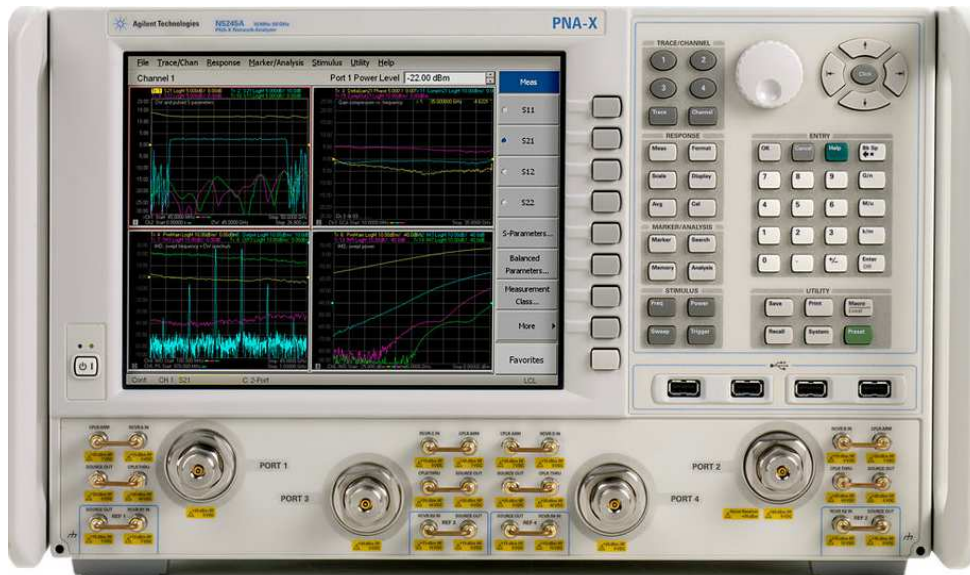


Figure 8 [62]: The VNA used in the experiments (**Agilent Technologies N5244A PNA-X Microwave Network Analyser**). This VNA can measure parameters of a four port network. As our “system” is a two-port network, connections are only made to PORT 1 (far left) and PORT 2 (far right).

The two main sub-bands in the electromagnetic spectrum that make up the larger microwave band are the **SHF** (super-high frequency) and **EHF** (extremely high frequency) bands. EHF is the highest radio frequency band (just before Far Infra-Red) and consists of waves with frequencies between **30** and **300 GHz**. EHF is also called the **millimetre wave band** as the wavelength of the waves in this band lie between 10 mm and 1 mm. The millimetre-wave spectral range, which bridges microwave and optical regions, is of particular significance mainly due to a rapidly growing number of millimetre-wave applications and components [63].

This range is of critical importance in the spectroscopy of condensed matter systems [64] and thus is the bandwidth that is of interest in this project; but the question now is: *How is such a large frequency achieved by the available VNA?* This is resolved by adding a **millimetre head controller** which, in turn is connected to two **millimetre-wave extenders**. These instruments allow the VNA to take mm-wave measurements by increasing its operating frequency band into this frequency range.



Figure 9 [65]: The complete VNA configuration used in this project. The **N5262A mm head controller** is shown placed under the VNA and is connected to two **millimetre-wave modules**. It provides the interface between the VNA and the modules (extenders).

The mm-wave modules are of model **V** VNA2-T/R-A** where the ****** correspond to the digits below:

15: allows extension of 50 - 75 GHz

10: 75 – 110 GHz (used for 3 of the 4 experiments)

06: 110 – 170 GHz

03: 220 – 325 GHz (used for 1 of the 4 experiments)



Figure 10 [66]: The N5262A Millimetre-Wave Controller for the PNA-X Network Analyser Series.

The controller shown above provides the interface between a maximum of four millimetre-wave head modules and a PNA-X Series network analyser [67].

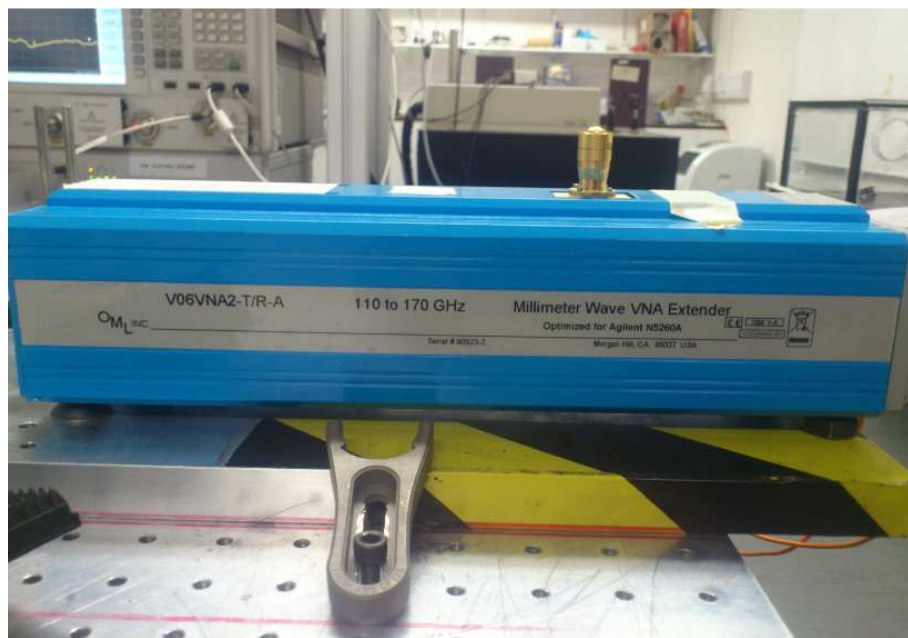


Figure 11: One of the pair of 110 - 170 GHz mm wave extenders available in the lab. The ones used for this project are the 75 - 110 and 220 - 325 GHz ones (not this one).

A single T/R (Transmission/Reflection) module allows the measurement of the S_{11}/S_{22} reflection coefficient only. The use of two T/R modules in the millimetre-wave VNA system allows for all four S-parameters to be measured. When the two modules are connected to the VNA via the controller, S_{11} and S_{21} are measured on the forward direction; S_{22} and S_{12} are measured when the signal path is reversed [68].

So by using two mm modules (of the same type) at a time, in four trials a frequency sweep from 50 - 325 GHz (approx.) can be done provided the module pairs are changed at every trial. According to the manual the signal path needs to be reversed in order to measure all four S-parameters of our two-port network. This is achieved by allowing the signal to be transmitted from one end while the other end receives, and doing the same thing in the opposite manner, just as in the illustration of **Figures 5 and 6**. Thus, the signal goes from PORT 1 of the VNA (and of the sample) and is read by PORT 2 one time and the opposite is done on the next time. This process can be repeated with every pair of mm-wave modules with the mm head controller providing the interface with the VNA's PORT 1 and PORT 2. These two signals are enough to generate the scattering matrix of the "DUT" which in our case is the enamel sample.

In this project, only one pair of waveguides (mm wave modules) was used and the enamel samples were tested under only one frequency range (75 - 110 GHz).

So far has been a discussion of the "measurement" part of the transmissometer. The other part, which includes everything between the two mm waveguides described above, is what is known as a quasi-optical (QO) circuit. This section of the transmissometer is where the sample is placed to allow the signals from the VNA to pass through it. In other applications the DUT is connected directly to the ports of the VNA (via the mm modules and controller). This project, however, uses a different approach for propagating the electromagnetic beam through the sample. One of the reasons for this is because the "network" is not exactly an RF device or microwave circuit but is instead an enamel

sample. This is where the QO circuit comes to use in order to efficiently guide the signals emerging from the VNA through the enamel sample with minimal losses compared to free space propagation.

Before discussing the quasi-optical circuit, however, it is important to understand how S - parameters are related to the refractive index in order to justify the use of the VNA in measuring it.

DIELECTRIC MATERIALS

Dielectric materials are generally poor electricity conductors, i.e. they either have little or no free electrons due to the high gap between the electron valence band and the conduction band. However, they have the ability to store electrostatic fields in them due to the presence of polar molecules within the material. Polar molecules are charged molecules (one end having a positive electrical charge and the other end a negative one) which initially are randomly orientated within the material in the absence of an electric field. Upon applying an external electric field, positive charges are displaced in the direction of the field while negative charges are displaced towards the source of electric field. The illustration below shows an example of what happens in such situations.

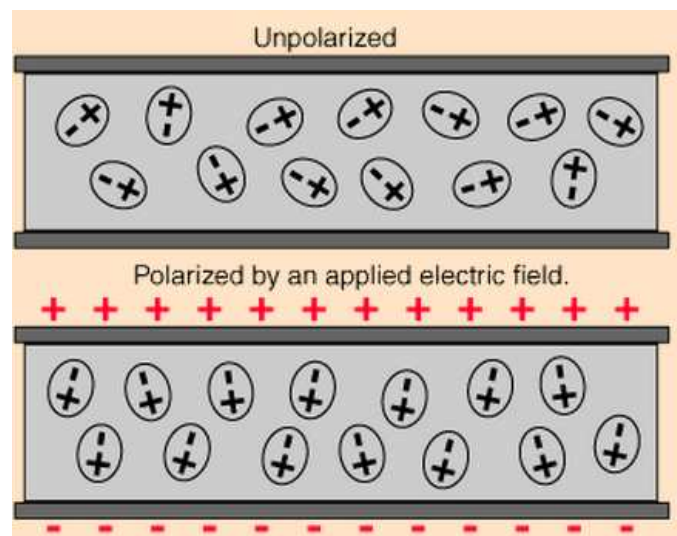


Figure 12 [69]: Polar molecules before and after polarisation by applying an electric field. The molecules are randomly aligned in normal conditions. When an electric field is applied they orient themselves with it.

If the molecules are weakly bonded they can change their orientation (as seen in **Figure 12**). If they are strongly bonded then distortion of the molecules can occur due to the differing directions that the positive charge(s) and the negative charge(s) on it are pulled towards.

The shifting of charges from their average equilibrium positions in a dielectric when faced with an electric field is called **dielectric polarisation**. Polarisation causes the material to have an electrostatic field within it which is opposite to the direction of the external electric field. The extent of polarisation within a dielectric can therefore determine the strength of the electric field within it. The electric field within it causes the material to experience a net electric field weaker than the external electric field. The property of 'storing' an electric field is thus all down to the degree of polarisation within the material.

The effect of an electric field on a dielectric medium can be measured by the absolute permittivity of the material. The absolute permittivity is more strictly a measure of the resistance that the material

exhibits when an electric field is being formed in it, for e.g. by polarisation as seen earlier. Absolute permittivity is given the following notation:

$$\epsilon = \epsilon_r \epsilon_0$$

where ϵ_r is the relative permittivity and ϵ_0 is the permittivity of free space. ϵ_0 has a value of approximately 8.85×10^{-12} farads per metre (F m^{-1}).

ϵ_r , the relative permittivity of a material is also known as the “**dielectric constant**” of the material and is generally complex. ϵ_r is just the ratio of the absolute permittivity to the vacuum permittivity so talking about one is the same as talking about the other. The dielectric constant is a complex number which can vary with position within the material, material state (solid, liquid or gas), the frequency of the applied field, humidity, temperature and other factors. It is thus common to write permittivity as $\epsilon(\omega)$ to show that it is frequency dependent.

Since ϵ_r is complex, it can be expressed as:

$$\epsilon_r = \epsilon^I + j \epsilon^H$$

ϵ^I is the real part of the permittivity and relates to the amount of electrostatic potential energy stored within the medium that can be exchanged with the external electric field.

ϵ^H is the imaginary part of the permittivity which is related to the loss of energy within the medium (usually as heat) or in other words how much it can absorb energy from the field causing the field to lose energy and become attenuated.

These two parameters can be formed into another parameter called the loss tangent:

$$\tan \delta_d = \epsilon^H / \epsilon^I$$

The loss tangent is usually used to characterise materials and is a property that can give an idea about the ratio of the energy lost to the energy stored of the specific material.

One of the aims of this project is to obtain refractive index measurements using the transmissometer in order for them to be compared later on to measurements obtained using OCT.

The refractive index of a certain medium, in its simplest definition is the ratio of the speed of light/electromagnetic radiation in vacuum to its speed in the medium. Hence, it can be used to describe the propagation of radiation through a particular medium. The refractive index is thus also frequency dependent and complex just as permittivity and is often shown as $n(\omega)$. The relationship between the refractive index of a dielectric medium to its dielectric constant is:

$$n(\omega) = \sqrt{(\epsilon_r(\omega) \mu_r(\omega))}$$

μ_r is the relative permeability of the material and is similar in concept to permittivity. It describes how the material responds to a magnetic field acting on it. Since electromagnetic waves are composed of magnetic and electric field components, both permeability and permittivity are required to describe the propagation of electromagnetic radiation through the material. Most naturally occurring materials have μ_r very close to 1 at optical frequencies [70]. This includes non-magnetic materials, for which μ_r is assumed to be 1 and thus the magnetic field component of the electromagnetic wave passing through the material induces no response from the material itself.

Materials are classified into four general categories based on the value of the relative permeability [71]:

1. *Diamagnetic*: $\mu_r < 1$
2. *Non-magnetic*: $\mu_r = 1$
3. *Paramagnetic*: $\mu_r > 1$
4. *Ferromagnetic*: $\mu_r \gg 1$

In this project, the samples studied are non-magnetic and thus permittivity is the main dielectric property of concern. Permeability becomes important when studying magnetic materials such as ferrites which exhibit magnetic responses.

DIELECTROMETRY

Permittivity and permeability which were discussed above are known as the dielectric properties of a material. Knowledge of these properties is important to scientists or engineers for various reasons. Reasons for characterisation of materials based on dielectric properties include:

- 1) Material/Circuit design.
- 2) **Research** (the reason in this project).
- 3) Quality control.
- 4) Integration of a material into a specific application where the presence of electric/magnetic fields can affect its behaviour.

Engineers within this field can utilise dielectric properties of materials for reasons 1), 3) and 4) so that materials can be used in the best possible way within their respective applications. Scientists conducting research can utilise dielectric properties for example to understand the reason behind certain materials' behaviour in the presence of electromagnetic fields. A relevant example of this is one of the parts of the research which this project aims to assist which focuses on quantifying the change in refractive index of enamel as its mineral content decreases when de-mineralisation occurs. The change in the enamel's structure when de-mineralised causes it to respond differently to the electromagnetic signal applied to it due to its dielectric properties changing.

Returning to dielectric material parameters, some other parameters exist that relate to the behaviour of an electromagnetic wave as it passes through the sample which in turn depend on its permittivity and/or its permeability.

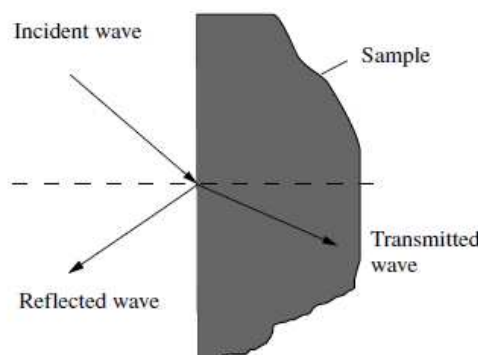


Figure 13: Boundary conditions for material characterisation using non-resonant methods [72].

As seen in the picture above, a material on which an electromagnetic wave is incident will have a reflected wave due to the difference between the wave impedance of free space (η) and the wave impedance in the material (Z) just as a wave travelling through a transmission line will reflect if the source impedance and load impedance aren't matched. η and Z have the following formulas:

$$\eta = Z_0 = \sqrt{\frac{\mu_0}{\epsilon_0}} = 120\pi$$

$$Z = \sqrt{\frac{\eta}{\epsilon_r}}$$

The part of the wave that is transmitted will also have a velocity in the material (v) which is lower than its velocity in free space ($c \approx 3 \times 10^8$ m/s).

Just as the wave impedance in the material depends on its permittivity, the velocity of the wave passing through also depends on the permittivity:

$$v = \frac{c}{\epsilon_r}$$

Coming to the main point, which is how a VNA can be used to measure the dielectric properties, this discussion of reflected and incident waves sounds similar to the S-parameters which were discussed earlier. Since VNAs can measure, in the form of S parameters, the transmission or the reflection of a wave through a network then they can also be used to measure the transmission/reflection of an identical electromagnetic wave through a material which in turn depends on the dielectric properties of the "network" (material). This makes VNAs the most used and most important tool in dielectric property measurement techniques.

Measurement of dielectric properties of materials has been around for a long time and multiple methods have been used which are under constant improvement.

Methods can be generally classified into two main categories: **resonant** and **non-resonant**. Non-resonant methods are often used to get a general knowledge of electromagnetic properties over a frequency range, while resonant methods are used to get accurate knowledge of dielectric properties at single frequency or several discrete frequencies [72].

The method used in this project is a sub-type of the non-resonant methods category called the **free-space method** and is based on phenomena related to microwave propagation, as opposed to microwave resonance phenomena.

Figure 14 on the next page shows a summary of the most common dielectric property measurement methods that are used.

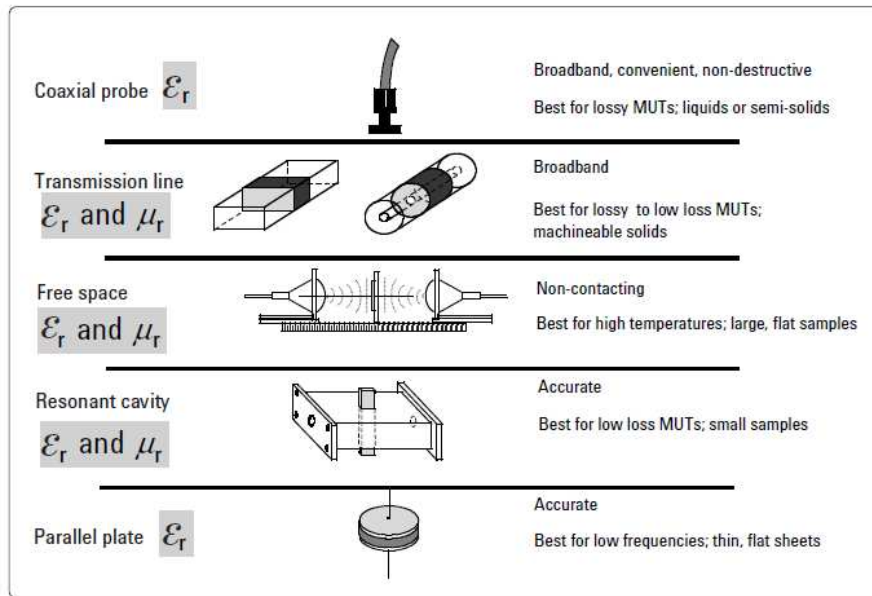


Figure 14 [73]: A summary of the main types of dielectric property measurement techniques used to date (both resonant and non-resonant).

Choice of which method to use is based on a lot of factors, including the frequency of interest, limitations on measurement accuracy, state of material (solid/liquid/gas), property of the material (homogeneous/isotropic), whether the sample can be destroyed or not, sample size or whether the material's properties vary considerably with temperature (some methods can't support temperature dependency) [74]. Selecting the free-space method wasn't my choice and the reason that it was used in this project is due to the availability in the THz lab of the relatively advanced (and accurate) quasi-optical circuit which is used to transmit the signal (in free space) between the ports of the VNA (more on this soon).

The relationship between S-parameters and the dielectric properties have been used for a long time for multiple techniques (both resonant and non-resonant). The extraction of the permittivity and/or the permeability of a sample based on its measured transmitted and/or reflected signals is based on formulas that have been developed which link the wave impedance in the sample, in addition to other parameters, to the corresponding reflected and/or transmitted signals' amplitudes which are characterised by the S-parameters. An example of one of the most common methods is the **Nicolson-Ross-Weir** method which was one of the earliest ones. All the different formulae have multiple elements in common with each other and papers that present improvements to the calculations in terms of speed or accuracy are published from time to time. Variations in the formulae linking the dielectric properties to the S-parameters are largely due to the different experimental setups including the technique and frequency range used.

These algorithms are generally used to create theoretical models to which the measured S-parameter data is fitted, usually using least-squares approximations (which have many forms), in order to obtain the dielectric properties.

For the purpose of this project, the formulae used to create the theoretical models are written in a PhD thesis written by Bin Yang titled “*Assessment of Magnetic Material for Use in Quasi-optical Non-reciprocal Devices Operating at Frequencies above 90 GHz*” [75]. These formulae were quite unique and were slightly different than those found in other sources. They were used (in the thesis) to measure the complex refractive index of ferrite materials used to design quasi-optical Faraday rotators. While I was researching about formulae linking S-parameters to dielectric properties in

microwave measurement publications, the author of this thesis, who was supervising the experiments on the transmissometer suggested I try and use the formulae in his thesis.

The formulae used are as follows:

$$\text{Reflectance: } r_{\pm}(\omega) = \frac{r_{1\pm} - r_{1\pm} e^{i2(\omega/c)n_{\pm}(\omega)d}}{1 - r_{1\pm}^2 e^{i2(\omega/c)n_{\pm}(\omega)d}}$$

$$\text{Transmittance: } t_{\pm}(\omega) = \frac{(1 - r_{1\pm}^2) e^{i(\omega/c)n_{\pm}(\omega)d}}{1 - r_{1\pm}^2 e^{i2(\omega/c)n_{\pm}(\omega)d}}$$

Both Transmittance and Reflectance are frequency dependent and are functions of $n(\omega)$ which is the frequency dependent complex refractive index, d which is the thickness of the sample, c which is the speed of light in free space and r_1 which is the single face reflectance or the reflected signal from the first air-sample boundary and is given by:

$$\text{Single face reflectance: } r_{1\pm}(\omega) = \frac{Z_0 - Z_{\pm}(\omega)}{Z_0 + Z_{\pm}(\omega)}$$

where Z_0 is the (normalised) free space wave impedance and $Z(\omega)$ is the frequency dependent wave impedance of the signal within the sample given by $\sqrt{\frac{\mu_r}{\epsilon_r}}$.

Both Transmittance and Reflectance are complex and can be equated to complex S-parameters after they are multiplied by a “thickness phase compensation” of $e^{j\omega d/c}$, i.e.

$$\text{Transmittance} = S_{21}(\omega) \times e^{j\omega d/c}$$

$$\text{Reflectance} = S_{11}(\omega) \times e^{j\omega d/c}$$

where S_{21} can be interchanged with S_{12} and S_{11} with S_{22} depending on the measurement procedure.

There are various ways of efficiently propagating electromagnetic radiation, with each method being appropriate to the frequency (wavelength) of the radiation. This is because of the fact the electromagnetic waves in open space propagate in all directions, following the inverse square law and losing power by a factor of D^2 where D is the distance from the source. This implies the necessity to guide the waves from one point to another as efficiently as possible with minimal power loss, particularly in the microwave part of the electromagnetic spectrum. Some of the structures built to propagate electromagnetic waves include **transmission lines**, **waveguides**, **coaxial cables**, **microstrip lines** and many more.

At microwave frequencies, waveguides are most commonly used for propagation. These structures are usually built using a metallic conductor which can be either hollow or filled with a dielectric. The “mode” in which the wave can propagate within the waveguide is determined by solving the

electromagnetic wave equation with boundary conditions related to the materials in the waveguide as well as its dimensions. Solutions to the wave equation, with boundary conditions taken into consideration determine the “mode” in which the waves can travel within that particular waveguide as well as the cut-off frequency of the waveguide.

The three main modes of electromagnetic wave propagation are:

TE mode: when there are no electric field (vector) components in the direction of propagation.

TM mode: when there are no magnetic field (vector) components in the direction of propagation.

TEM mode: when there are neither electric nor magnetic field vector components in the direction of propagation.

Free space dielectric property measurement requires a means of directing the electromagnetic signal through the sample with minimum power losses. Aperture antennas, more commonly known as **horn antennas** or feed horns, which are special types of antennas can do this job by providing the transition between the waveguide used to carry the signal from the VNA’s signal generator (or the mm-wave extenders in this case) to free space and back again after it is reflected/transmitted through the sample. Their choice of use in these types of applications is due to the fact that they transform the electromagnetic wave in the waveguide into a beam which is more manageable in free space.

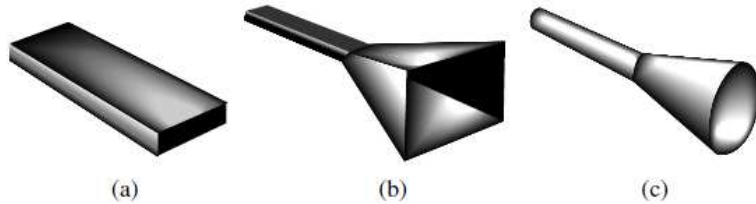


Figure 15 [76] Typical aperture antennas. **(a)** is a regular rectangular waveguide aperture antenna. **(b)** and **(c)** are pyramidal horn and conical horn antennas (respectively). Horn antennas are special types of antennas made from hollow metal waveguides that are shaped like horns.

After the signal emerges from the antenna there is the issue of diffraction effects affecting the S-parameter measurement results. Since all waves experience diffraction at the edges of materials, the sample has to be either larger/the same size as the wave’s **transverse** (perpendicular to the direction of propagation) height and width, measured in wavelengths. This is why free space measurements have to adhere to the general rule of thumb:

$$d \gg h \gg \lambda$$

where **d** is the transverse dimensions of the sample, **h** is the transverse dimensions of the electromagnetic signal and **λ** is its wavelength [72]. In order for this condition to be satisfied and generate accurate results, horn antennas, along with other components are used simultaneously to generate either **parallel beams** or **focused beams** in order to ensure that all of the signal’s power is transmitted through the material.

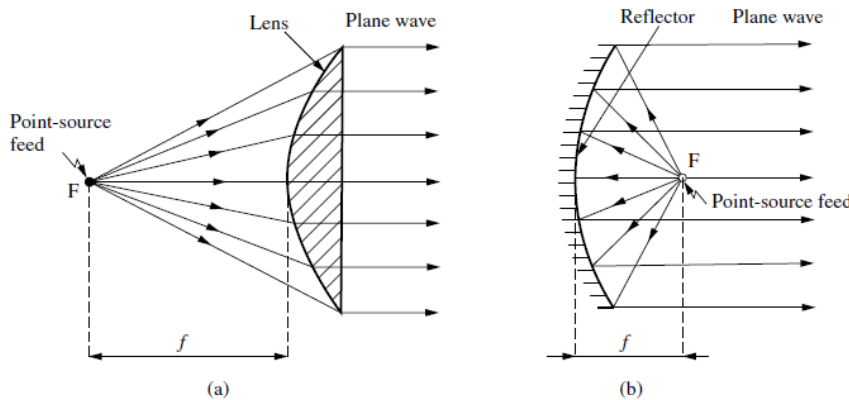


Figure 16 [77]: The generation of a parallel microwave beam by means of (a) a lens and (b) a reflector.

In this project a focused beam is used to direct the signal through the sample. This brings the discussion to the other part of the transmissometer which is the quasi-optical circuit where the focused beam is formed.

2) The Quasi - Optical circuit:

Optics in general is the study of the properties and the behaviour of light and how it interacts with matter. Optics also involves the design and building of instruments that use light in a specific manner or instruments that help detect it (in the case of non-visible light).

Optics has several branches and studies each of which applies different theories and models depending on specific applications. Some of them are listed below [78] [79] [80]:

Theoretical optics: accounts for most optical phenomena with use of electromagnetism. It is often difficult to apply in practice but is used when non-simplified models are needed and is one of the main branches.

Practical optics: the study of optics in the practical field. It has two sub-branches:

Physical: accounts for some wave effects of light such as interference, polarisation and diffraction which geometric optics doesn't cover.

Geometric: models light as a collection of rays that travel in straight lines and bend when passing through/reflecting from surfaces. Geometric optics' models are used when designing quasi-optical circuits with the difference being that diffraction is accounted for and controlled.

Quantum optics: covers phenomena that can be explained by light's wave-and-particle like nature and thus deals with the application of quantum physics/mechanics to optics.

Quasi optics: is the branch of optics that this project revolves around and the system where the sample is placed is a type of quasi-optical system. According to Goldsmith [81]: "*Quasi optics is concerned with the propagation of electromagnetic radiation when the wavelength of the radiation is more or less comparable to the size of the optical components (mirrors/apertures/lenses) of the system through which the radiation is passing*". Typical wavelengths at which quasi optical circuits are used are from about 1 – 2 mm but they can be used for higher (and lower) frequencies. Common

conventional electronic circuits have voltages/currents as their inputs and outputs. In quasi-optical circuits the inputs and outputs to the circuit are in the form of electromagnetic beams of radiation.

Recalling the three electromagnetic wave propagation modes which are called the “**transverse modes**”, each has a different pattern of field distribution or profile, namely electric field intensity, when looking at any plane (cross section) which is perpendicular to the wave’s axis/direction of propagation.

The mode of electromagnetic propagation used within the quasi-optical circuit for the experiments in this project is called the “fundamental TEM mode” or **TEM₀₀**. This particular mode displays a transverse electric field intensity profile similar to that of a Gaussian function and is commonly used in lasers. Recalling the two types of beams used in free space measurement techniques, a beam with a Gaussian intensity profile can be used in conjunction with a curved reflector (discussed later on) can be transformed into a focused beam.

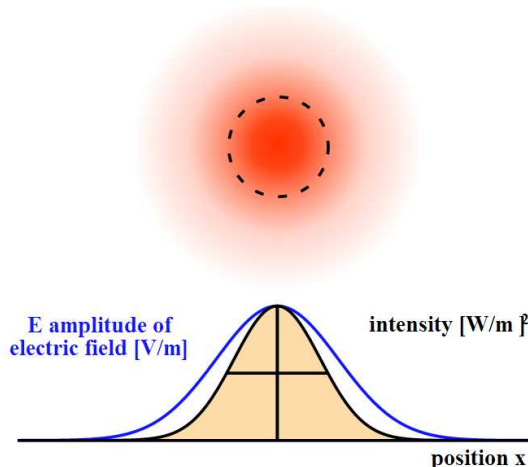


Figure 17 [82]: Electric field intensity (approximated by a Gaussian function) and the corresponding intensity profile. The top portion of the diagram shows the two-dimensional intensity profile of a Gaussian beam that is propagating out of the page. The blue curve, below, is a plot of the electric field amplitude as a function of distance from the centre of the beam. The black curve is the corresponding intensity function.

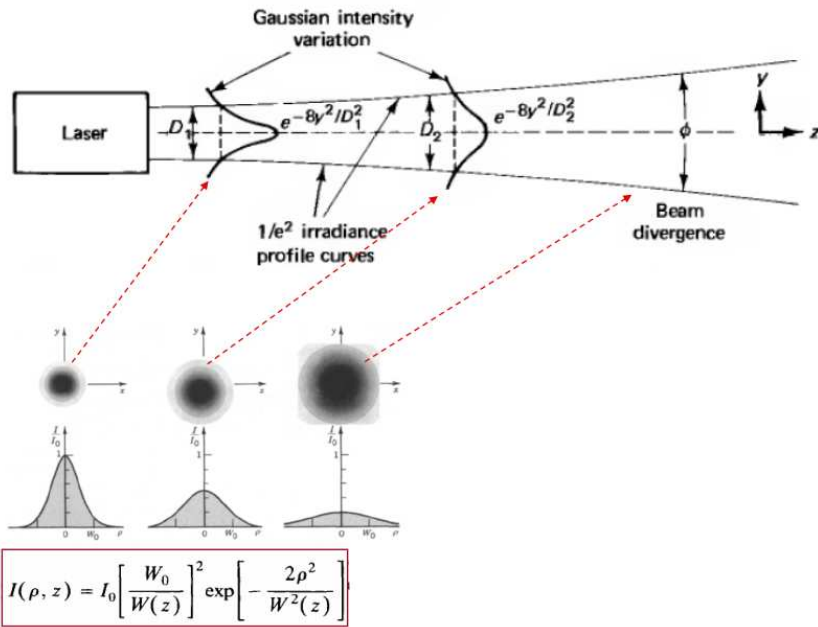


Figure 18 [83]: A schematic of a laser beam at three points throughout the direction of propagation. The transverse irradiance/intensity of the beam has a profile similar to a Gaussian function. Three different functions are shown with the corresponding spot sizes (of the beam) at the three different points along the z axis.

The formula in the red box in **Figure 18** above calculates the intensity distribution which can be very closely approximated by a Gaussian function. I_0 is the intensity at the beam waist, seen at the position of w_0 in **Figure 19** below, which also occur (but isn't shown) at the end of the laser in **Figure 18** (above). A Gaussian beam has a characteristic called the spot size, which is the diameter of the beam along any perpendicular plane to the beam's propagation direction. The spot size is smallest at the beam waist (where it is $2w_0$), and generally becomes larger as the beam diverges, i.e. as $w(z)$ in **Figure 19** increases.

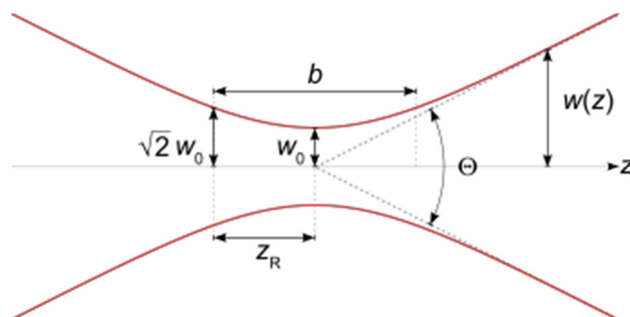


Figure 19 [84]: Some Gaussian beam parameters around the beam waist. $w(z)$ is the Gaussian beam width, which generally increases as the axial distance z increases, i.e. as the beam diverges. w_0 is the beam waist, b is the depth of focus, z_R is the Rayleigh range and Θ is the total angular spread.

w(z) corresponds to the radius of the spot size and is smallest at the **beam waist** where it has a value of w_0 .

$$w(z) = w_0 \sqrt{1 + \left(\frac{z}{z_R}\right)^2}$$

z_R in the formula above is called the **Rayleigh range** and is equal to $\frac{\pi w_0^2}{\lambda}$ where λ is the wavelength of the beam.

One of the horn antennas which isn't shown in **Figure 15** is a special type of feed horn is the corrugated horn which exhibits radiation symmetry [85] and thus can be used to create Gaussian beams from electromagnetic radiation emerging from a waveguide (the case with the VNA).

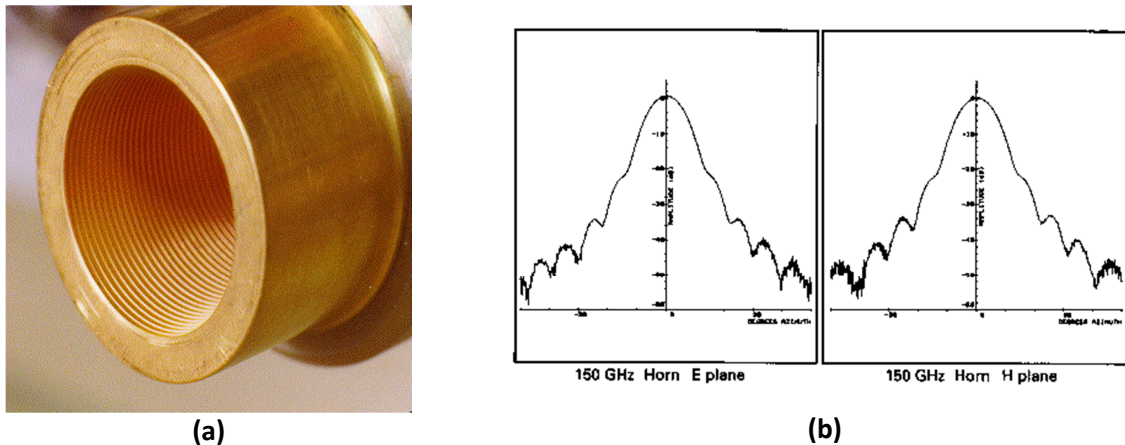


Figure 20 [86]: (a) Corrugations visible on the inside of such feed horns. (b) Electric and Magnetic field patterns of a corrugated horn in (a) designed by Thomas Keating Ltd., operating at 150 GHz. The field patterns show axial symmetry and look very similar to Gaussian functions.

The corrugated horns attached to the millimetre wave extenders create Gaussian beams with the beam waist at the aperture (exit hole) of the horns. As the beam emerges from the horn, it starts diverging slowly due to the diffraction/expansion effects as it propagates in the open air spaces.

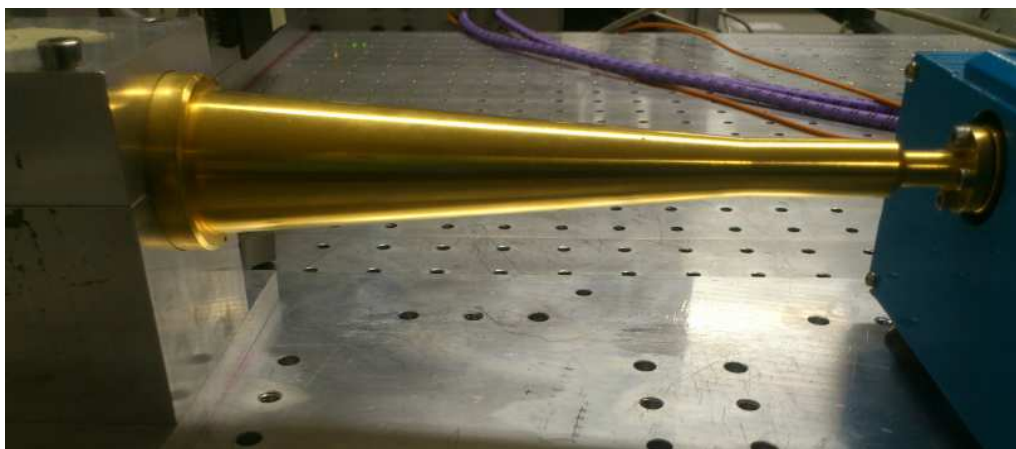


Figure 21: Outer view of one of the pair of corrugated feed horns used in the circuit. The signal exits the mm wave head from the right, enters the horn where boundary conditions transform its propagation into the TEM_{00} / Gaussian beam mode. The beam then enters the quasi-optical circuit on the left.

The quasi-optical circuit used consisted of **curved** and **flat reflectors** [87] which the beam reflects off. The curved reflectors, also called **ellipsoidal mirrors** reflect the beam in a certain direction, causing it to form another beam waist somewhere along that direction. A characteristic of Gaussian beams is that they stay Gaussian when reflected or refracted. When reflected by a curved mirror they are focused again, resulting in another beam waist. Thus, by the addition of mirrors in specific locations, it is possible to preserve the entire signal by focusing it multiple times and thus constantly “correcting” the divergence of the beam. Focusing the beam using ellipsoidal (curved) mirrors instead of traditional lenses is preferred because of their wider bandwidth [88].

The two other components of the quasi optical circuit in addition to the horns and the curved reflectors are the **wire grid polarisers** and the **absorbers**. Polarisers are filters used in optics that pass light/electromagnetic radiation through with only one, specific polarisation. Light with mixed polarisation or any radiation whose polarisation is unknown can be filtered through the polarisers. The two main types of polarisers are **linear polarisers** and **circular polarisers**. Wire grid polarisers are a type of linear polarisers and let electromagnetic radiation through either horizontally or vertically to the direction propagation. Choosing the polarisation state is useful in some cases, especially when it is to be passed through certain materials that have different responses to either state.

Wire grid polarisers are made from meticulously wounded conducting wires around a supporting metal frame. The wires are closely spaced together and have very small diameters, with diameters of 5 μm available [89]. Their method of operation is based on the fact that an electric field parallel to a wire will create a current along its length which in turn causes it to generate electromagnetic radiation. The electric field vector generated from the wires is equal to the incident electric field vector and opposite in direction which causes both electric field vectors to cancel each other out. The vector of the electric field which is perpendicular to the wires cannot cause a potential difference (hence current) along the height of the wires due to their diameters being too small. The diameters of the wires in the polarisers is chosen to be smaller than the wavelength of the incident signal and the spacing (although very small) between them means that the perpendicular component of the electric field also can't set up a potential different along the length of the grid. This process leaves only the component of the electric field which is perpendicular to the wires to pass through while the component parallel to the wires gets reflected.

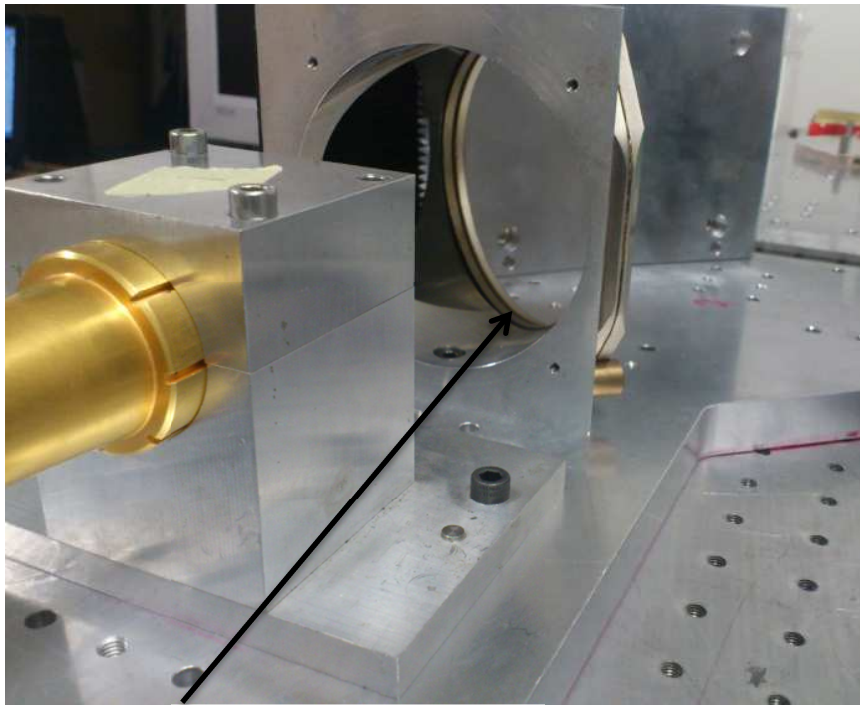


Figure 22: The wire grid polariser used in the experiments. The polariser is the first thing that the beam crosses after emerging from the corrugated horn.

The component of the electric field that doesn't pass through gets reflected back and cancels out with the incident electric field component. An absorber placed at the back of the polariser absorbs/damps any remaining radiation which is reflected back in order to not interfere with the rest of the incident signal.

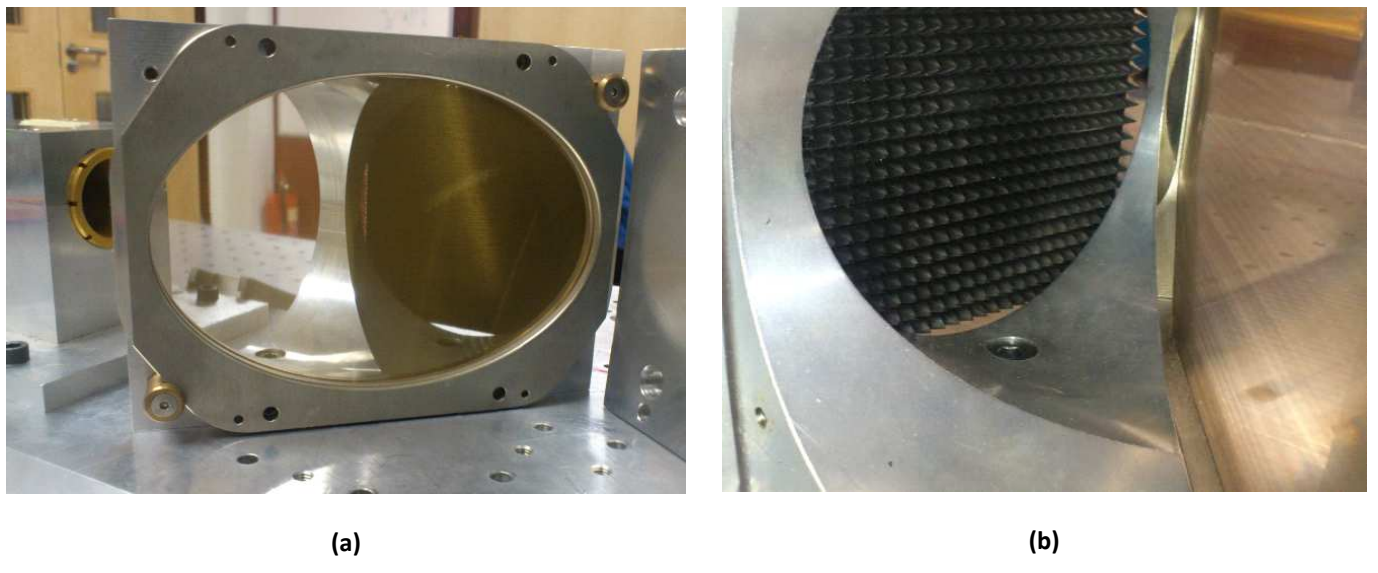


Figure 23: (a) A front view of the wire grid polariser used in the experiments. (b) A view from the back of the polariser. The black square with small cone shaped perforations is the absorber which dissipates the reflected electric field component that doesn't pass through.

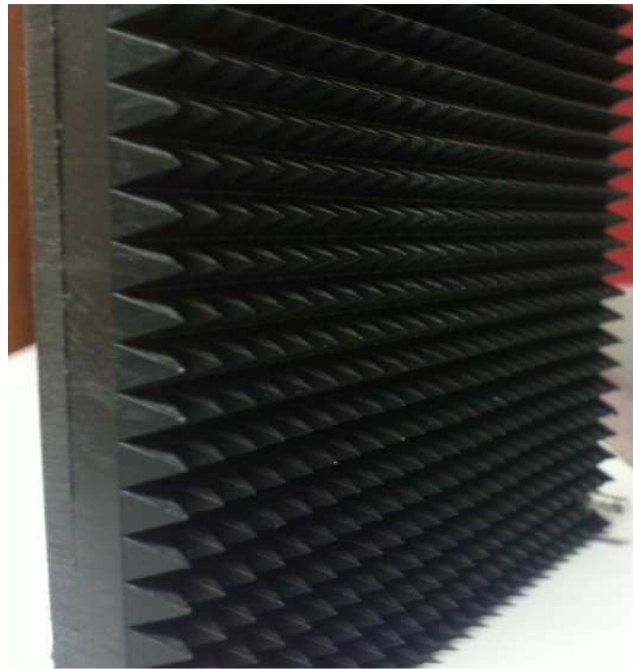


Figure 24: One of the absorbers used in the quasi-optical circuit to damp the signals reflected back from the wire grid polarisers.

Absorbers are used for a variety of applications one of which is eliminating unwanted radiation that could affect the performance of a system or potentially generate inaccurate results. They are made of a matrix of usually cone/pyramidal shaped protrusions filled with a material that can greatly attenuate electromagnetic radiation. Absorbing filling material is characterised by its permittivity and permeability which were discussed in the “dielectric materials” part of this section. The real and imaginary parts of the complex permittivity and permeability can be re-arranged in the form below to calculate the **loss tangent** of the material:

$$\tan \delta_e = \frac{\epsilon''}{\epsilon'}$$

$$\tan \delta_m = \frac{\mu''}{\mu'}$$

The two quantities above are called the electric and magnetic loss tangents of a material. The higher the loss tangent of the material the greater the attenuation it has on either (or both) the electric/magnetic field and hence on the wave as a whole. Materials in the absorbers have very high loss tangents in order to provide perfect attenuation of unwanted waves.

The bandwidth used in 3 of the 4 experiments in this project is the **W band** (75 – 110 GHz). The VNA millimetre wave heads (extenders) used for these experiments are pictured in **Figure 11** earlier on in this section. The quasi-optical circuit used for this frequency range is given the name “Z - bench” due to its Z-like shape.

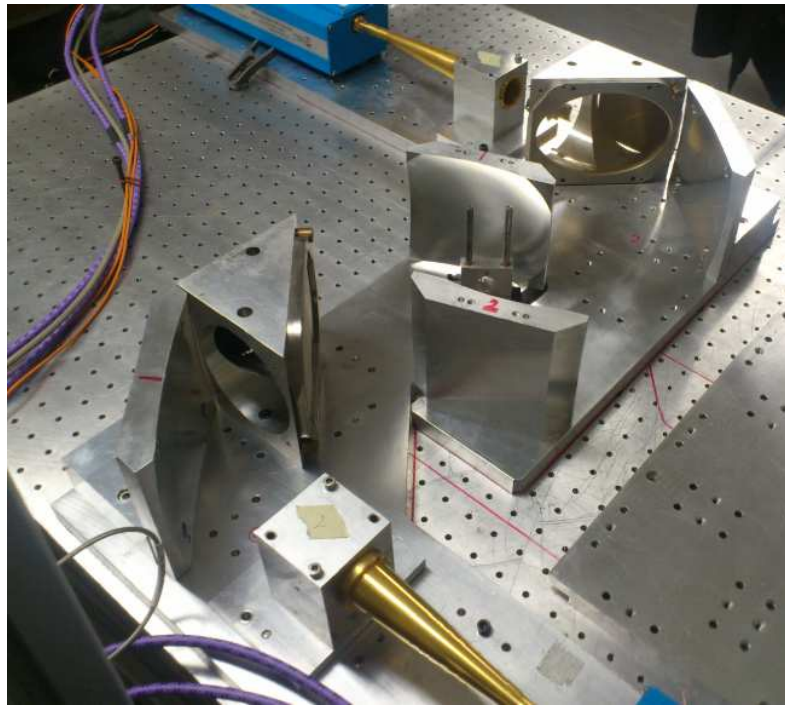


Figure 25: The quasi-optical circuit “Z bench” used for the experiments in this project. The golden horns create the Gaussian beams which feed, via the extenders into the VNA’s Port 1 and Port 2 in order to measure the scattering parameters of the Device Under Test (sample) placed in the middle of the circuit at the beam waist.

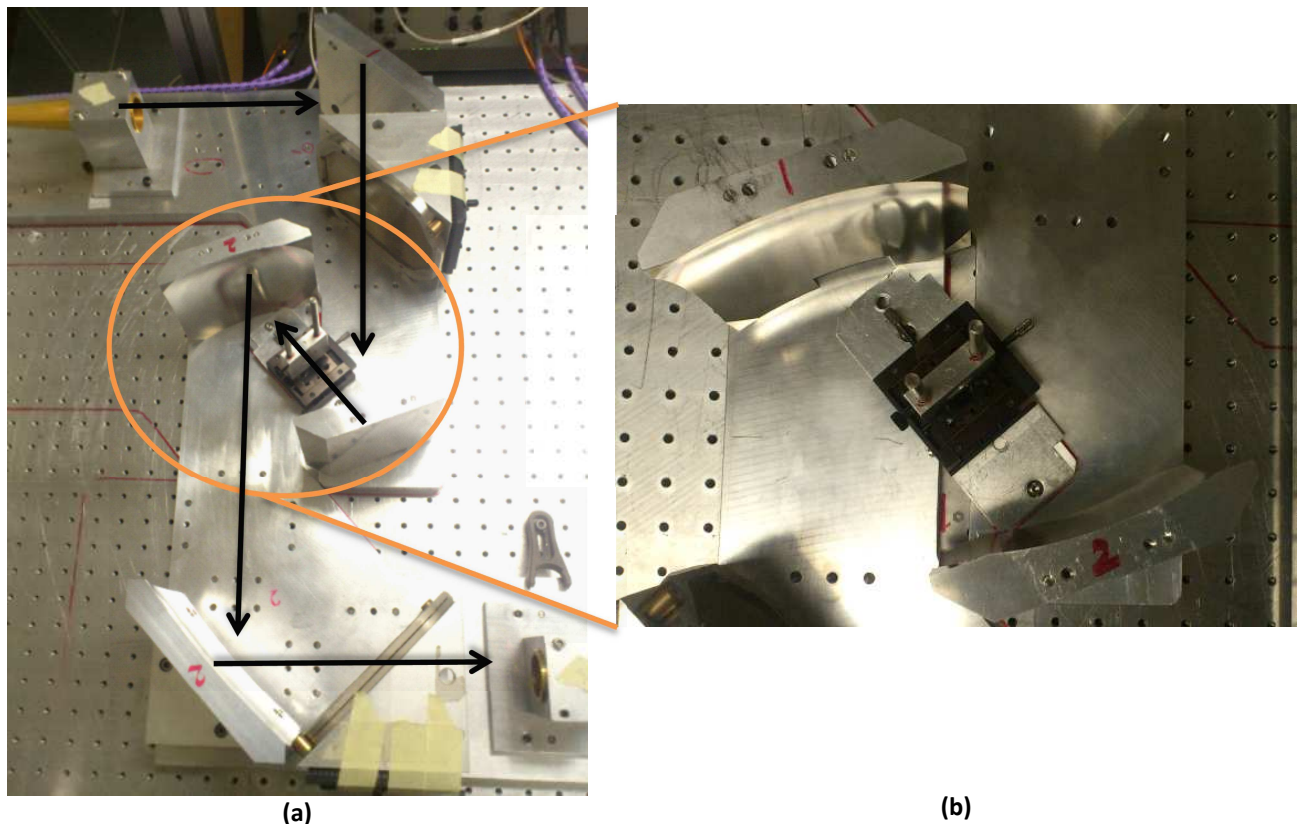


Figure 26: (a) Top view of quasi-optical “Z” test bench, used for the experiments in this project. The black arrows indicate the direction of propagation of the beam as it leaves Port 1 of the VNA to be received at Port 2 in order to measure S_{21} . (b) The middle part of the circuit which includes the sample holder.

Quasi-optical circuits such as the “Z-bench” shown above are designed using Gaussian beam mode analysis, which this project doesn’t cover. **Gaussian beam mode analysis** refers to the use of formulas (and experimenting) to predict the form of the beam travelling through the circuit depending on the frequency in use. Such analysis can be used to identify the location of the beam waist and its dimensions in order to place the sample in that position. Placing the sample at the beam’s waist ensures that all of the power from the source passes through it. By knowing the beam waist’s dimensions it is possible to make sample holders with the right diameter to ensure the entire focused beam passes through it. Creating another beam waist at the aperture of the second feed horn by reflecting the beam again after it passes through the sample ensures that the entire signal (which hasn’t been reflected from the sample) is fed back into the receiving end (Port 2) of the VNA in order to make accurate S-parameter measurements. If the beam waist lies before the second feed horn’s aperture, then diffraction effects will cause the beam to diverge and result in a portion of the transmitted beam being lost, thus affecting result accuracy.



Figure 27: 2 of the curved reflectors on both sides of the sample holder. The reflectors focus the beam in such a way that its re-focused beam waist lies exactly on the hole in the middle of the sample holder. The diameter of the hole where the sample is placed is designed (using Gaussian beam mode analysis) so that the entire signal passes through.

This brief overview of QO circuits brings an end to the discussion of the transmissometer which is the complete system where experiments in this project are to take place.

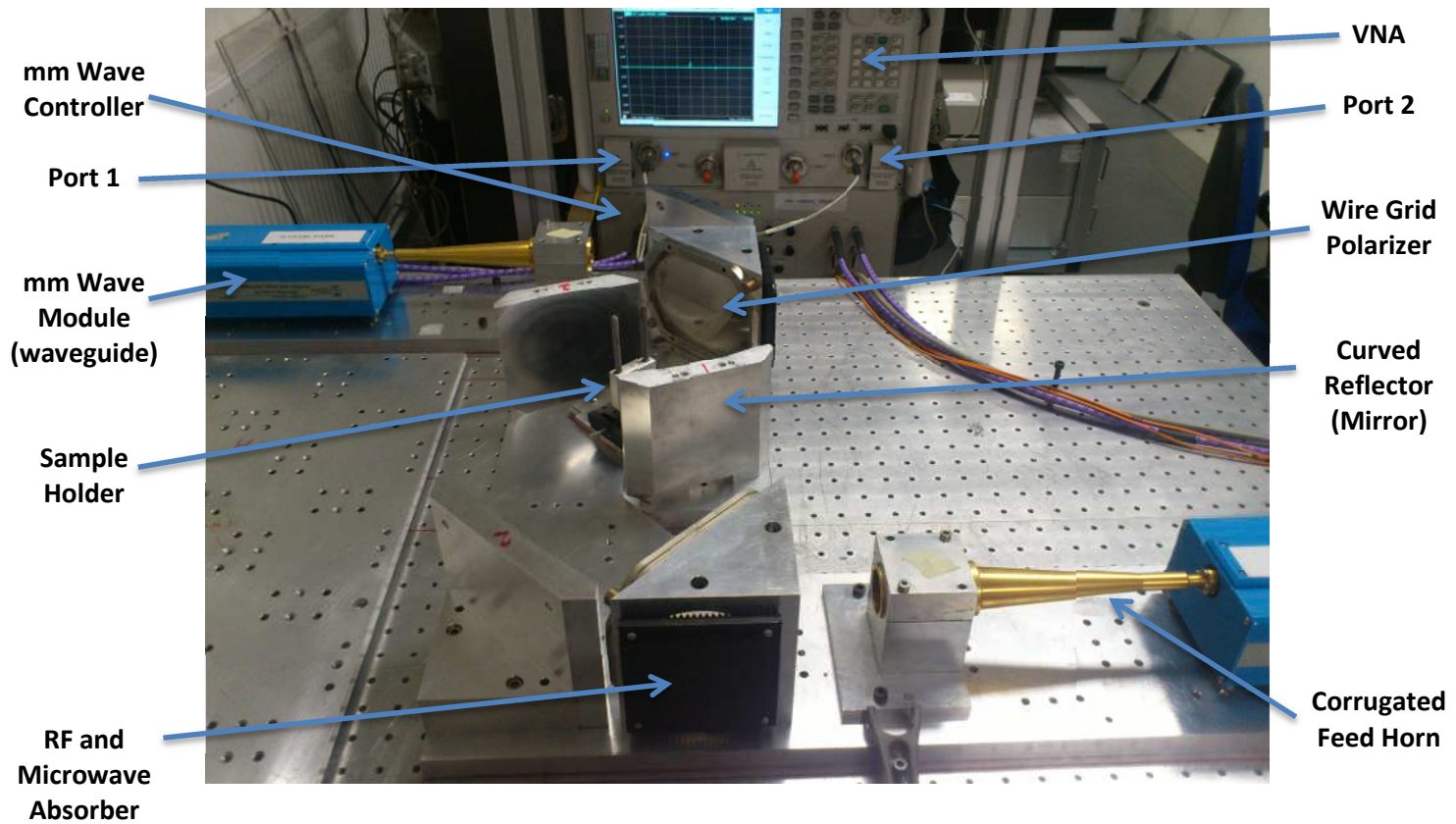


Figure 28: The transmissometer (QO circuit + VNA) used for all experiments in the project. Labels on the right and left indicate components of the transmissometer discussed previously in this section.

The transmissometer pictured in **Figure 28** was used to measure the refractive index of enamel samples at various stages of de-mineralisation. The experimental procedure is detailed in the following section of the report.

Implementation and Results

This project consisted of 4 experiments:

1. A thin cross section of the scattering phantom; **Frequency sweep:** 220 -320 GHz.
2. 3 sound (healthy/non-de-mineralised) enamel samples; **Frequency sweep:** 75 -110 GHz.
3. 1 enamel sample de-mineralised for a duration of 1 hour; **Frequency sweep:** 75 -110 GHz.
4. 3 enamel samples de-mineralised for a duration of 5 hours; **Frequency sweep:** 75 -110 GHz.

The first two experiments were conducted by the research assistant without my presence. This was because the system was booked for measurements for research purposes or for private companies and the exact time that my samples were to be measured could not be told. I had the chance to be there for the third and fourth experiments and hence the experimental procedure for these is slightly more detailed. The choice of the frequency sweep depended on the millimetre wave heads that were present at the time of the experiment which had been used by whoever was using the system before.

1) Scattering phantom cross section:

The first sample tested on the transmissometer was a thin cross section of a scattering phantom. As mentioned earlier on in the report, scattering phantoms are used to calibrate OCT machines and they are designed to have uniform scattering characteristics.

Due to the availability of only one phantom at the lab in the School of Medicine and Dentistry, a cross section of it was obtained in order to return it to the lab. This was acceptable since the phantoms are designed specifically to have a uniform scattering structure (and hence refractive index) throughout. The cross section was taken using a machine called a *lathe* in the mechanical workshop of the university and had a thickness of about 2 mm.



Figure 29: Scattering phantom cross section used for measurement (left) and original phantom used for OCT calibration (right).

The thin cross section was studied under a **profilometer** in the materials laboratory. The profilometer has an extremely sensitive stylus which traces out a graph on the screen as it moves over the surface.



Figure 30: The profilometer used to trace out the phantom's surface shape.



Figure 31: The stylus of the profilometer as it moved across the surface of the phantom.

A roughness scan of its surface showed a concave shape on one side and a convex shape on the other side which is a result of the cutting process when the cross section was taken from the original scattering phantom.

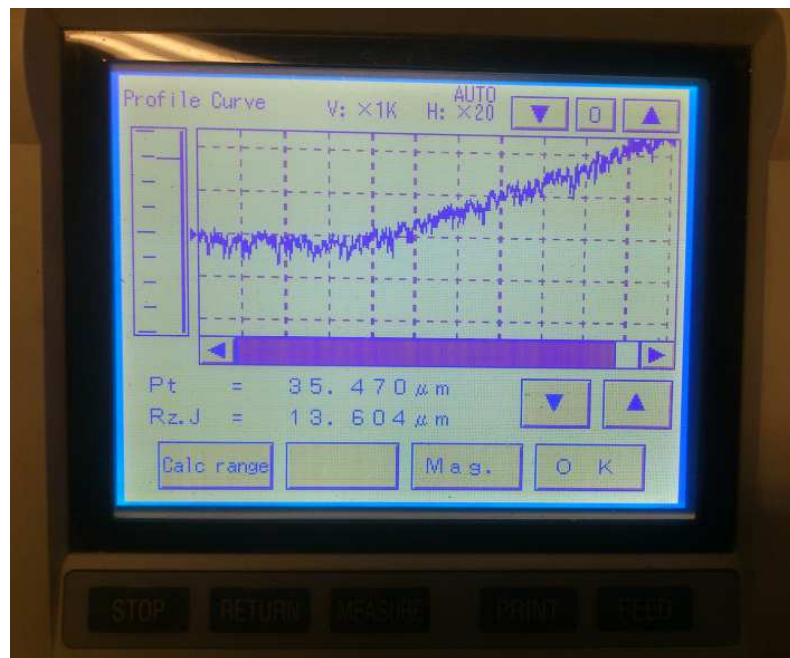


Figure 32: The profilometer's flatness scan result as the stylus travelled halfway across the diameter of the phantom showing the convex shape of the edge.

Figure 32 above shows the result of the scan across the surface of the phantom on one side. This was the side that had a convex shape which, even though invisible to the eye, could be picked up to the stylus which is sensitive to dents as small as 10 nm. The convex shape on one side, coupled with the concave shape on the other side result in non-parallel sides of the phantom. Since parallelism is important in transmission mode spectrometry, control over this factor may have effects on measurement results. More details on how this factor can be controlled are discussed in the “Discussion and Analysis of Results” section of the report.

The cross section of the phantom was also taken to the School of Biological and Chemical Sciences to be studied under a confocal microscope in order to obtain images of the phantom's structure on the inside.

In addition to obtaining a single image of the surface of a sample, the microscope has a feature called the “Z stack” which operates in a similar manner to OCT. This functionality allows images to be taken at different optical layers of the sample which can be played back into an animation which shows how the structure of the sample changes with depth. This could be used, perhaps to understand how the titanium dioxide particles are structured within the epoxy resin matrix and how homogenous they are. If the particles are homogenous enough then measuring the refractive index of the cross section will be identical to measuring that of the original phantom. It could also be used to look at the structure of enamel samples just like OCT. However, the limitation to this is the size of the sample placed in the microscope. The phantom cross section was too big to show any clear images and with large samples only a 10 x magnification is possible. The lab technician suggested I come back to her with just a tiny piece of the phantom, even if it was so small that forceps are needed to pick it up. Smaller samples allow magnification to take place up to 60 x due to the ease of causing fluorescence of the particles using any of the available lasers with varying excitation wavelengths.

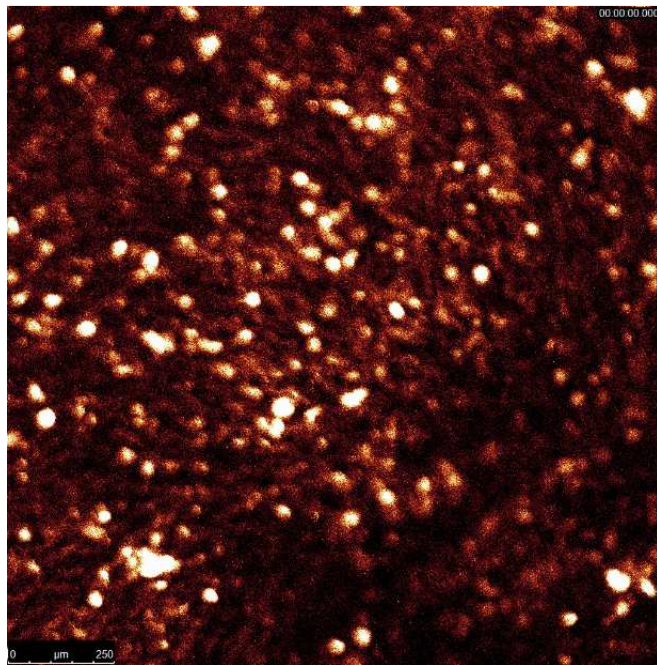


Figure 33 (above): The surface of the phantom, magnified 10 x. The white dots may represent the Titanium oxide particles. According to the lab technician, the image is very poor due to the large size of the phantom (both thickness and diameter). This magnification was achieved after using a 633 nm wavelength helium-neon laser to trigger some fluorescence.

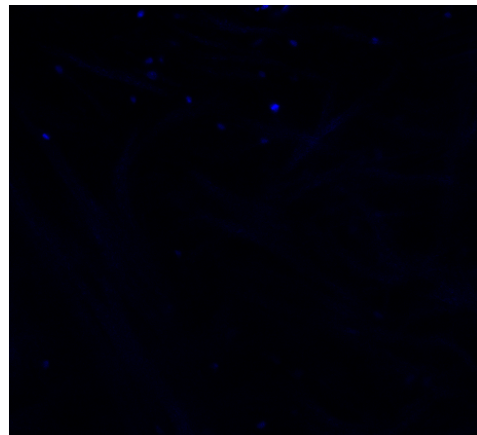
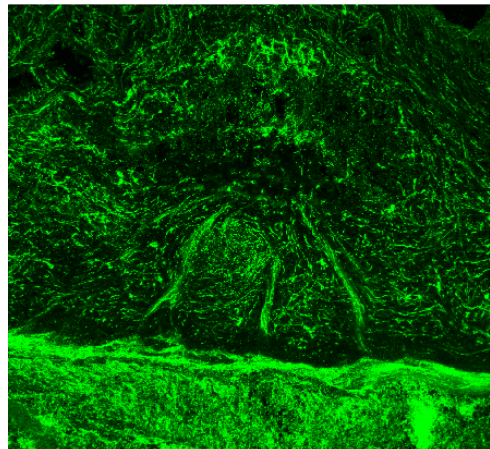


Figure 34 (right): 2 of the images taken of the phantom by the "Z stack function." The image outputs from the microscope are stored in a '.lif' file which can be opened after installing the appropriate tools by software such as ImageJ.



Before starting the measurement and just after the quasi-optical circuit was set up with the cables from the VNA's ports connected to the millimetre wave heads and the corrugated horns fitted, calibration of the VNA was necessary to eliminate background effects on the measurements. By running a "**Continuous**" frequency sweep for a couple of times and then running a "**Single**" sweep, the S_{21} values were placed on "**Hold**". These values were then saved to the VNA's memory by pressing the "**Data > Memory**" button. After that, pressing "**Normalize**" divides any S_{21} value by the corresponding value in the "**Memory**" (which contains S_{21} background data) resulting in a gain of 1 (or 0 dB). Returning to the "**Continuous**" frequency sweep showed a constant S_{21} magnitude of 0 dB throughout the frequency range indicating that it is OK to start the measurements.

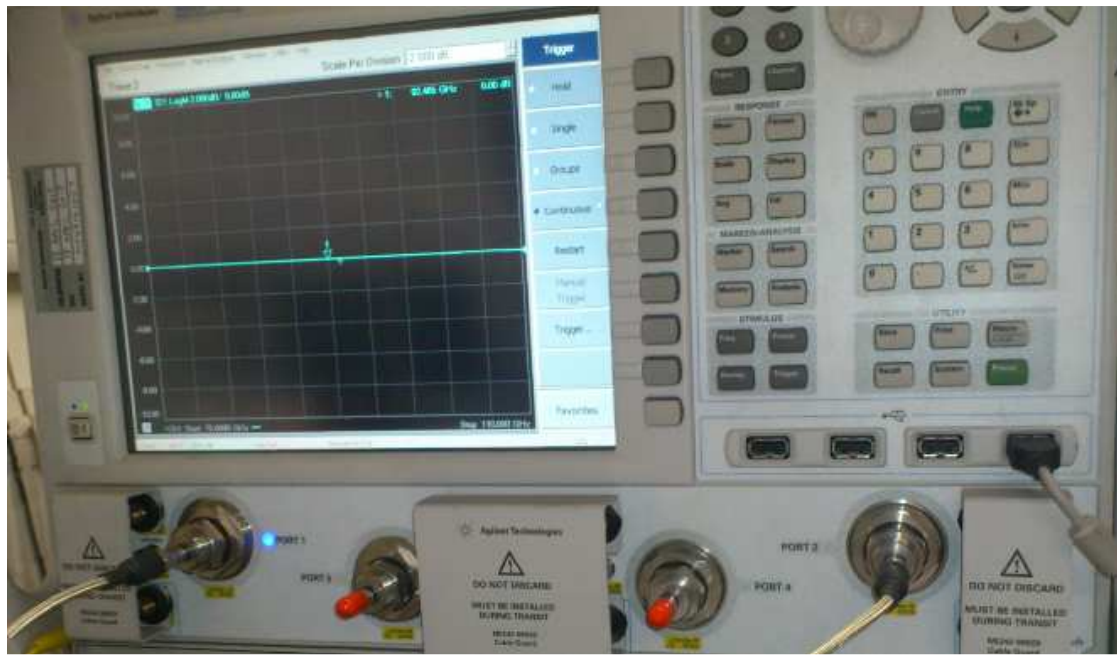


Figure 35: Photo of the VNA display after calibration with 0 dB being the reference plane for the measurements.

The sample was placed in the middle of the circuit and a S_{21} frequency sweep between 220 and 320 GHz was done for 3 times. The results were saved as *Comma Separated Variables* (.csv) which could be opened later on as an Excel spreadsheet.

	A	B	C	D
1	!CSV A.01.01			
2	!Agilent Technologies	N5244A	MY49141007	A.09.42.16
3	!Agilent N5244A: A.09.42.16			
4	!Date: Friday	January 11	2013 15:58:01	
5	!Source: Standard			
6				
7	BEGIN CH1_DATA			
8		Freq(Hz)	S21(DB)	S21(DEG)
9		2.2E+11	-2.7728586	10.034515
10		2.20053E+11	-2.7851591	10.00552
11		2.20105E+11	-2.7919421	9.9680996
12		2.20158E+11	-2.7969818	9.806922
13		2.2021E+11	-2.7958348	9.8173113
14		2.20263E+11	-2.8033214	9.7204828
15		2.20315E+11	-2.8102179	9.7129059
16		2.20368E+11	-2.8071167	9.5830221
17		2.2042E+11	-2.8100111	9.5619888
18		2.20473E+11	-2.8097286	9.5383215
19		2.20525E+11	-2.8047729	9.4390688
20		2.20578E+11	-2.8208272	9.3322372
21		2.2063E+11	-2.8149631	9.3787489
22		2.20683E+11	-2.804877	9.1937342
23		2.20735E+11	-2.8199573	9.0412235
24		2.20788E+11	-2.832737	9.1131039
25		2.2084E+11	-2.8137407	9.0274162

Figure 36: Excel spreadsheet containing S_{21} frequency sweep (220 – 320 GHz) data of the scattering phantom cross section.

The first column in the spreadsheet titled **Freq(Hz)** contains all the frequencies probed by the VNA resulting in an S_{21} response from the sample. The frequency range depends on the millimetre wave heads used in the quasi-optical circuit set-up and the step size depends on the scaling which was manually entered onto the VNA at the beginning of the experiment. For this experiment, the step size was 50 MHz, resulting in a total of 2001 frequencies at which the complex S_{21} value is stored in the other 2 columns: **S21(DB)**, which contains the magnitude in decibels and **S21(DEG)** which contains the phase angle in degrees.

The same frequency sweep was run 3 times and so the average of the three trials was taken and saved in a separate spreadsheet. In order to use this data in the refractive index calculation, it was imported into Matlab and saved in '.mat' format as three separate column vectors.

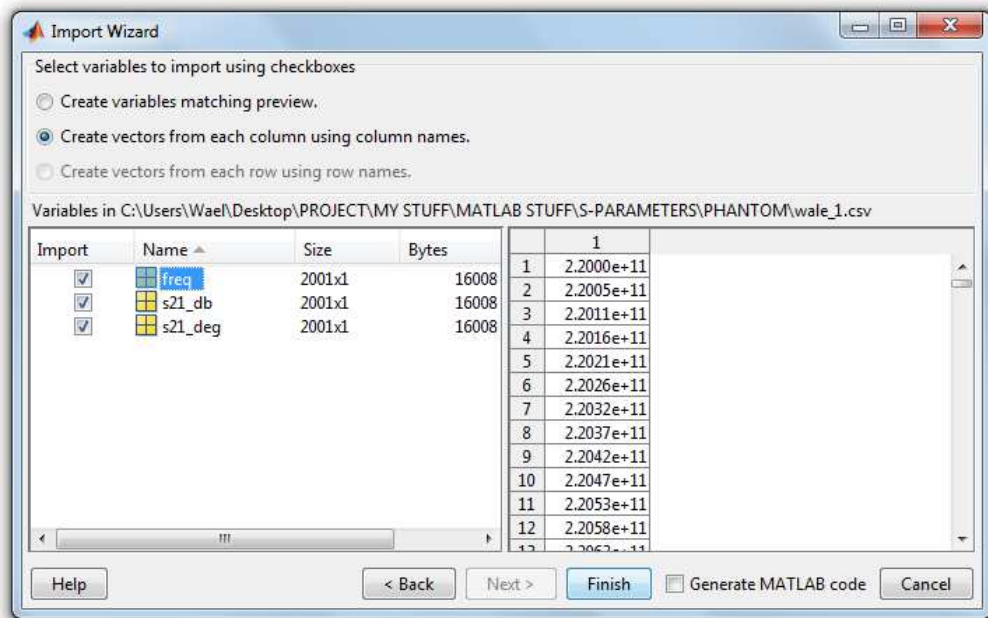


Figure 37: Importing the VNA data into Matlab from the Excel spreadsheet.

The three variables were renamed into **freq**, **s21_db** and **s21_deg** and added to the Matlab variable workspace.

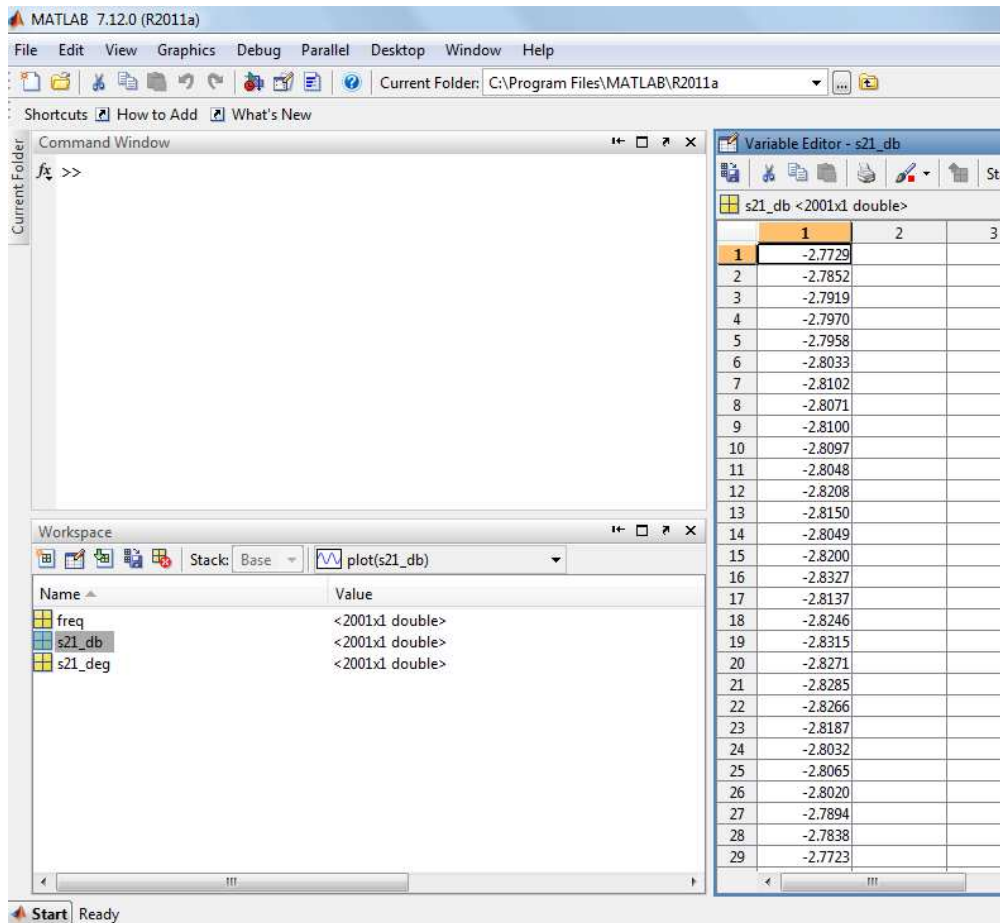


Figure 38: The three column vector variables in the Matlab workspace, imported from the Excel file generated by the VNA. Each of the three variables is a single column containing 2001 rows.

After importing the variables were imported, they were saved as a '.mat' file which could be loaded later on into the Matlab scripts at any time and used for processing.

Re-calling what was mentioned previously in the 'Background Theory' section, the basis of dielectric property extraction using the transmissometer lies in two properties called the '**Transmittance**' and '**Reflectance**' of the material. Transmittance and Reflectance are both frequency dependent and they can be found using the formulae below:

$$\text{Transmittance: } t_{\pm}(\omega) = \frac{(1 - r_{1\pm}^2)e^{i(\omega/c)n_{\pm}(\omega)d}}{1 - r_{1\pm}^2 e^{i2(\omega/c)n_{\pm}(\omega)d}}$$

$$\text{Reflectance: } r_{\pm}(\omega) = \frac{r_{1\pm} - r_{1\pm} e^{i2(\omega/c)n_{\pm}(\omega)d}}{1 - r_{1\pm}^2 e^{i2(\omega/c)n_{\pm}(\omega)d}}$$

In the formulae on the previous page ω is the angular frequency of the electromagnetic (Gaussian) beam, c is the speed of light in vacuum ($\approx 3 \times 10^8$ m/s), d is the thickness of the sample and n is its (frequency dependent) refractive index. r_1 is given by:

$$\text{Single face reflectance: } r_{1\pm}(\omega) = \frac{Z_0 - Z_{\pm}(\omega)}{Z_0 + Z_{\pm}(\omega)}$$

where Z_0 , the normalised free space wave impedance is 1 and $Z(\omega)$ is $\sqrt{\frac{\mu_r(\omega)}{\epsilon_r(\omega)}}$ where μ_r is equal to 1 in non-magnetic materials.

Transmittance/Reflectance can also be obtained experimentally using S parameter values:

$$\text{Transmittance} = S_{21} \text{ (complex)} e^{j\omega d/c}$$

$$\text{Reflectance} = S_{11} \text{ (complex)} e^{j\omega d/c}$$

Thus, a graph of transmittance or reflectance against frequency can be plotted by either using S-parameter data or by using the formulae which are dependent on the refractive index and hence permittivity (and permeability). The value of complex permittivity at each frequency which results in a transmittance/reflectance graph similar to that plotted using S-parameters is thus the permittivity of the sample at that particular frequency.

The first program I wrote gives an estimated permittivity value for all frequencies which results in the closest approximation of both theoretical (using the formulae) and experimental/measured (using S_{21} data) transmittance graphs. The post-doctoral research assistant who supervised the experiments mentioned that for low-loss materials which generally tend to be solid and non-magnetic, the magnitude of the transmittance depends on both the real and imaginary parts of the complex relative permittivity while the phase of the transmittance depends on only the real part of the permittivity. Thus, by comparing measured transmittance phase against multiple theoretical transmittance phases, each computed with a different real part (ϵ_1), it was possible to find out the value of ϵ_1 which provided the closest least-squares approximation to the measured transmittance.

After the value for ϵ_1 was 'cracked', the transmittance magnitudes were compared in a similar manner but this time by making ϵ_{11} into a range and using the cracked value for ϵ_1 . The code is attached in the "Supporting materials" folder under the name "dielectric_property_calculator.m" which can be opened using Notepad (and Matlab). The code is also present in Word format in order for the comments (in green) to be visible as they explain the process in more detail.

Running the program in the Matlab command prompt opens a window where the '.mat' file containing frequency and S_{21} data is selected:

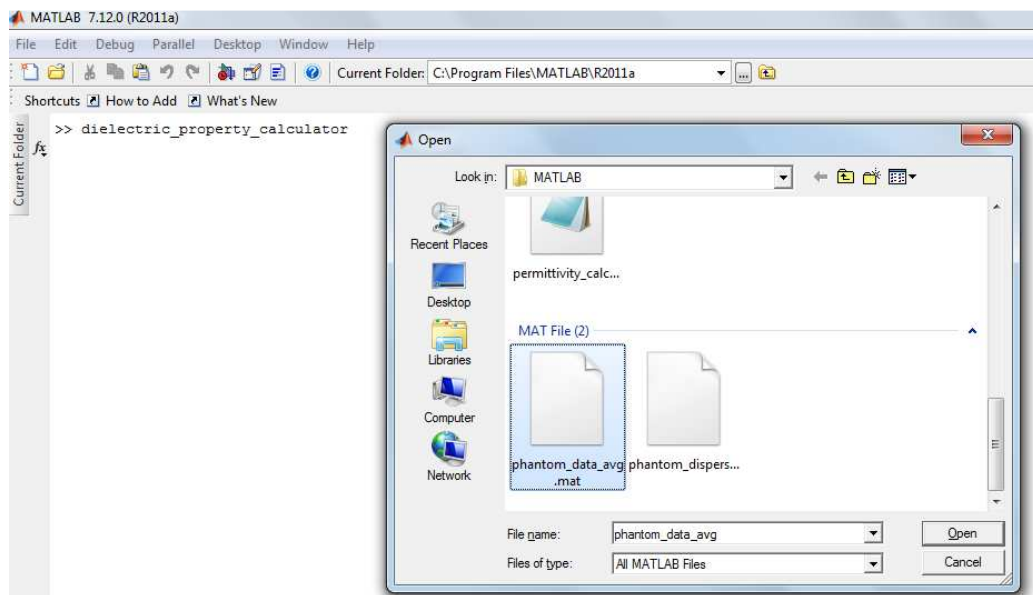


Figure 39: Using S_{21} data from the VNA in the Matlab code.

After the file is selected, the program asks for the sample thickness as measured by the micrometre (**1.863 mm**) in the lab. Entering the thickness in millimetres causes the program to run for a few seconds before giving two outputs. The first output is the complex relative permittivity of the sample selected from both ranges of ϵ_1 and ϵ_{11} (0 - 50 and 0 - 5 respectively) which results in the closest approximation of the theoretical transmittance function to the measured one. As shown in the screen-shot below, this value was 2.925 for ϵ_1 and 0.09 for ϵ_{11} .

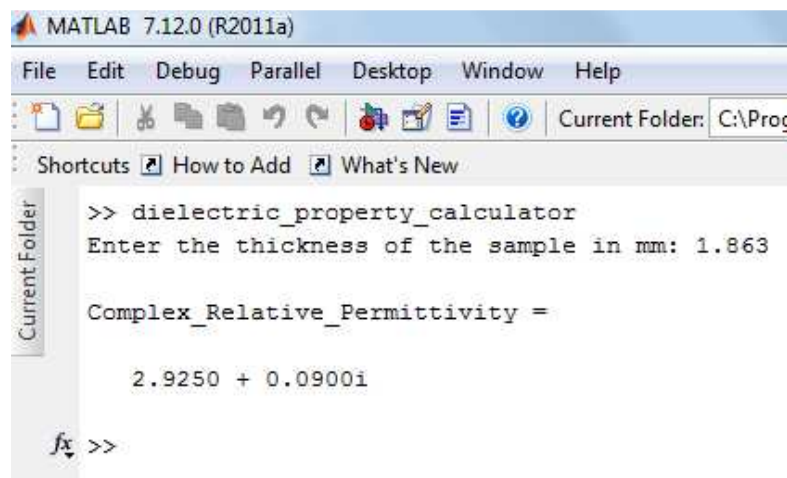


Figure 40: First output of the program (complex permittivity).

The second output is the graphs for the measured sample transmittance and the theoretical transmittance evaluated using this permittivity value. Both transmittances are separated into magnitude and phase to enable plotting, with the red graphs corresponding to measured transmittance and the blue graphs corresponding to theoretical transmittance data.

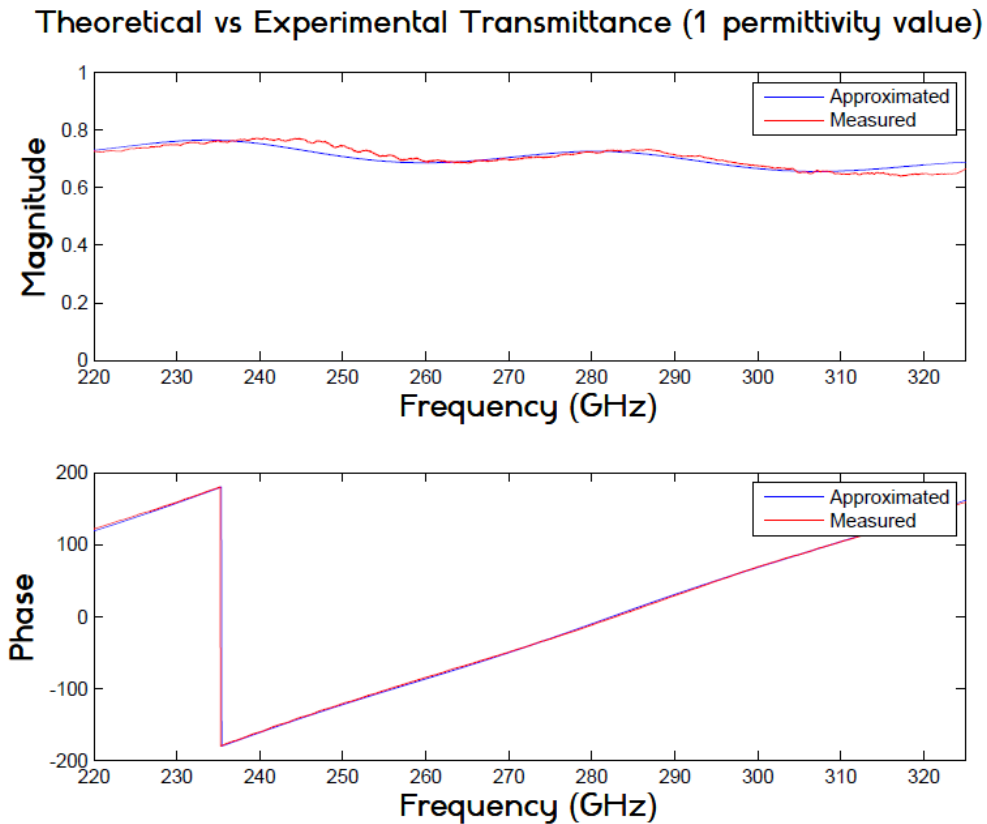


Figure 41: Second output of the program. The blue graphs correspond to theoretical transmittance evaluated using $\epsilon_r = 2.925 + j0.09$ and the red graphs correspond to the measured transmittance evaluated using S_{21} data of the sample obtained from the VNA.

To get a closer value for the permittivity, a second program (**dpc_manual.m**) was written to allow the user to manually enter the ranges for ϵ_1 and ϵ_{11} to compensate for the large and ambiguous range in the previous program by adding the following lines:

```
er_1_low = input('Enter the lower boundary of epsilon 1: ');
er_1_high = input('Enter the upper boundary of epsilon 1: ');

er_2_low = input('Enter the lower boundary of epsilon 2: ');
er_2_high = input('Enter the upper boundary of epsilon 2: ');
```

Based on the previous output of the program, the limits could be made smaller in order to get a closer estimate. The screenshot to the right shows the result of running this program using the user-defined limits.

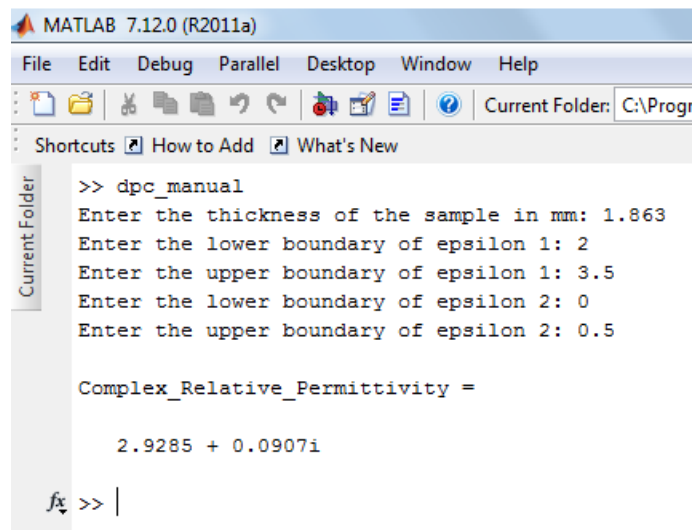


Figure 42: First output of the second program in which the user inputs the permittivity limits for ϵ_1 and ϵ_{11} manually.

The output of this program shows an increase in the number of significant figures for both the real and imaginary parts of the complex permittivity.

The two programs so far only give a rough estimate for the permittivity of the sample at all of the given frequencies. In reality, however, the permittivity varies with frequency even if by low amounts. The third (and most important) program I wrote uses a different method to obtain the permittivity at each and every frequency in the VNA's S_{21} sweep. The method of using phase data to estimate the real part of permittivity and the magnitude data for the imaginary part also worked using this program, but since that holds true only for lossless/low-loss materials, I wrote a program that could work for any type of sample.

This was achieved by using the least-squares approximation not for phase and magnitude data separately, but for both experimental and theoretical complex transmittances. The real and imaginary parts of permittivity limits are set according to the outputs of the previous program with the step size set to 50 steps. This results in 51 different values for ϵ_1 and 51 different values for ϵ_{11} . Using all possible combinations of these values, $\epsilon_r = \epsilon_1 + j \epsilon_{11}$ was made into a range of $51^2 = 2601$ different values. Each value of ϵ_r was used to compute the theoretical complex transmittance at every frequency and compared to the measured complex transmittance at that frequency to find the value of ϵ_r , i.e. the complex permittivity of the sample at that particular frequency.

Choosing to make the step size 50 was due to Matlab freezing due to the large amounts of matrices it has to process at any value above 50. Even with this range it takes at least 20 minutes for the program to run. The code is attached under the name "**dispersive_perm_calc.m**" and differs from the other two. This code is a Matlab script instead of a function. Thus, loading the S_{21} data and entering the thickness have to be done from within the code as it doesn't give an option to choose the '.mat' file or enter the neither the sample thickness nor the permittivity limits.

The first output of the program is a similar graph of theoretical and measured transmittance, shown below:

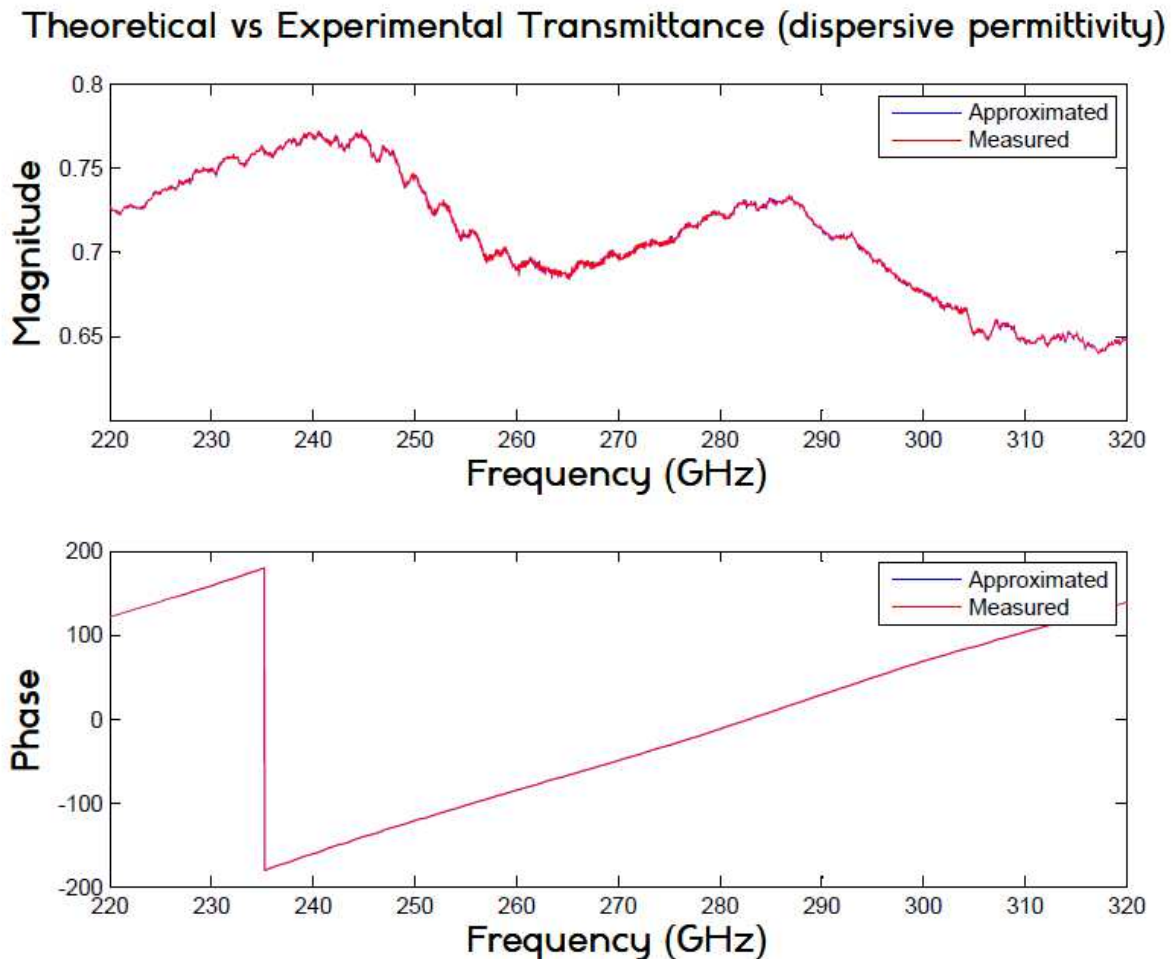


Figure 43: First output of the program used to calculate the permittivity of the scattering phantom across the 220 – 320 GHz frequency range. The blue graphs correspond to the magnitude and phase of the complex theoretical transmittance calculated using the ‘approximated’ complex permittivity of the phantom at every frequency. The red graphs correspond to the magnitude and phase of the complex measured transmittance calculated using the value of S_{21} at every frequency within the range. The very close overlapping of the blue and red graphs (compared to that of the previous program) indicates the accuracy of this fitting technique.

The second and third outputs show both the real and imaginary parts of the complex relative permittivity and refractive index of the scattering phantom cross section for the given frequency range.

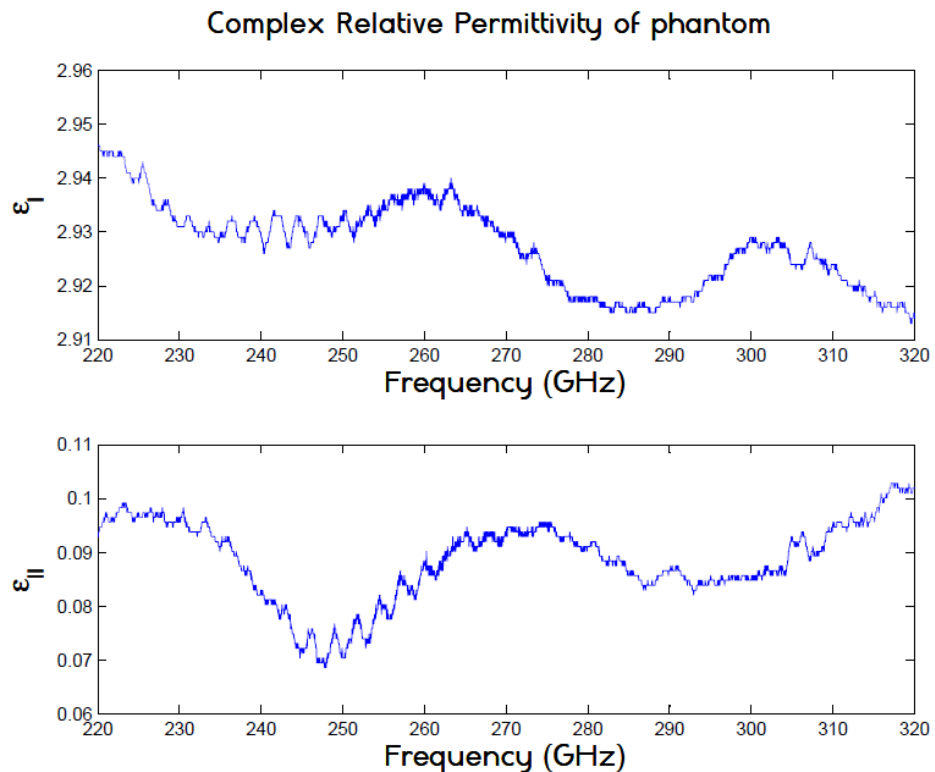


Figure 44: Second output of the program showing the changes in the real (ϵ_1) and imaginary (ϵ_{11}) parts of the complex relative permittivity of the scattering phantom cross section between 220 and 320 GHz.

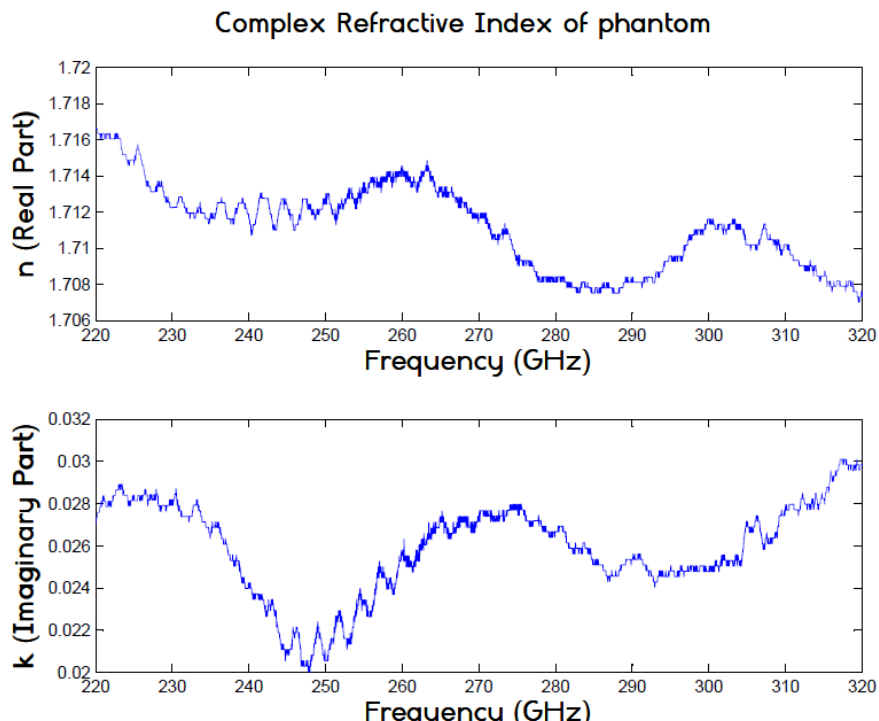


Figure 45: Third output of the program showing the changes in the real (n) and imaginary (k) parts of the complex refractive index of the scattering phantom cross section between 220 and 320 GHz.

According to [75], the most accurate values for the refractive index are those evaluated at the peaks and troughs of the measured complex transmittance magnitude/ S_{21} data. The number of peaks and troughs present depends on the thickness of the sample and its permittivity. Thinner samples or samples with high permittivities exhibit higher oscillations in their S_{21} graphs seen on the display of the VNA. For the final part of the analysis, I wrote a program to plot the calculated complex refractive index (magnitude and phase) only at the frequencies where peaks and troughs of the measured complex transmittance magnitude are present.

This requires saving all necessary variables that were a result of the previous program into another '.mat' file. The program then plots the measured complex transmittance magnitude, to assist the user in determining the location of the first peak. The user enters the upper frequency limit where the lower limit is the starting frequency and the peak is located somewhere in between. The program locates the frequency at which there is a peak value of the transmittance magnitude and displays it to the user. After displaying the location of the first peak, the user is asked to enter the upper frequency limit for finding the first trough and displays the frequency at which the trough occurs to the user. The program then asks the user to enter the total number of peaks and troughs visible in the transmittance magnitude graph. Since the period is roughly the same between peaks and troughs the program uses this to locate the frequencies at which all peaks and troughs are present. Refractive index is then plotted at these points and displayed. The code for this program is attached under the name "**peak_trough.m**".

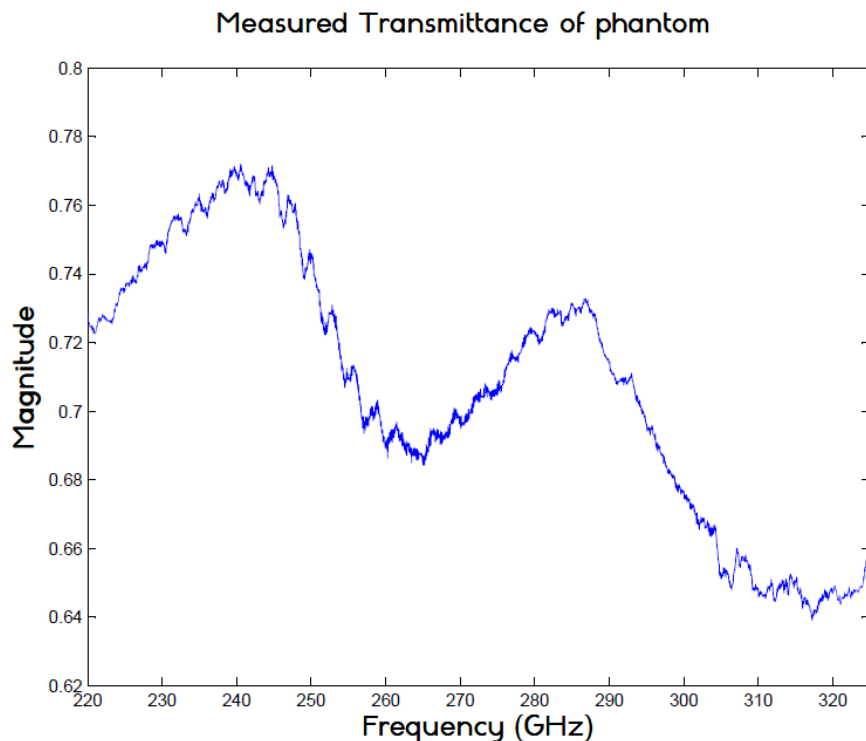


Figure 46: The first output of the program, which is the magnitude of the measured complex transmittance of the scattering phantom, to assist the user in determining the number of peaks and troughs and the location of the first peak in order for the program to extract the refractive index of the phantom at these points.

```

>> peak_trough
Enter the upper frequency limit (in GHz) for finding peak: 260

Frequency of first peak is around: 241 GHz.

Enter the upper frequency limit (in GHz) for finding trough: 280

Frequency of first trough is around: 265 GHz.

Enter the total number of peaks and troughs in transmittance graph: 4
fx >>

```

Figure 47: Screen-shot of the program outputs. After the graph in **Figure 46** is displayed, the upper frequency limit is requested. From the graph in **Figure 46**, the first peak occurs before 260 GHz and so that is entered. Then, the next upper frequency limit is requested in order to locate the trough which is displayed as well. From the same figure it is also visible that there are 4 peaks and troughs in total and so the value 4 is entered resulting in the graph shown in **Figure 48**.

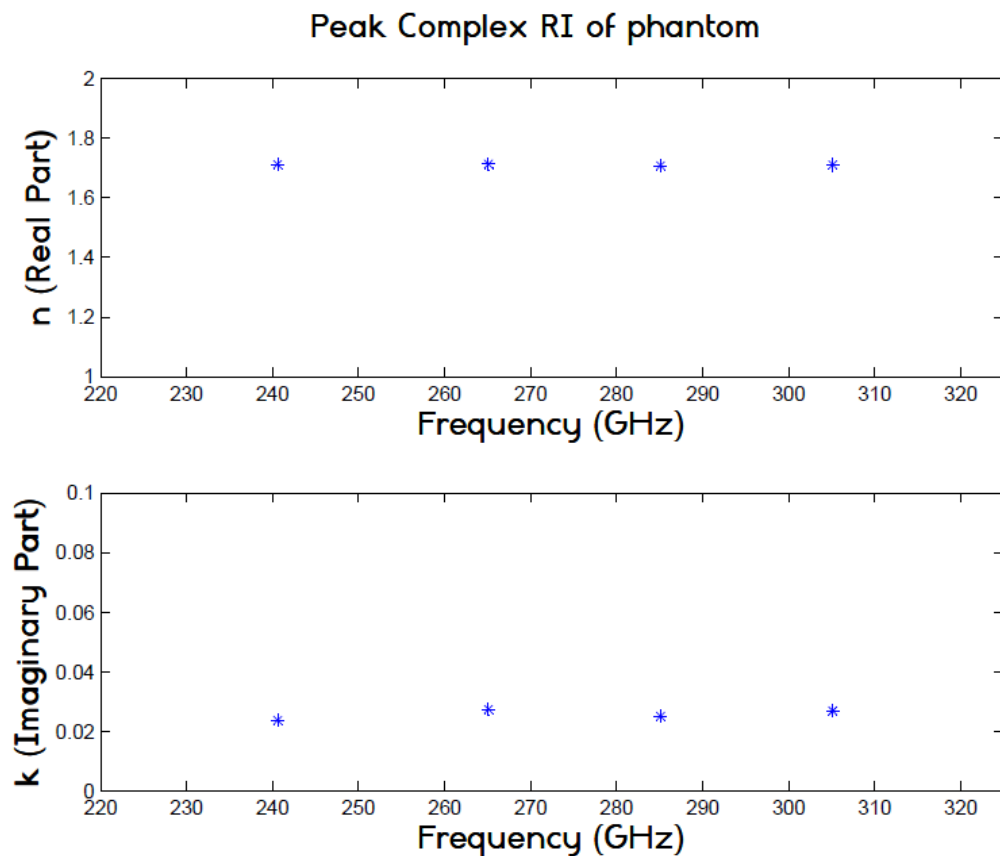


Figure 48: The last output of the program and the very final stage of the refractive index extraction process. It shows the real and imaginary parts of the refractive index of the scattering phantom cross section at 4 points between the 220 and 320 GHz range.

The analysis of the S_{21} data and extraction of the refractive index of the phantom which has been described for this experiment was used for all forthcoming experiments and hence from here forth, only the final refractive index results of this process will be shown. There are, obviously, some minor changes that needed to be made when using these 4 programs for the other 3 experiments but any changes that needed to be made are indicated.

2) Three sound enamel samples:

The second experiment consisted of conducting measurements using three sound enamel samples. The acid used for de-mineralisation was not available at the time of the measurements and so the results obtained are only useful in getting an idea about the refractive index of healthy enamel.



Figure 49: Enamel samples used for this experiment, labelled 1, 2 and 3 on the sides in order to distinguish between obtained results.

Using the same programs and with thicknesses of **4.271, 4.156 and 4.423 mm** for samples 1, 2 and 3 respectively, the refractive index of these samples between 110 and 170 GHz was calculated. As mentioned before, due to Matlab freezing at anything above 2601 combinations of ϵ_1 and ϵ_{11} , this was compensated by running the program multiple times and narrowing the range each time in order to get the most accurate results.

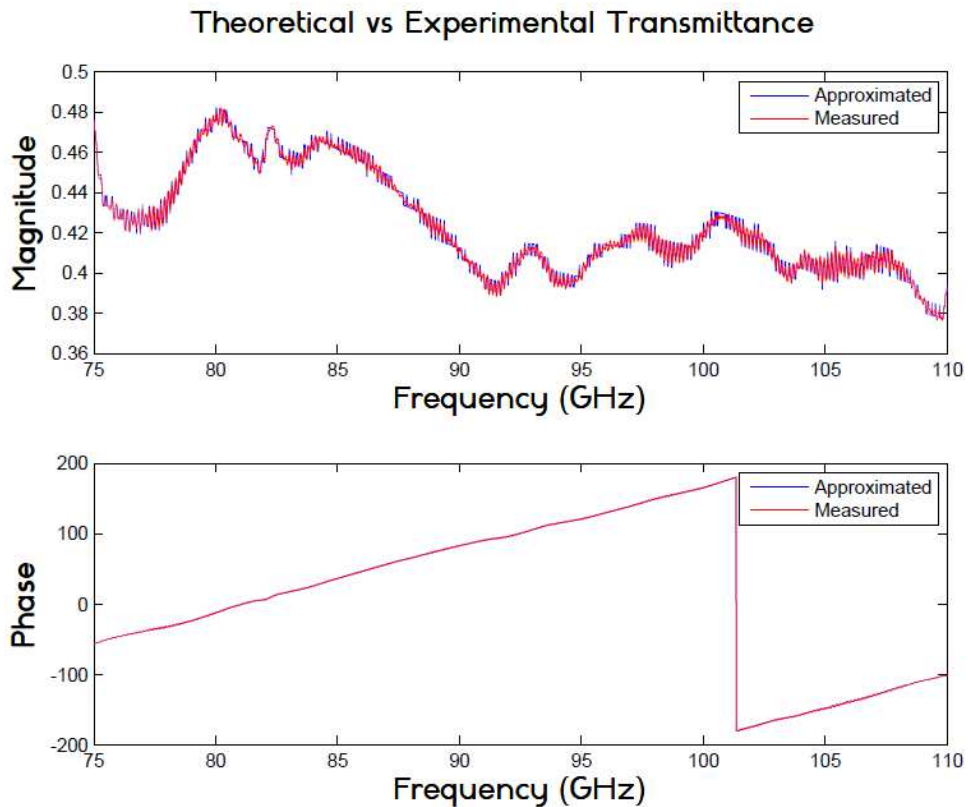


Figure 50: The theoretical (blue) and measured (red) transmittance graphs of Sample 1 after the fitting process. The final range used to fit the theoretical graph onto the measured graph was $2.94 - 3.04$ for ϵ_1 and $0.2 - 0.5$ for ϵ_{11} .

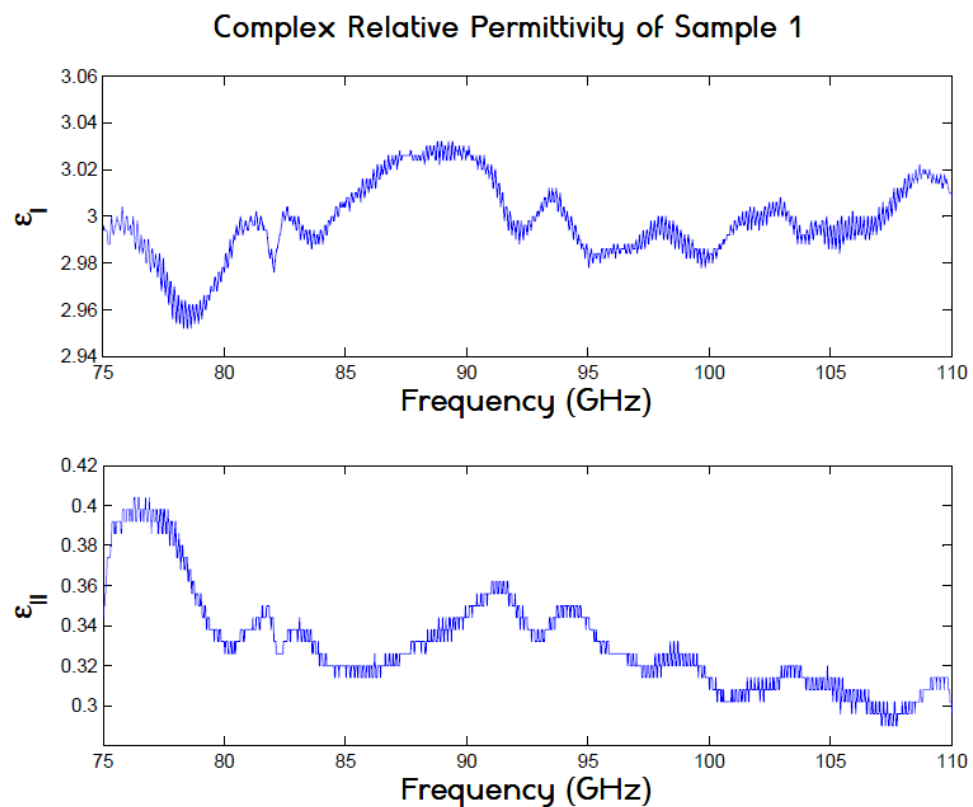


Figure 51: The dispersive (frequency dependent) complex relative permittivity of Sample 1, calculated as a result of the fitting process.

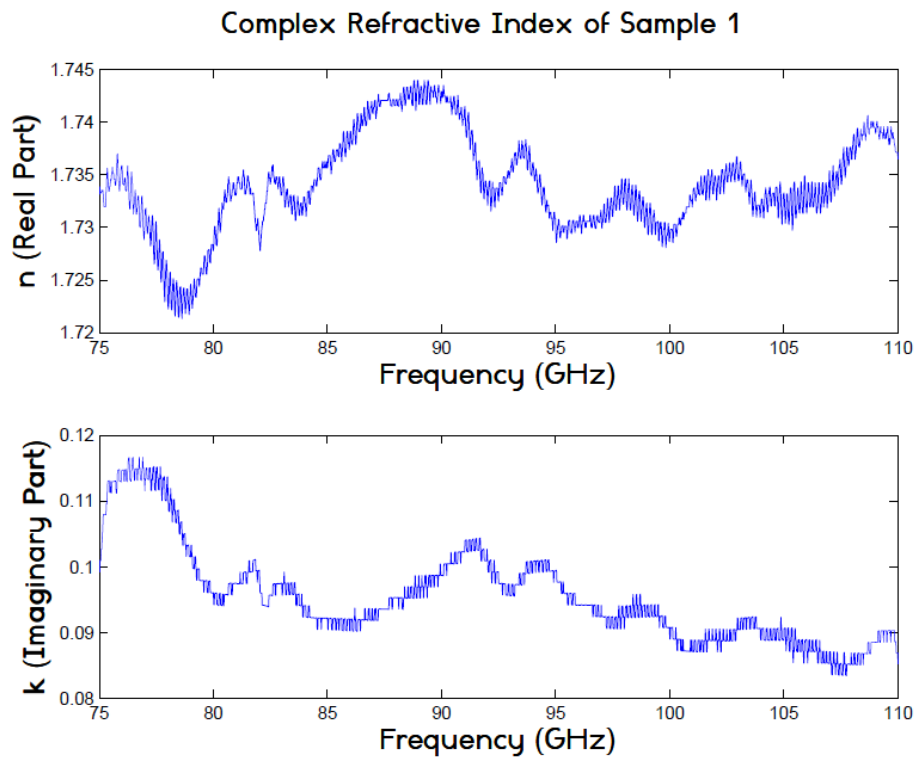


Figure 52: The dispersive (frequency dependent) complex refractive index of Sample 1, calculated as a result of the fitting process.

The same process was then repeated for samples 2 and 3. Due to the peaks and troughs not being evident in the transmittance graphs for all three samples, the refractive index graph was plotted as it is and not only at the maxima and minima. The method of extracting refractive index at the peaks and troughs of the measured transmittance/ S_{21} graphs works perfectly for thin samples. The thinner the sample the more oscillations are present and it is possible to obtain multiple values for the refractive index throughout the frequency range. The results of this experiment and of the next two experiments show an unidentifiable number of peaks and troughs, sometimes (as in the results for experiment 4) showing only one peak value throughout the frequency range. Thus, from here forth the refractive index for any sample will be plotted throughout the frequency range. If however, the samples were tested for a longer frequency range, more peaks and troughs would be visible and it would have been possible to use this technique (more in the next section of the report).

To compare the refractive indices of the three sound enamel samples, they were plotted on the same graph.

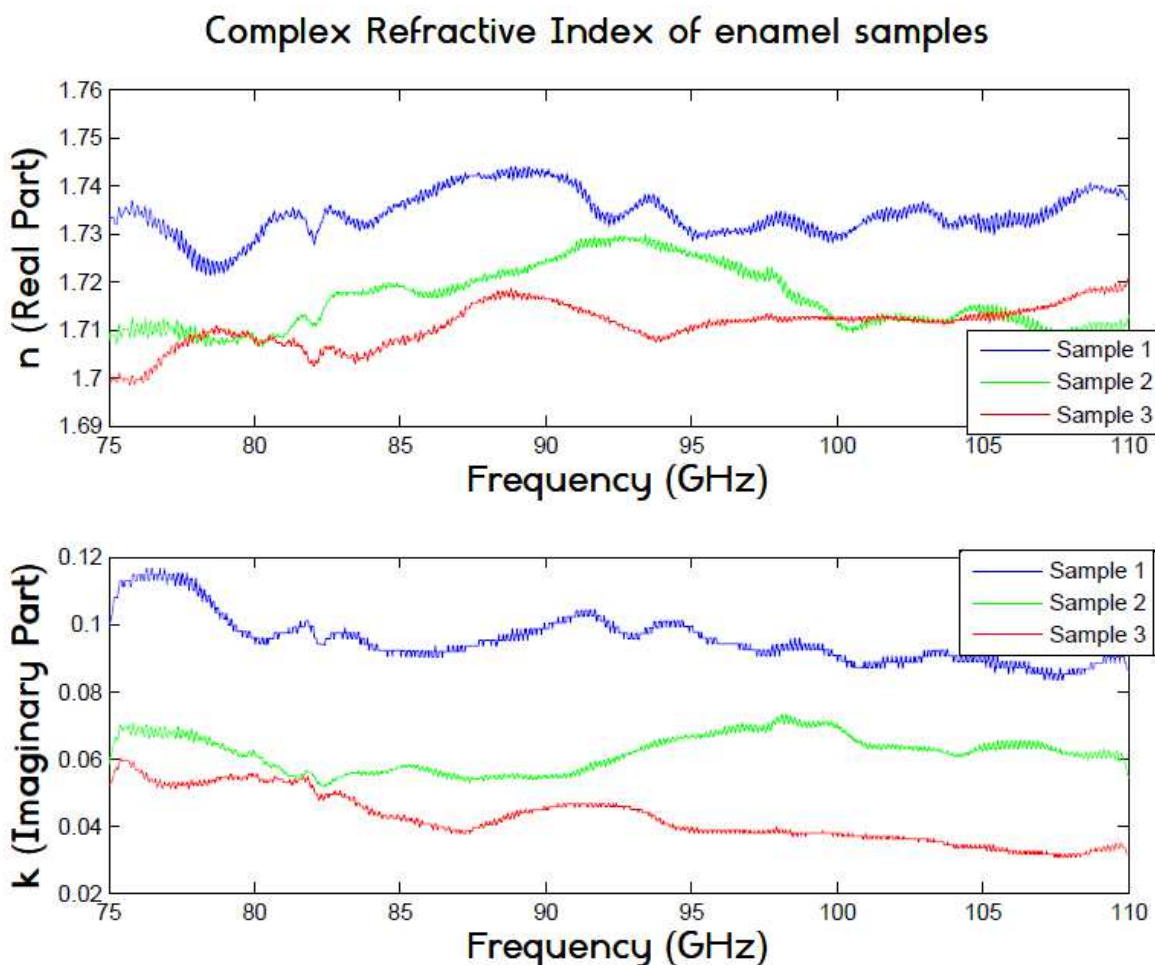


Figure 53: Complex refractive index of the 3 sound dental enamel samples: Sample 1 (blue), Sample 2 (green) and Sample 3 (red).

The imaginary part of the refractive index is related to the electromagnetic/light absorption properties of the material and is not of much importance in this project. Thus, to save page space the imaginary part is not plotted from here on.

3) One enamel sample with de-mineralisation (1 hour period):

The original plan was to use the previous three samples to study the de-mineralisation effect acid has on them but since they needed to be taken to the National Physics Laboratory for similar measurements using a Time Domain Spectrometer, another new enamel sample was acquired for the purpose of this experiment.

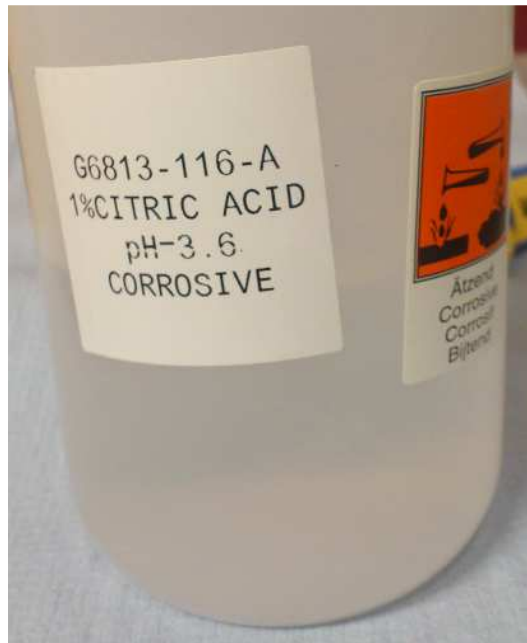


Figure 54: Acid used for this experiment (and the next one).

The sample holder within the quasi-optical circuit was much smaller in diameter to that of the enamel samples and thus for the previous experiments (enamel and phantom) the samples were stuck onto the holder using double-sided tape. This has the potential to greatly affect the accuracy of the measurements because the samples only contained enamel in the middle surrounded by a hard paraffin resin, as opposed to the phantom which was the same all over. This meant that any small displacement of the sample's position could alter the proportion of the beam passing through the enamel and hence affect the results. This was proven by visually monitoring the S_{21} graph displayed on the VNA as the sample was gently displaced by a few millimetres to the right, left, up and down which resulted in very evident changes. Since this was bound to happen due to having to constantly remove the sample in order to apply the acid, making the sample fit into the sample holder was a must.

Ideally, the sample would be precisely cut using some sort of diamond-edged tool/saw until their diameter fits that of the sample holder. Due to the unavailability/lack of response from the workshop technician and the short time before the system booking date, sandpaper was used to grind the sample's edges in an effort to reduce its diameter. To make sure the sample wasn't made too small for the sample holder it was grinded overnight until its diameter was about 17 mm which is close to that of the sample holder (15 mm). The rest was done on the experiment day when the holder was available and it was possible to constantly check whether or not the enamel sample and holder's diameters match.



Figure 55: Original sample (left) and sample during the grinding process (right). The sandpaper used for grinding is shown in the background.

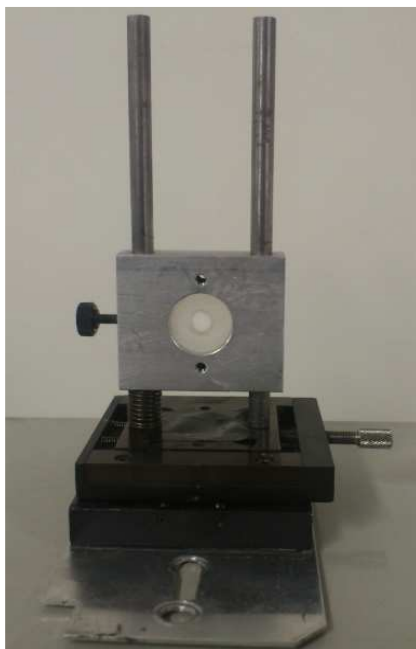


Figure 56 (a): Enamel sample after sandpaper grinding seen fitting perfectly into the quasi-optical circuit sample holder.

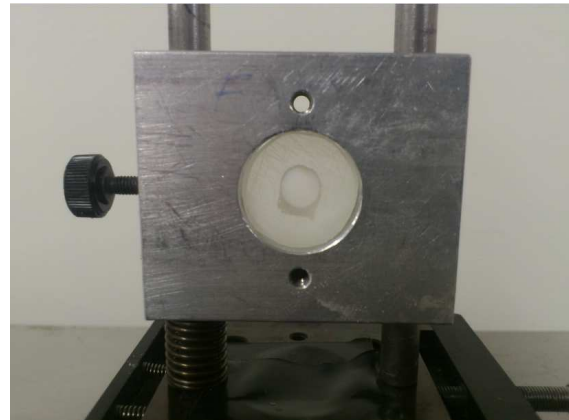


Figure 57 (b): Close-up of (a).

After replacing the sample-holder, the VNA was connected to a PC containing software to automatically capture measurement results at set intervals. In order to avoid displacing the sample as much as possible, the sample was left in the holder throughout, with acid applied with a cotton bud onto the middle enamel part every 3 minutes. The first measurement was taken without the addition of acid, with subsequent measurements taken in this manner:

1. After the first measurement was taken, the text file containing the saved results appeared in the specified folder.
2. As soon as the file appeared, the cotton bud was immersed in the acid and gently applied to the enamel.
3. The acid was left to act on the enamel for just under 3 minutes, after which any excess was removed using a dry cotton bud before the next measurement was taken.

The samples provided were rough on one side and smooth/polished on the other side. The middle enamel part is exposed on the smooth side and covered by the same resin that surrounds it on the other side. This means that acid can only be applied to the smooth side in order for it to have an effect on the enamel.

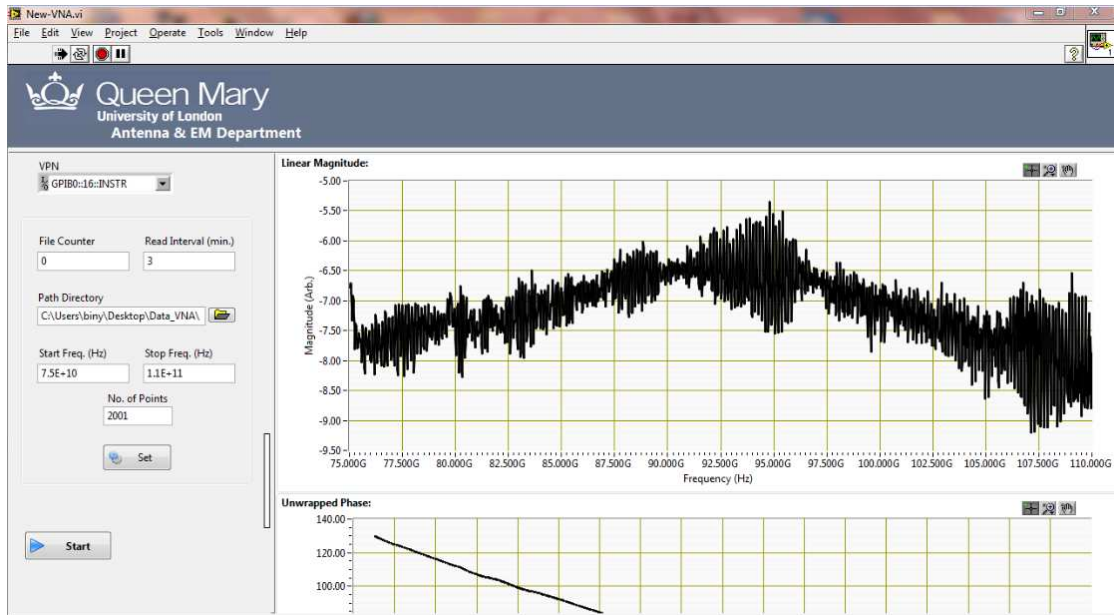


Figure 58: Screen-shot of LabView based automated measurement software used for this experiment to collect S_{21} data (between 75 GHz and 110 GHz) every 3 minutes for 1 hour.

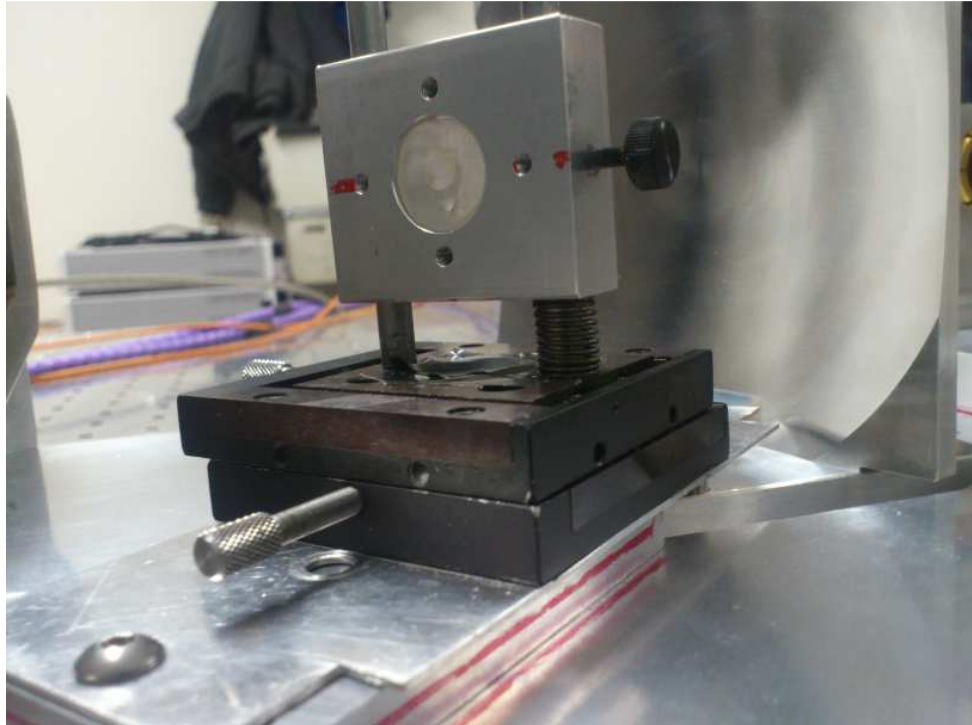


Figure 59: The enamel sample within the quasi-optical circuit, soon after the acid was applied. One of the mirrors used to reflect the beam is visible behind the sample holder.

Repeating this process every 3 minutes for about an hour resulted in 21 measurements, including one without the effects of the acid.

As with all of the samples tested in this project, the thickness of the samples was measured using a micrometre in order to account for it when plotting transmittance functions. The thickness of this sample was **3.828 mm**.



Figure 60: Micrometre used to measure the thicknesses of all samples at the end of the experiments (in order to not interfere with results by possibly altering the enamel's shape/compress it).

Before the measured S_{21} values were analysed, plotting the measured transmittance of all the 21 trials showed a lot of noise and thus the values had to be smoothed using an "rlowess" filter which smoothes the data by local regression using weighted linear least squares and a 1st degree polynomial model. Due to all results showing the same proportion of noise, they were all smoothed using the same program for consistency. The program I wrote, attached with the name "**rlowess.m**", smoothes the data using the multiple times before displaying the result. As all of the measurements in this experiment were smoothed using the same program, any variations in the data due to the effects of acid would still be visible after analysis.

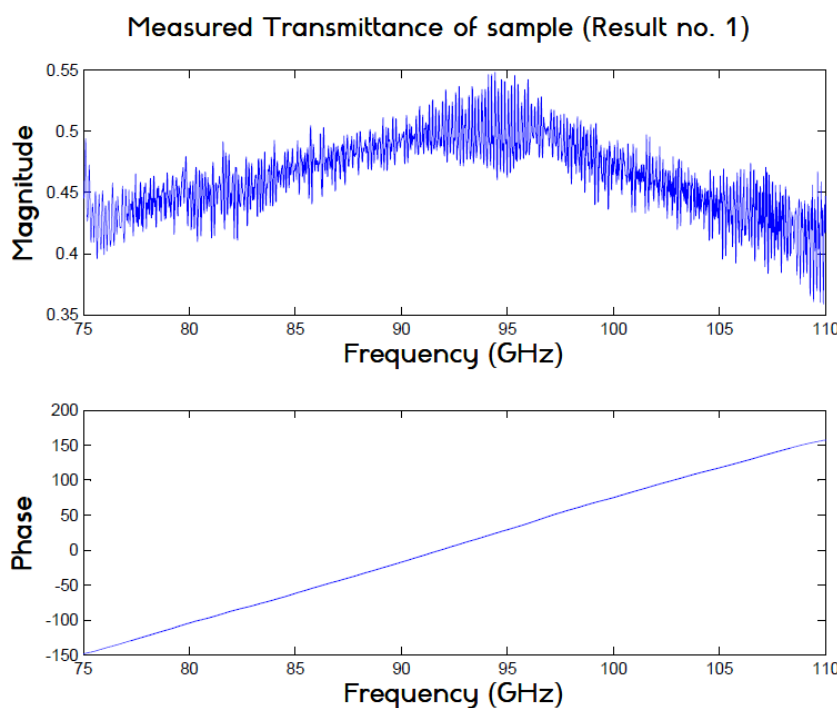


Figure 61: The first measured transmittance of the sample (without acid), showing a lot of noise in the magnitude.

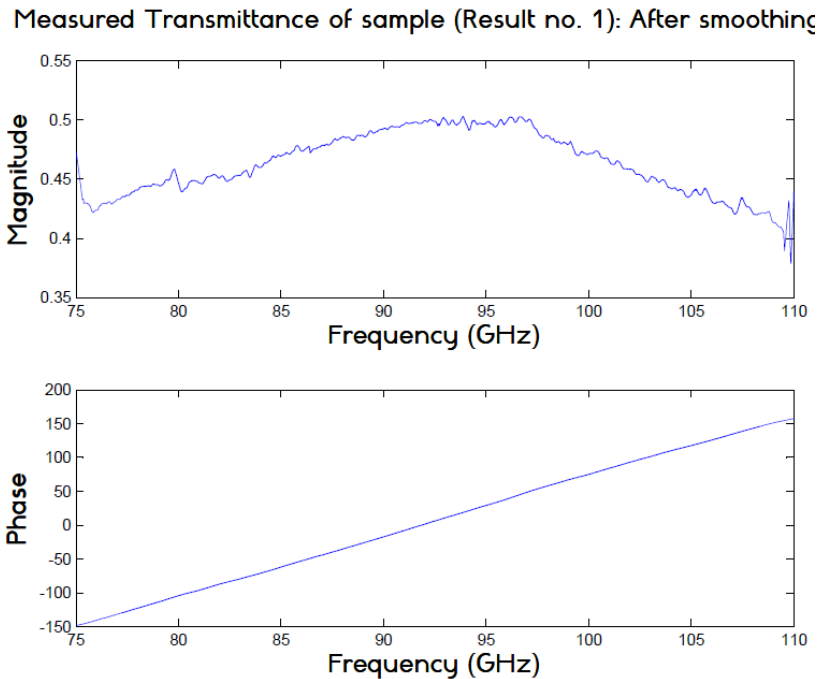


Figure 62: The first measured transmittance of the sample (shown in **Figure 61**), after smoothing.

For all the measurements, the smoothed data was inserted into the programs described previously to extract the refractive index. Smoothing the data makes the permittivity extraction process easier and more accurate. **Figure 63** below shows the result of the fitting process applied to the first measurement, which is that of the sound enamel sample, before the subsequent acid additions. **Figure 64** on the next page shows the dispersive refractive index of it across the frequency range, a result of the transmittance graphs fitting process.

Theoretical vs Experimental Transmittance of sample (Result no. 1)

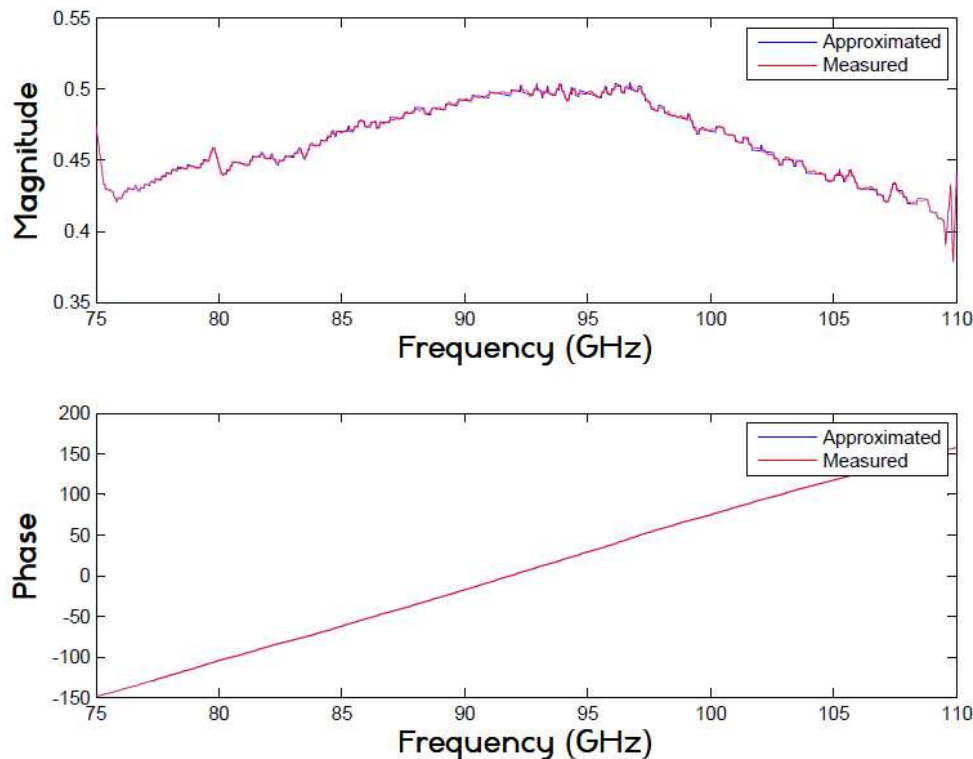


Figure 63: The measured and theoretical transmittance graphs (after the fitting process) of the enamel sample before the application of acid.

Complex Refractive Index of sample (Result no. 1)

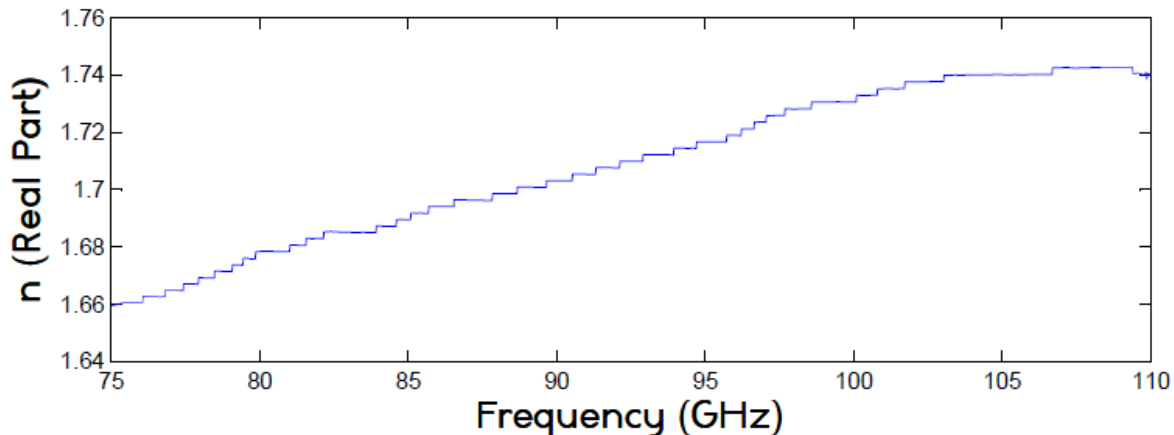


Figure 64: The refractive index (after the fitting process) of the enamel sample before the application of acid.

Repeating this process for all 21 measurements, the refractive index of the sample between 75 and 110 GHz was calculated at all 3 minute intervals for the whole hour. Due to the results being too close together, Figure 65 below shows the refractive index measured at 6 minute intervals only.

Complex RI (Real part) of sample

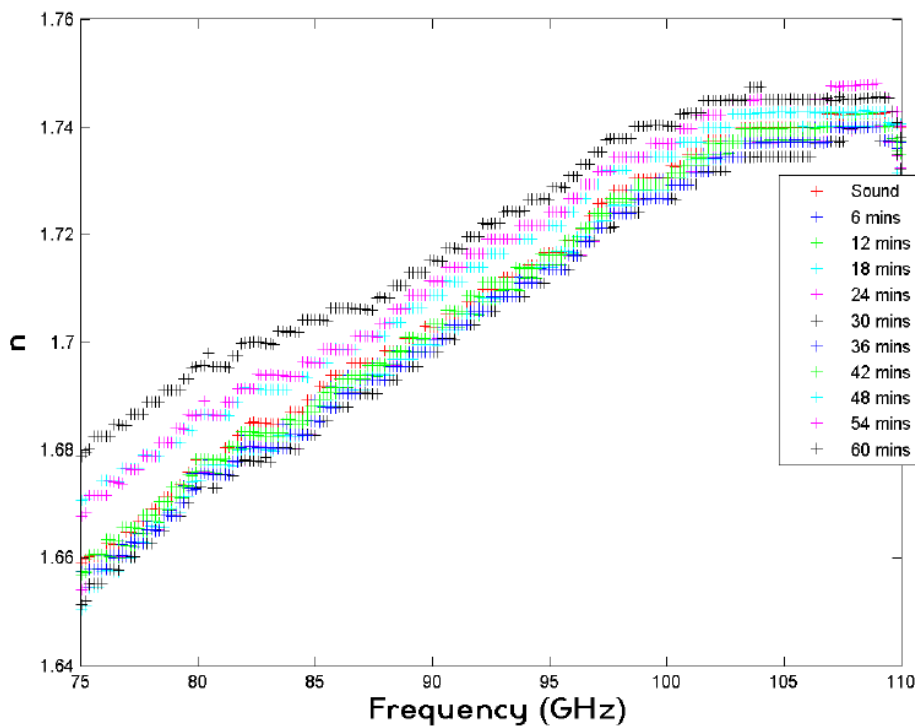


Figure 65: The complex refractive index of the enamel sample measured at 6 minute intervals (applying acid each time) throughout the 1 hour.

Due to the presence of only one peak in the measured transmittance graphs for all 21 measurements of the sample, it was possible to extract the refractive index of the sample at the transmittance peak for every measurement. Comparing the refractive index at this point for all measurements gives a better representation of the variation in refractive index at every interval within the 1 hour time period.

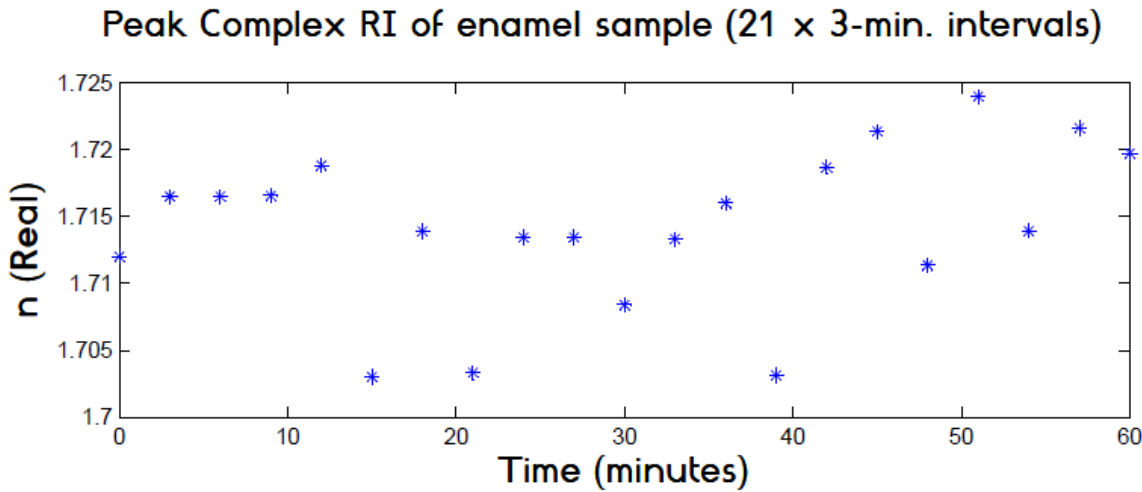


Figure 66: The complex refractive index (extracted at the frequency at which the peak measured transmittance is present) of the enamel sample as it varies with time. Time = 0 corresponds to the sound (healthy) sample, Time = 3 corresponds to the refractive index after acid was applied for 3 minutes (and wiped off), Time = 6: after acid was applied for another 3 minutes after the previous measurement etc.

Due to the close proximity of all the refractive index graphs, only 3 were plotted in **Figure 67** below and compared in order to identify whether the acid has had its effects on the sample or not.

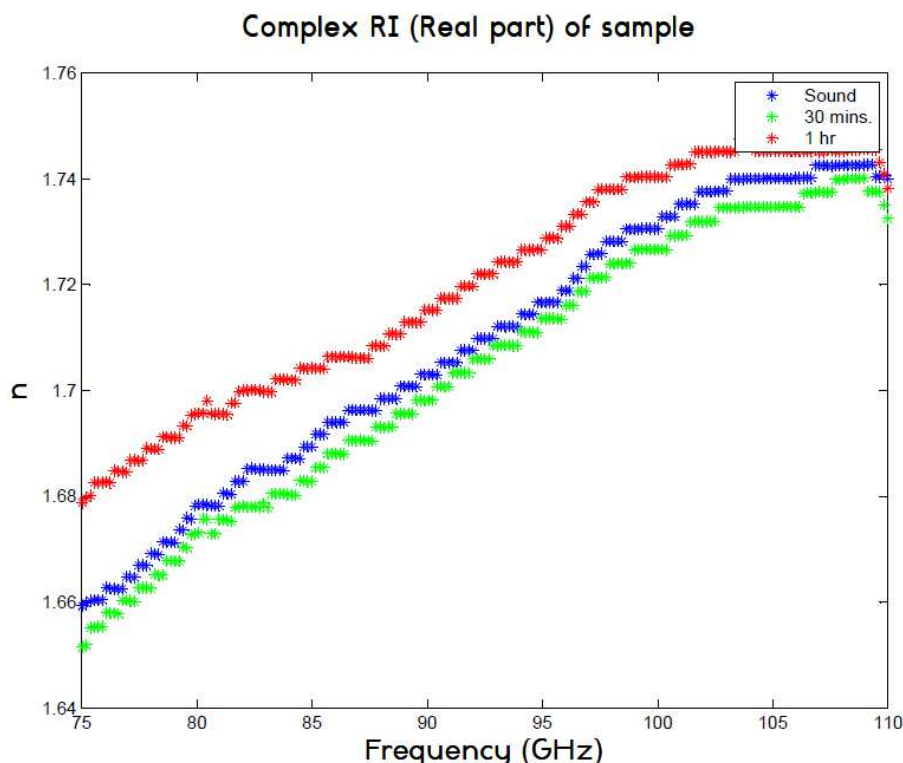


Figure 67: The complex refractive index of the sound enamel sample (blue), after 30 mins. of applying acid (green) and at the end of the experiment (red).

4) Three enamel samples with de-mineralisation (5 hour period):

Due to the possibility that the intervals between measurements in the previous experiment were too short for the acid to have a noticeable effect on the results, the experiment was repeated for a longer duration with 3 other enamel samples which were likewise reduced in diameter. Similarly, while grinding with sandpaper, the best effort was done to ensure that the enamel part lies completely in the middle of the surrounding resin.

As well as increasing the experiment duration, the method by which the acid was applied was changed in this experiment. In the previous experiment, the sample was left in its vertical position within the holder and a cotton bud was used to apply the acid. For this experiment, the samples were removed from the holder and laid horizontally with acid added using a dropper on their smooth side (where the enamel is exposed). This also helped to quantify the acid added to the samples as one of the dropper's features is to limit the amount of acid added to the sample. The dropper was better than a syringe which could induce a parallax error when reading off the scale.



Figure 68: Dropper used to apply acid onto enamel samples. The scale on the lower picture reads 1 ml.

Since this means that the samples had to be constantly removed and replaced within the holder, markings on the edges were used to monitor their position within the holder. This was used as a method of control just in case their rotation within the sample holder may affect the results and by aligning the markings with the holes on the sides of the holder it was possible to make sure that the same side is always facing north for all measurements. The markings were also used to number the samples to account for their differing thicknesses, amount of acid added and the duration that the acid was left before it was wiped off on the results produced.

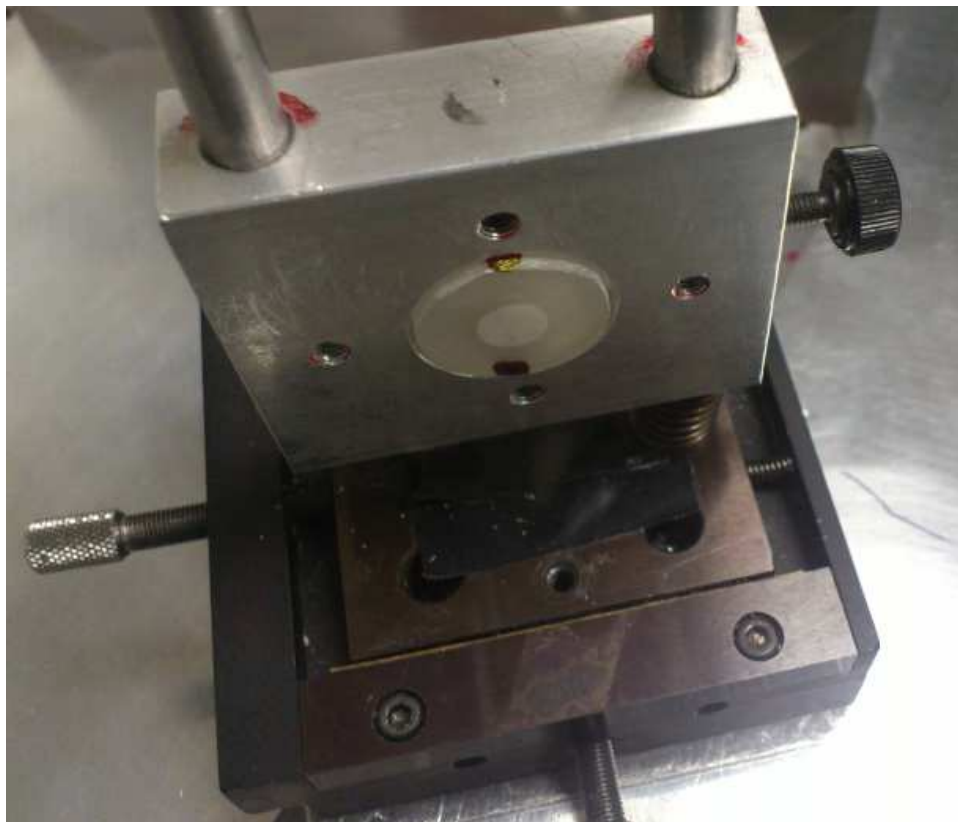


Figure 69: Aligning the markings with the holes on the sample holder in an effort to keep the position constant throughout the procedure.

As well as controlling the position of the samples, the side facing the incident beam was also controlled. Dental erosion is a surface effect and due to the hard nature of the enamel it is unlikely that the acid placed on the top layer (smooth side with exposed enamel) has a great effect on the rest of the enamel underneath. In another effort to keep measurements controlled, the side on which the acid possibly affected was placed facing the incident beam at all times for all three samples. Measuring S_{21} means that the incident signal comes from port 1 of the VNA and passes through the sample to the receiving end at port 2. If the surface of the enamel changed because of de-mineralisation effects, it may as well have a direct effect on the amount of the beam that is reflected back to port 1. Thus, it would be inaccurate to measure with the beam incident on the rough side (where enamel is covered) once and on the polished side another time.



Figure 70: Two of the samples used for this experiment. The visible protuberance over the middle enamel part (on the smooth side of the sample) is the acid droplets. Enamel is a hard substance and the acid doesn't dissolve through it. This is why it has to be wiped off before a measurement is taken.

At first, all three samples were measured without the effects of acid. After that, the procedure outlined below was followed throughout the 5 hour period:

Sample 1	Sample 2	Sample 3
Applying 1 ml of acid every 30 minutes before wiping it off and taking a measurement.	Applying 2 ml of acid every 60 minutes before wiping it off and taking a measurement.	Applying 2 ml of acid every 60 minutes before wiping it off and taking a measurement.

This approach was chosen to see whether the amount of acid added to the enamel or the time it is left on the enamel produced any differences in refractive index results.

Similar to the previous experiment's results, S_{21} data (hence measured transmittance) across the frequency range contained a lot of noise and smoothing had to be done in order to make sense of it. There was, however, one step that had to be done before that. The person who supervised this experiment was different than the person who supervised the previous 3 experiments and the frequency scaling which he set on the VNA was in steps of about 5.4 MHz compared to the scaling in the previous experiments which was around 18 MHz. This new frequency scaling meant that the column vectors used to hold the frequencies and corresponding S_{21} magnitude and phase data consisted of 6401 rows compared to the previous 2001 rows. The programs which I wrote to extract the refractive index involve a lot of processing and caused Matlab to freeze at times or display the error below:

Out of memory. Type HELP MEMORY for your options.

As a result of this I wrote another program to virtually reduce the scaling on the VNA by only keeping the S_{21} data at certain intervals (every 3 rows). It is attached under the name "**minimiser.m**" and it reduces the VNA data from 6401 rows to 2134 rows.

To see whether this step has an effect on the quality of the results, S_{21} magnitude and phase data were plotted for the same measurement: one using the original results and one with the reduced results.

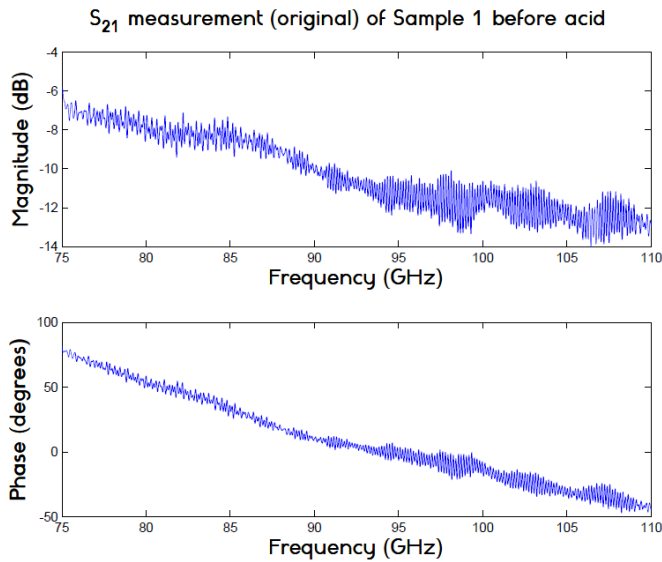


Figure 71: Original S_{21} magnitude (decibels) and phase (degrees) graphs of Sample 1 at the beginning of the experiment (before acid).

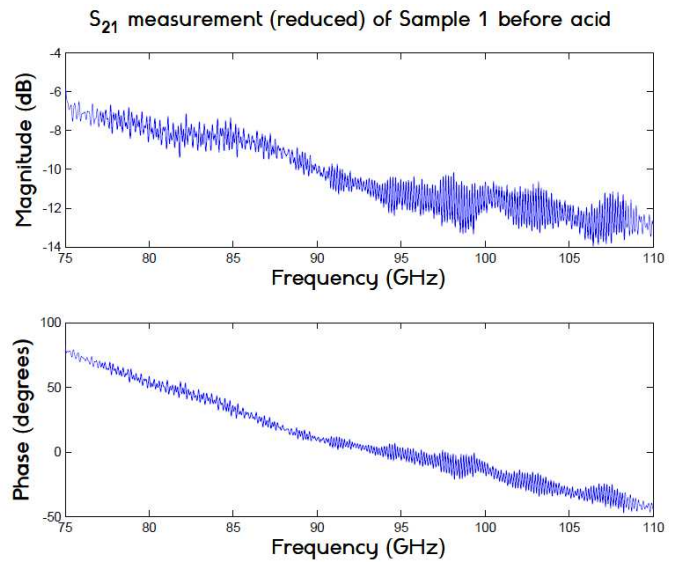


Figure 72: Reduced S_{21} magnitude (decibels) and phase (degrees) graphs of Sample 1 at the beginning of the experiment (before acid).

Since it is evident that this reduction in the frequency scale from around 5.4 MHz to around 18 MHz (increased step size) has no effect whatsoever on the measurement results, all 18 '.mat' files which were imported from the VNA's Excel spread sheet outputs were minimised in the same manner.

The next step was to smooth the data as it was exceptionally noisy, just as in the previous experiment. All results were smoothed using the same program, i.e. the same number of times for consistency.

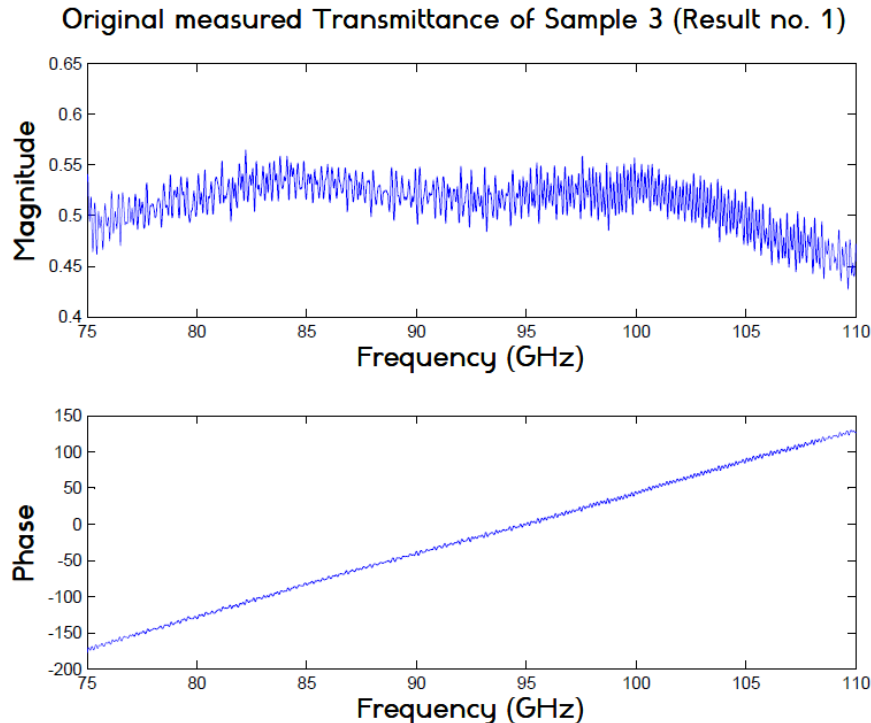


Figure 73: An example of the measured transmittance (calculated from the "minimised" S_{21} data) of Sample 3 before the addition of acid.

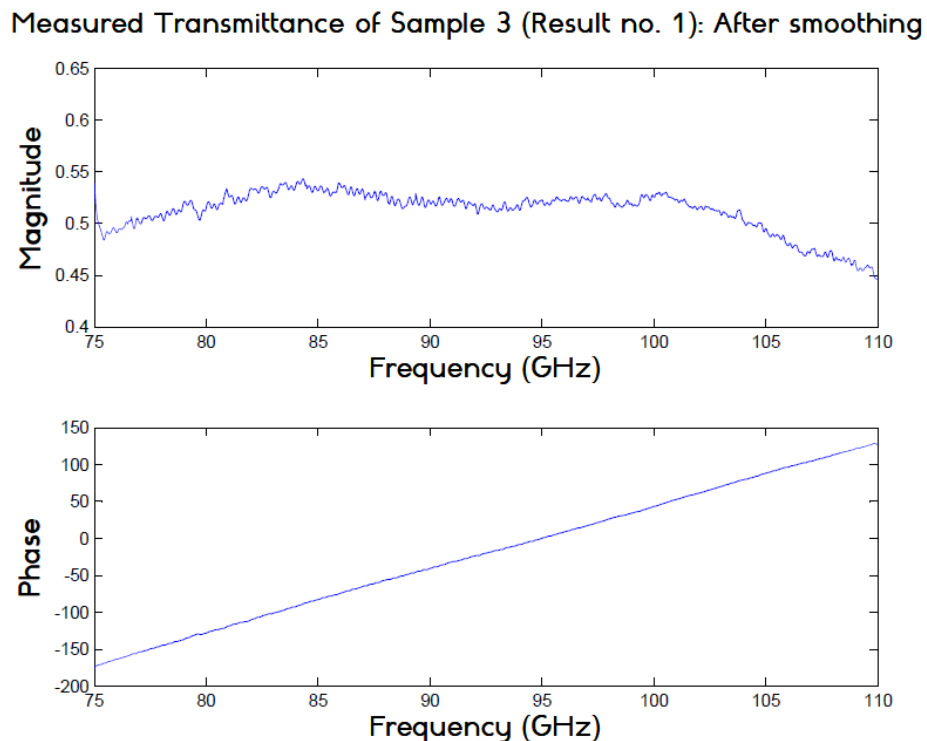


Figure 74: The same transmittance graph in Figure 73, after the smoothing process.

The next stage, after smoothing out all the measured transmittance results, was to insert them into the other programs in order to extract the refractive index of all the samples at each time interval within the 5 hour period. Just like in the previous experiment, the 'smooth' measured transmittance magnitude and phase graphs were imported into the program, recombined to form the complex measured transmittance and finally used within the least squares algorithm to calculate the dispersive complex refractive index. Sample thicknesses as measured by the micrometre were **4.612**, **4.506** and **3.951 mm** for Samples 1, 2 and 3 respectively.

Taking Sample 3's measurement results before the addition of acid for example, the graphs in Figure 75 on the next page show the measured transmittance, obtained from S_{21} data, and the theoretical transmittance, calculated using the dispersive complex permittivity.

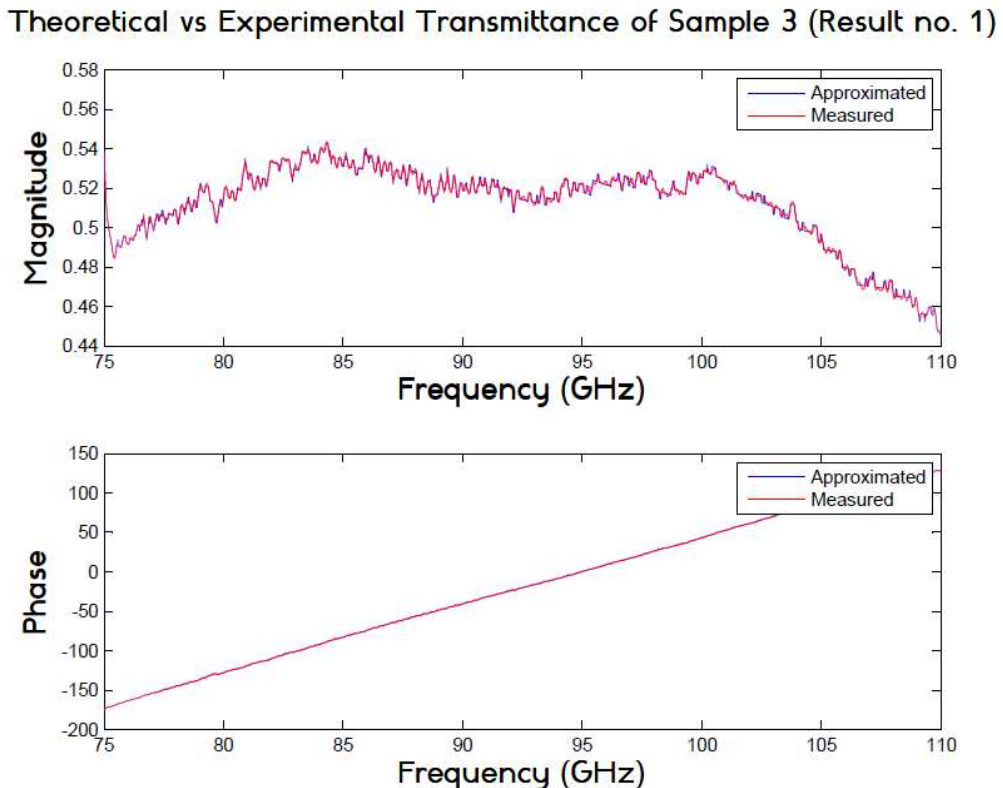


Figure 75: Measured and theoretical transmittance of Sample 3 before acid. The theoretical transmittance (blue graph) was calculated using the permittivity range which was manually set.

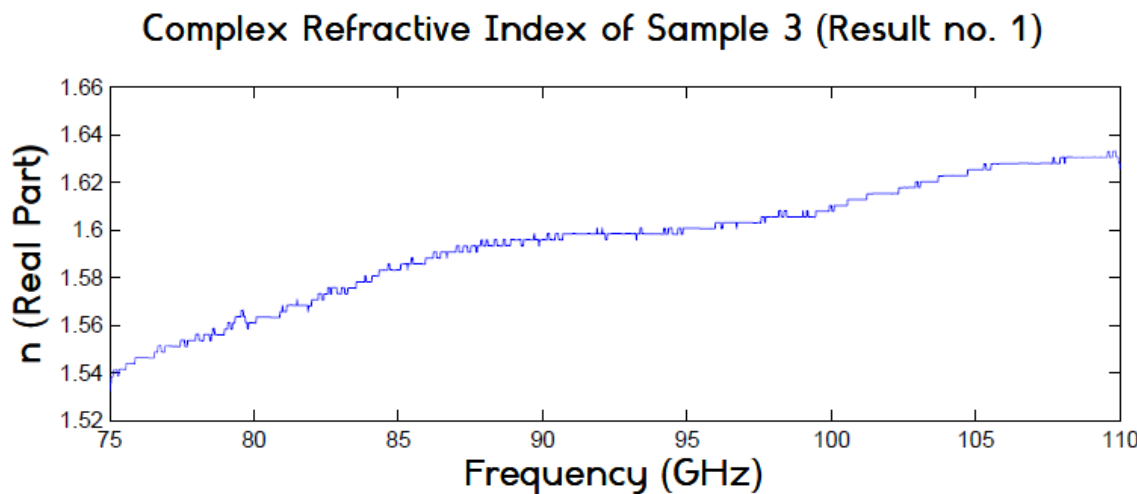


Figure 76: The complex refractive index of Sample 3 (before acid) at every frequency within the 75 – 110 GHz frequency range.

There was a small problem with the S_{21} data of some of the results for samples 1 and 2. For sample 2 for example, the measured transmittance before smoothing showed a lot of oscillations somewhere between 100 and 105 GHz. The data was smoothed in an effort to eliminate the noise in this region which is clearly an experimental error.

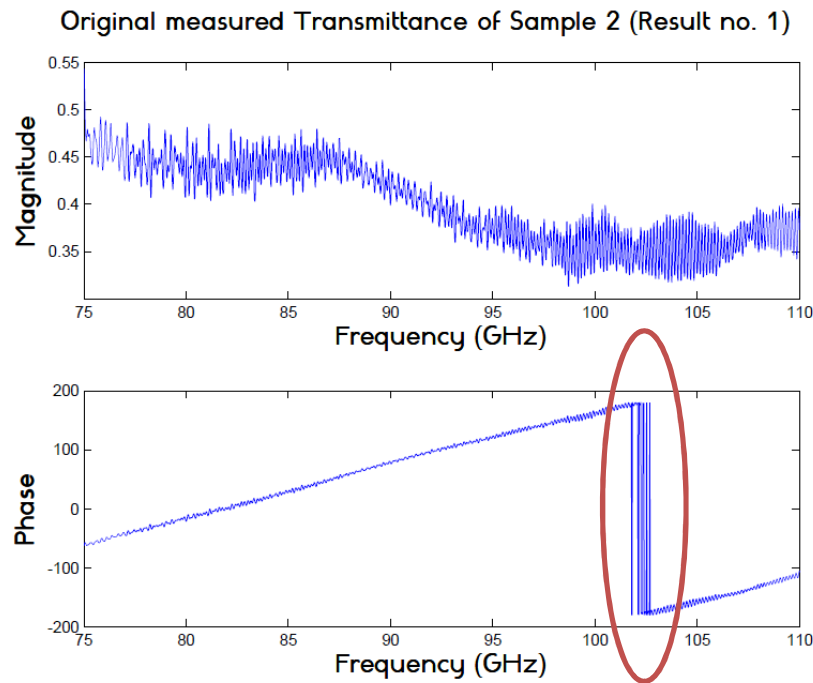


Figure 77: Measured transmittance of Sample 2 (before the addition of acid). The oscillations between 100 and 105 GHz are not normal and haven't been seen in any of the measurement results before.

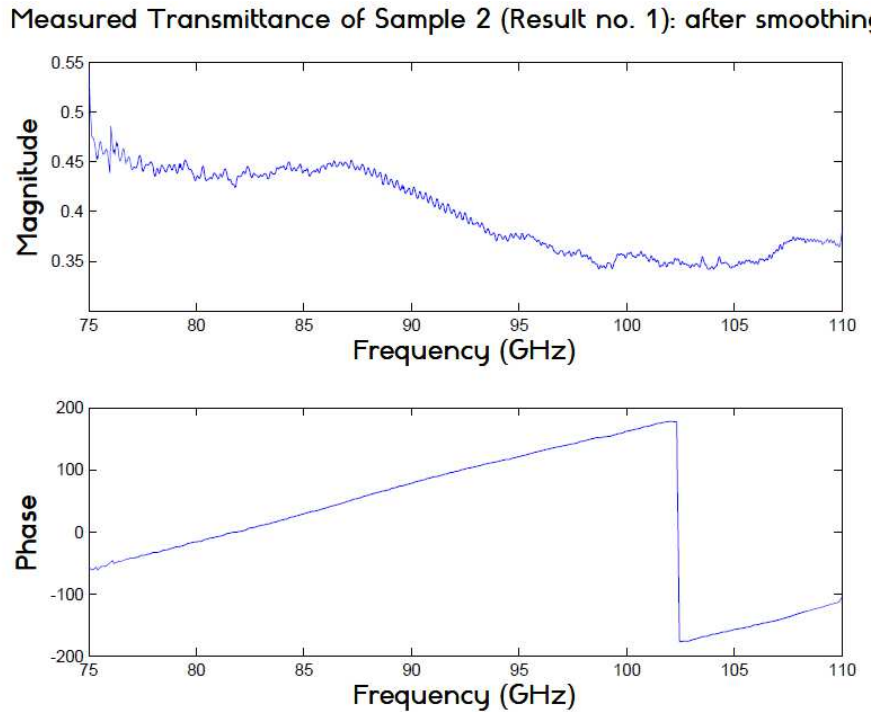


Figure 78: Measured transmittance of Sample 2 (before the addition of acid) after it was smoothed. Transmittance phase data had always shown a shape similar to the one here (after smoothing) and there have never been any oscillations like in **Figure 77** above.

These oscillations, although corrected slightly as a result of the smoothing, still affected the fitting process. When setting the limits for the permittivity, I ignored the fact that the permittivity at the point of the oscillations is greater than the set limits. I chose to focus on the permittivity of the samples at all the other frequencies instead of compromising the majority of the results just because of this.

Theoretical vs Experimental Transmittance of Sample 2 (Result no. 1)

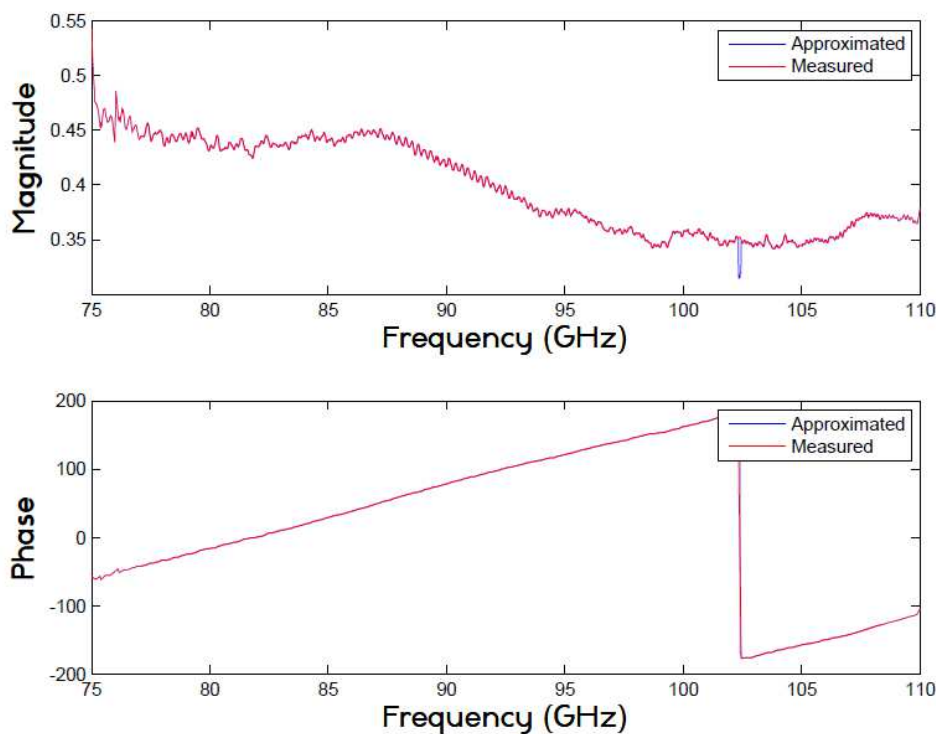


Figure 79: Theoretical and measured transmittance of Sample 2 (before the addition of acid). Due to the permittivity limits used being ignored for the area which showed oscillations, the theoretical graph doesn't fit the measured one between 100 and 105 GHz.

Complex Relative Permittivity of Sample 2 (Result no. 1)

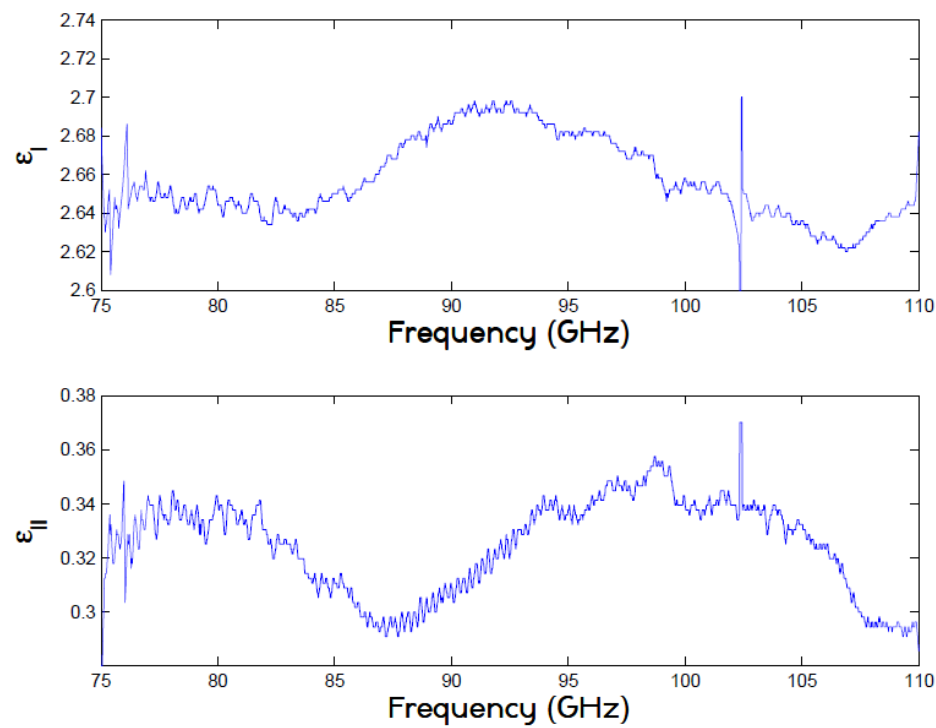
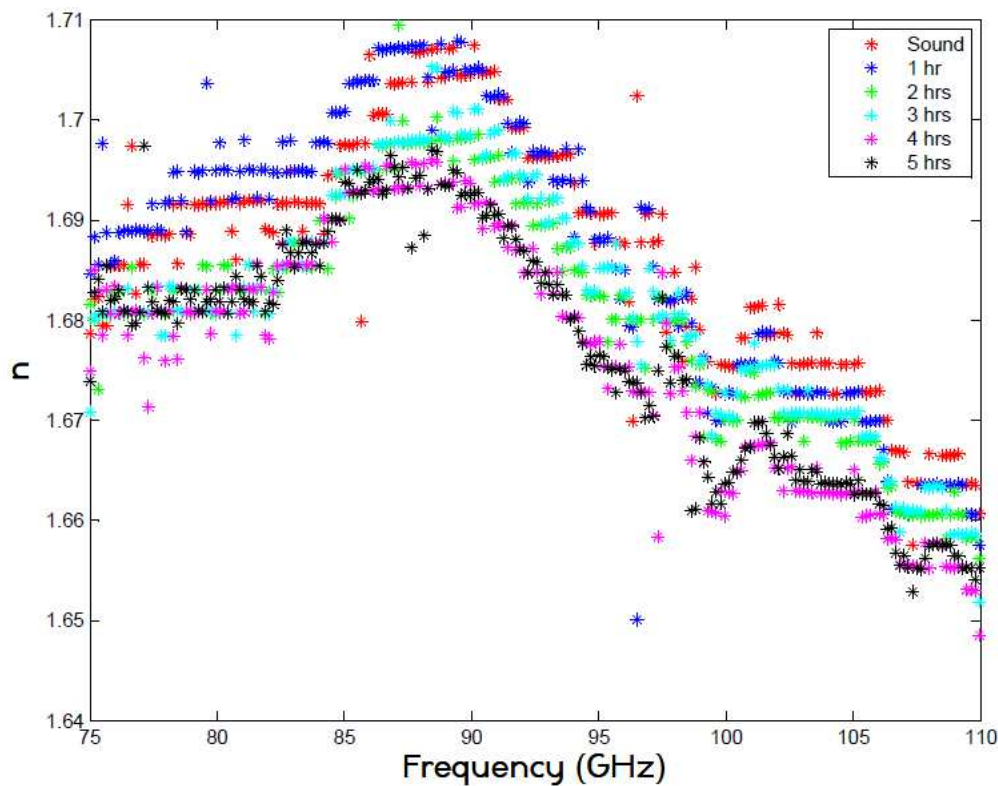


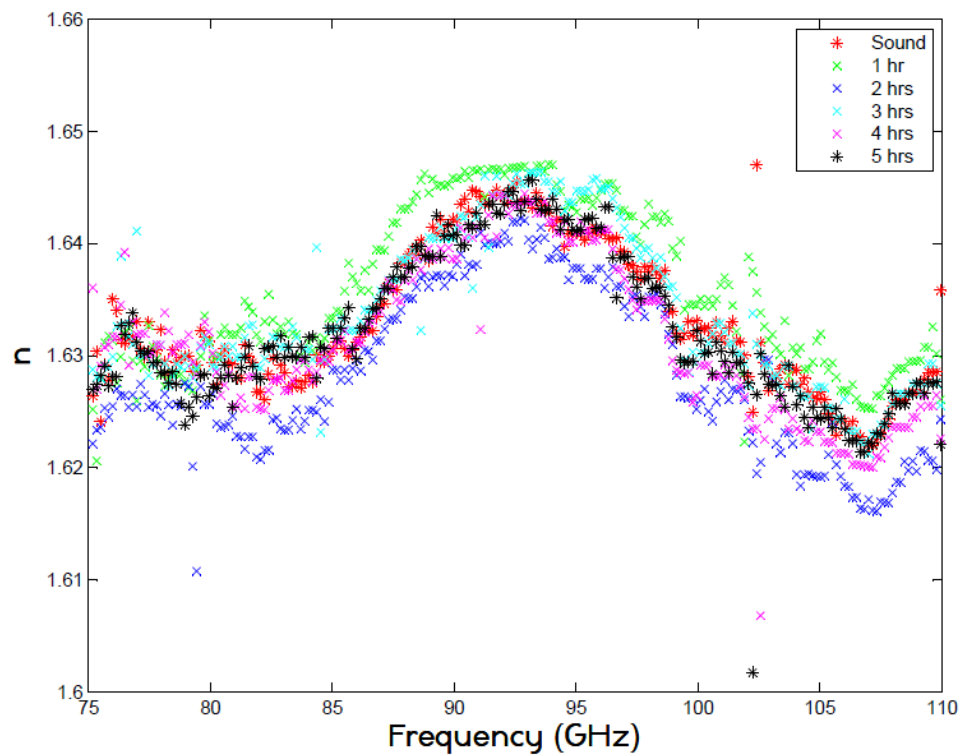
Figure 80: The complex relative permittivity of Sample 2 (before acid). The great increase in the values between 100 and 105 GHz is seen.

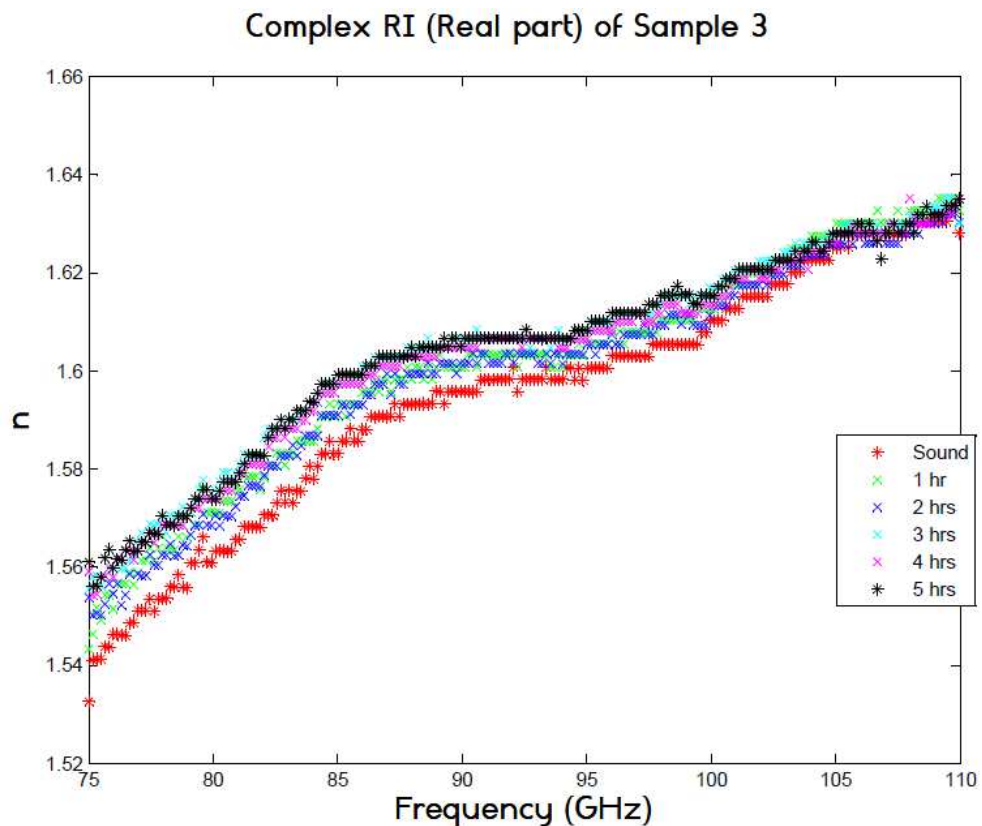
After analysing all of the S_{21} results for the three samples, it was possible to obtain refractive index values of the samples at various times. All the final results are shown on the next pages.

Complex RI (Real part) of Sample 1



Complex RI (Real part) of Sample 2





Discussion/Analysis of Results

In this section the results shown in the previous section will be discussed and analysed in order to arrive to a relevant conclusion as to whether or not the aims of this project have been met. In most of the results displayed in the previous section, the imaginary part of the refractive index was shown as well as the real part. In this section only the real part of the complex RI is compared due to the relative irrelevance of the imaginary part to the aims of this project. The imaginary part κ corresponds to the amount of loss experienced by light/any electromagnetic radiation as it travels through the material. It depends on the dielectric loss of the sample which in turn depends on ϵ_{11} . Most of the samples showed low values for the imaginary part of the complex relative permittivity which classifies the samples in the “low-loss” category. The real part of the complex RI, n , is what this project is concerned about which is the ratio of a wave’s velocity in the material to that in free space.

It is important before jumping to any conclusions to first prove that the processing of the S_{21} results generated by the VNA and the calculation of the refractive index of the samples from the fitting procedure using the codes I wrote is correct. If the codes work correctly then analysis and comparison of the refractive index results can then safely take place.

The first step taken to ensure that the codes I wrote work correctly was to test them with data for a pre-characterised material. I was sent the S-parameters of a low loss, high permittivity ceramic by the research assistant who guided the experiments to try on my codes. The sample was thin and had a high permittivity value and so it was possible to extract the refractive index at the transmittance maxima and minima due to the presence of consecutive peaks and troughs in the transmittance graph within the frequency range.

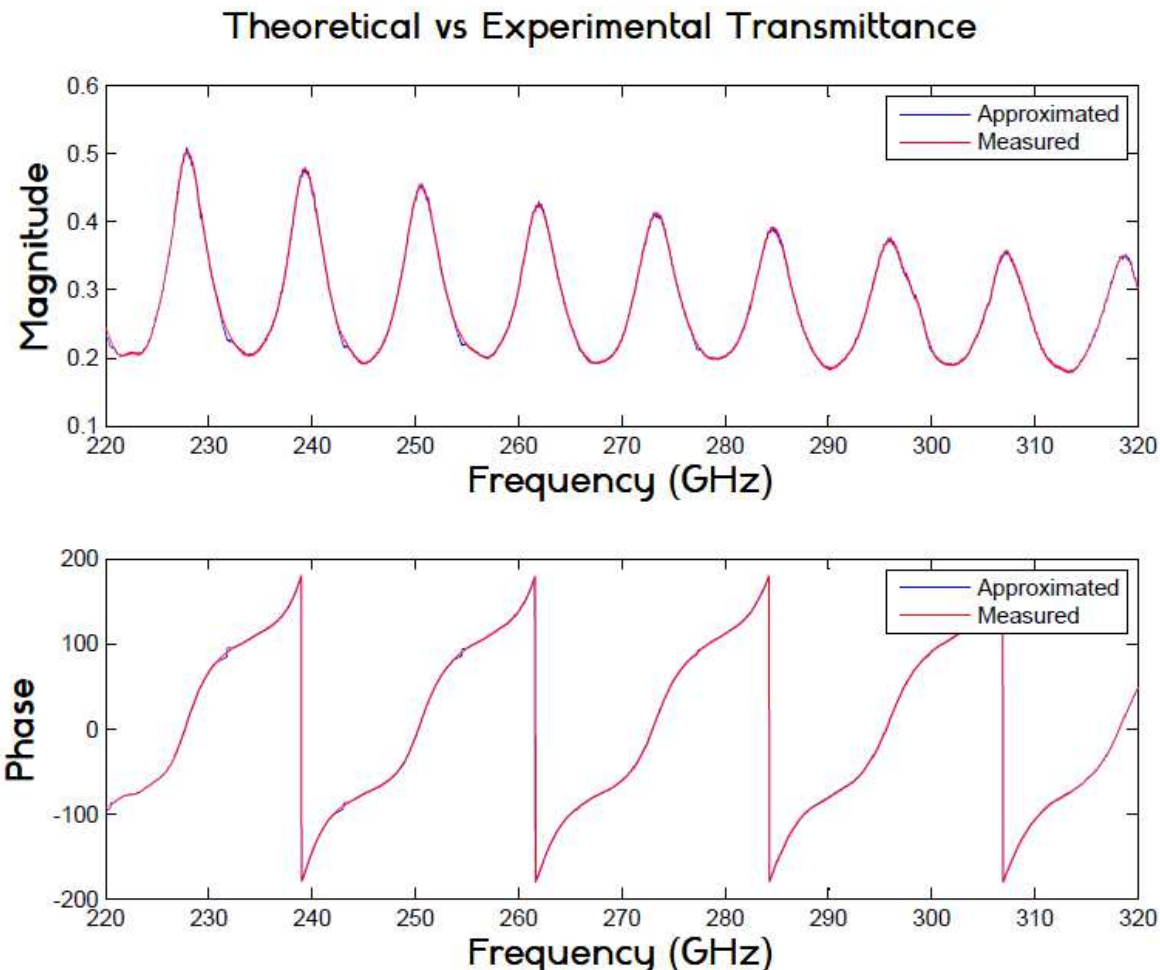


Figure 81: The measured transmittance graph of the sample (obtained from the S_{21} results I was sent) and the theoretical transmittance graph (after the fitting procedure). As for all of the results in this project, the fitting is almost perfect.

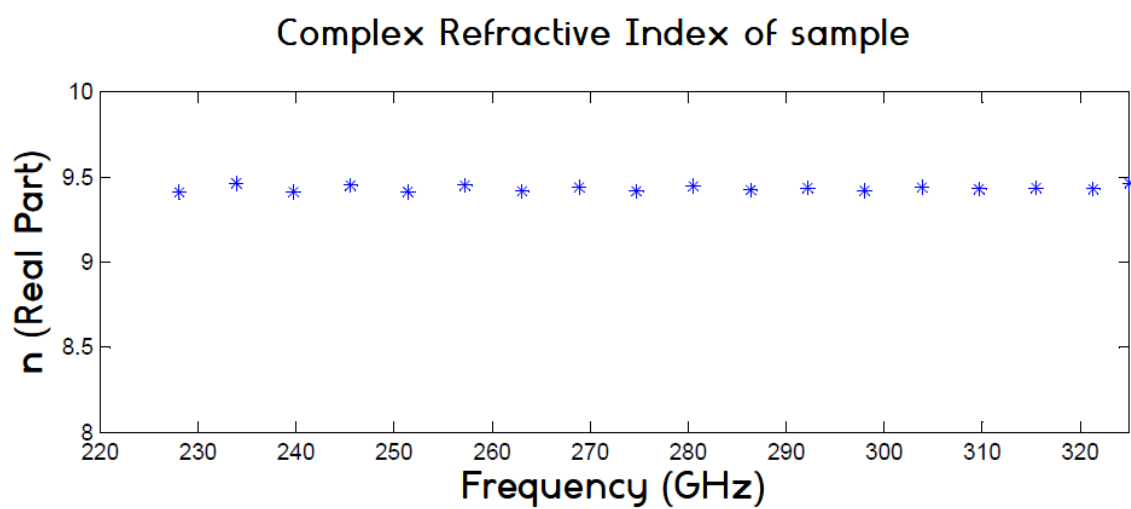


Figure 82: The complex refractive index of the sample extracted at the peaks and troughs of the transmittance graph.

After showing the refractive index plots in **Figure 82** above to the research assistant, he confirmed to me that the results are correct which justifies my manual fitting method which doesn't use any Matlab tools. He also confirmed that I can use refractive index values at all points in the 75 - 110 GHz frequency range to compare between results. This is because there aren't any peaks/troughs in most of the results and using the program "**peak_trough.m**" would therefore require a larger frequency range, possibly the whole 75 - 325 GHz range in order to get a complete transmittance graph with multiple peak amplitudes in it. To make comparisons clear, refractive index values for experiments 3 and 4 were plotted at selected intervals due to the difficulty of comparing multiple graphs for each sample. This was because the graphs overlapped each other and it became hard to tell which one is which. The graphs were plotted the way they are shown in the previous section after testing multiple colours and markers until the ones that made comparisons to be made easily were chosen.

The second step was to compare the refractive index of the scattering phantom cross section to that present in a National Physical Laboratory's report written by Peter H. Tomlins, Robert A. Ferguson, Christian Hart and Peter D. Wooliams titled "*Point Spread Function Phantoms for Optical Coherence Tomography*" [51] from which the figure below was taken.

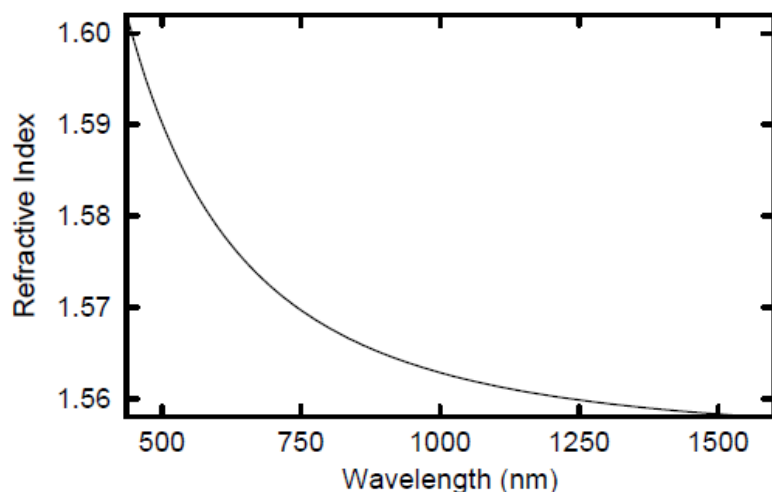


Figure 83 Refractive index of cured DBF resin measured over the wavelength range 435.8 nm to 1600 nm [51].

The refractive index shown above is of the material that makes up the phantom at optical and infra-red wavelengths. Unfortunately, there isn't any data available as to the refractive index across the millimetre wavelengths. This is because the phantoms are used mostly at infra-red wavelengths (in OCT) and are characterised for that purpose only. Thus, it wasn't possible to compare the refractive index measured in the experiment (which was around 1.7 across the 220 -320 GHz range) to any standard data.

It was my plan to get hold of some material which is well characterised with viewable online/published dielectric property measurements in order to measure using the transmissometer. If the S_{21}/S_{12} results obtained from the measurement result in permittivity/refractive index results comparable to published results after being processed using the transmittance fitting code then that would be enough proof. This was not possible due to the unavailability of the transmissometer at the time I finished the code.

Experiment 2 (3 sound enamel samples):

In this experiment 3 sound enamel samples were measured “just for fun”. The plan was to use these samples later on for de-mineralisation later on but they were needed for another project and so new samples were brought in for the other 2 experiments.

The refractive index of these samples varied from around 1.7 to 1.74 as shown in **Figure 53**. This result could be used to get an idea about the approximate RI value at the W band. As I was not present for this experiment and the samples weren’t grinded with sandpaper, I assume that care was taken to keep the middle part of the samples, which contained all the enamel, in the middle of the sample holder as much as possible.

Experiment 3 (1 de-mineralised enamel sample, 1 hour duration):

In this experiment, the sample was left in its vertical position on the sample holder and acid was applied to the exposed enamel by the use of a heavily soaked cotton bud. The refractive index values showed some changes as time progressed but this couldn’t have been a result of de-mineralisation. If de-mineralisation would have been the case then a trend would have been visible as time progressed. Even after the results were plotted only at 6 minute intervals the refractive index graphs were overlapping as the refractive index varied from 1.65 to 1.75.

Since a transmittance peak was present in all 21 results using this sample, the refractive index at this peak (for each measurement) was extracted from the refractive index graph for all the frequencies. This is because ideally, refractive index/permittivity would be extracted at the maxima and minima of the transmittance functions (more on this in error analysis). The peak refractive index varied between 1.7 and 1.725 as is seen in **Figure 66** and there wasn’t any particular decrease in the refractive index with time, which represented the total amount of time that the acid had been acting on the enamel without being wiped off. This result led to the speculation that either the 1 hour wasn’t enough to bring about a change in the refractive index or the method of applying the acid wasn’t really effective, especially as the sample was in the vertical position the whole time. Experiment 4 was the last chance to do a measurement and so the whole 5 hour period was utilised to investigate whether time was an issue.

Experiment 4 (3 de-mineralised enamel samples, 5 hours duration):

In the last experiment, 3 enamel samples were each tested across a 5 hour period. Sample 1 was measured every half an hour (over which the acid was acting on it) but in order to get a clearer view of the refractive index variation, the results for this sample were plotted only at 1 hour intervals. This is justified due to the fact that if the change in refractive index was due to the acid then it would be possible to see it by comparing the hourly measurements instead of the 30 min. ones.

The refractive index varied between around 1.65 and 1.71 and did show a slight decrease after the 5 hour period. Whether this decrease can be linked to the effects of acid can only be validated after looking at the results of samples 2 and 3.

Sample 2, on which 2 ml of acid was left to act on for 1 hour intervals (between measurements) showed a total variation in refractive index between about 1.62 and 1.65. There isn’t any visible trend in the refractive index and all 6 graphs are intertwined with many points overlapping each

other. Just as the sample in experiment 3, there was no visible effect of the acid on the enamel's refractive index throughout the 5 hour period.

Sample 3 was treated with 1 ml of acid every 1 hour, which means that it can be compared to Sample 1's measurement results at the 1 hour intervals. The initial plan was to make it different than Sample 1 by increasing the time duration in which the acid is left on the enamel by half an hour. Since Sample 1's results were plotted at hourly intervals and Sample 2's results didn't show the slight gradual decrease in RI which was observed for Sample 1 even though 2 ml of acid were added to it, Sample 3's new purpose was just to confirm that changes in the refractive index can't be detected. The refractive index of this sample varied between 1.54 and 1.64. Strangely enough, the refractive index shows a very slight increase as time progressed. This prompted me to think that maybe the results were plotted the other way round somehow. Doing the tedious fitting and processing again, I got the same results as before which meant that the changes in refractive index can't possibly be due linked to enamel de-mineralisation.

The results of this final experiment show that despite changing the procedure in which acid was added to the exposed side of the enamel samples and increasing the time duration, **the changes in the refractive index for all of the measurements can't be attributed to the de-mineralising effects of the acid on the enamel**. My opinions on why this is so are presented below. Some of the factors mentioned are related to why the transmissometer couldn't pick up changes in mineral content while others are just factors that may be an issue in the future and getting a hold on them might result in a better chance of result repeatability.

ERROR ANALYSIS

There are many possible reasons as to why the experimental results haven't shown a decreasing refractive index (magnitude) as a direct result of the application of acid onto the enamel samples. I strongly believe that the reasons which are listed below are linked to the obtained results and that if in the future they are investigated then there is a high chance of the transmissometer being able to detect changes in the mineral content.

1) Enamel sample preparation:

The samples provided contained enamel only in the centre with the rest being a resin. Even after grinding them with sandpaper, the samples were still mostly resin. This means that the beam passing through doesn't pass entirely through the enamel, it also passes through the surrounding resin. Assuming the resin (and enamel) from which the samples are made is the same, which is probably the case, there is still the issue of sample thickness and parallelism of the edges.

The samples studied had varying thicknesses, which is an important factor in transmission spectroscopy. This shouldn't be a problem if each sample is studied separately as was done in this project but it is an issue if multiple samples were tested to ensure repeatability (if future results showed any trends).

Just for the sake of comparison, the refractive index of all of the enamel samples in the three experiments is shown in **Figure 84** on the next page.

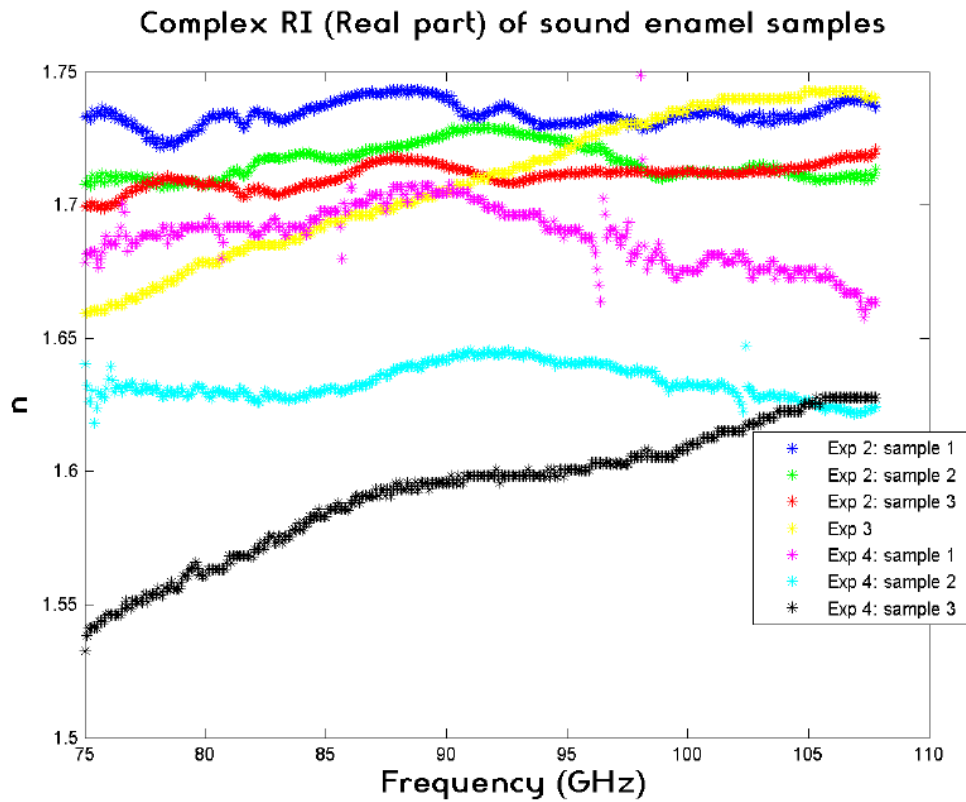


Figure 84: The refractive index of all of the sound (healthy) enamel samples used for the experiments in this project.

It can be seen that the refractive index of the samples varies even before the addition of acid which hints that comparisons between results of different samples in the future can only be done with samples that are exactly identical and have perfectly parallel sides.

The profilometer scan of the scattering phantom discussed in the previous section showed that it didn't have a perfectly flat shape. Again, assuming that future work in this subject carries on and the issues discussed in this section are addressed leading the detection of mineral content, if multiple samples are to be compared against each other then parallelism of the edges might be important.

Ensuring that both surfaces of a sample are perfectly flat and parallel can be checked by using a profilometer as seen in the previous section. Achieving parallelism of the edges can be done using lapping machines. At the **School of Engineering and Materials Sciences** at QMUL, single sided lapping machines are available that can ensure flatness of only one of the sample sides. Double-sided lapping machines by which parallelism of the edges can be achieved can be done by companies such as **PETER WOLTERS** [90]. My original plans were to lap up the scattering phantom cross section and repeat the refractive index measurement to see if there were any changes but due to the unavailability of the transmissometer this couldn't be done. A quote I got for double side lapping the phantom is about £100.

Looking again at the graphs in **Figure 84**, Sample 3 (in the last experiment) has the lowest refractive index of all. For this particular sample I accidentally made it about a millimetre in diameter smaller than the sample holder during the sandpaper grinding process. To make sure that it doesn't fall out/tilt when placed in the holder I wrapped a thin layer of tape around it to make up for the empty

space. The low refractive index resulting from this could be possibly due the absence of resin around the edges of the sample which leads to another possible issue in error analysis.

This is the issue of perfectly fitting the samples within the holder. Grinding them with sandpaper was the only solution but using high precision cutting tools to give them all the same diameter and to ensure that the enamel containing part lies perfectly in the middle of the beam would have been better.

All of the above ideas may not have much to do with why the refractive index changes due to demineralisation weren't visible which brings me to the most important part which is the thickness of the enamel samples. Enamel is a hard substance, and just as is shown in the photo from **Figure 70**, the acid stays on the surface and doesn't pass to the bottom layers. This means that the acid can only act on the top layer of the enamel and thus any de-mineralisation that will happen will only be to the surface. Studying dental erosion with these samples using OCT is perfectly fine since OCT is capable of producing 3D images of multiple layers of the sample hence making it possible to view changes on the surface (simulating actual erosion).

At SMD, where these studies take place, the samples are placed in a glass container filled with a thin layer of acid in such a way that the exposed enamel side of the samples lies directly on the acid. The entire container is then placed in the OCT machine where it is left for hours as the de-mineralisation takes place, enabling multiple 3D images to be taken which can be formed into a video/animation showing the changing structure of the enamel as time progresses.

This process is not possible with the transmissometer, as the nature of the system involves the beam passing through the entire sample. If de-mineralisation occurred (assuming the 5 hour period was enough) then changes in the refractive index would only be for the very top layer of the enamel. Because of this, the majority of the enamel sample would be unchanged as far as the transmissometer is concerned since this is what the beam is passing through. In my opinion, if changes in the refractive index are to be detected due to de-mineralisation, samples which are much thinner should be provided, preferably without any surrounding resin. The samples should also be identical in diameter to the sample holder where the beam waist lies.

2) Frequency range:

Refractive index usually is measured at the peaks and troughs of the transmittance graphs. The number of peaks present in the transmittance graph will be greater if:

- 1) The sample is thinner.**
- 2) If its permittivity is higher.**

Proof of this is the transmittance graphs of the ceramic sample (**Figure 81**), the phantom (**Figure 43**) and an enamel sample (**Figure 73**). The ceramic sample had a thickness of 1.4 mm (and a very high permittivity) and showed the most peaks in its transmittance graphs. The phantom sample, even though it had a much lower permittivity than the ceramic sample showed 2 peak transmittance amplitudes and 2 trough amplitudes due to its 1.863 mm thickness. All of the enamel samples were around 4 mm thick and for most of them only one peak was present, if any. To view more peaks the samples have to be tested for a wider range of frequencies, since the transmittance of most samples will have peaks of decreasing amplitude occurring after the same frequency period such as that for a 2.77 mm FB6H ferrite sample shown in Figure 6.8 (page 143) of [75].

All of the enamel samples were tested only in the W band (75 - 110 GHz) for this project and the only solution was to calculate the refractive index for every complex transmittance value at every frequency. This is why the refractive index was varying significantly even for a single measurement.

Increasing the frequency range and decreasing the enamel samples' thickness would, combined, result in more peak transmittance amplitudes to be present, enabling accurate refractive index measurements to take place.

3) System stability + standing waves:

VNA's are capable of very accurate and precise measurements, especially the type used in this project (**Agilent N5244A PNA-X**). However, this is only if correct measures are taken to reduce system instability due to the three types of error associated with the VNA which are: **systematic** errors, **random** errors and **drift** errors.

Systematic errors are errors that are due to the imperfections in the measurement system. One of the reasons that cause this kind of error, for example, is cross talk. Cross talk is when signals that haven't passed through the material are detected at the transmitted signal detector. Systematic errors can be removed by calibration and because calibration was performed at the beginning of all experiments, as shown in **Figure 35**, it is possible to rule out systematic errors affecting the results in this report.

Random errors, which can't be corrected by calibration, are due to instrument noise. According to **[72]**, random errors can be minimised by taking multiple measurements and taking the average of it. This was done for all the experiments by letting the VNA do the frequency sweep in "Continuous" mode for at least 3 times after the sample is placed and then "holding" the fourth sweep results.

Drift errors are errors that are due to changing working conditions (after the calibration is performed) such as connector movements or temperature variations. These errors can be minimised by re-calibrating the VNA throughout the measurement duration before every measurement **[91]**. For experiment 4 this was performed, thanks to advice from the lab technician who was supervising me. Since measurements were taken every half an hour to give time for the acid to act on the enamel, a calibration was done to accommodate for any changes in the working conditions in those 30 mins.

Looking at the results of experiments 3 and 4, (**Figures 58** and **73** respectively), S_{21} results (hence measured transmittance graphs) showed a lot of oscillations which was why the results had to be smoothed before using them in the programs. I referred to this previously as "noisy" and even though these frequent variations in the magnitude and phase graphs partly eliminated after smoothing, still has a great effect on the measurements especially for samples 1 and 2 in experiment 4.

Observing the transmittances of the scattering phantom and ceramic sample for example, the relative smoothness of the measured transmittance is clear in both the amplitude and the phase graphs. In experiment 3, the transmittance magnitude showed a lot of "noisy" oscillations. In experiment 4, all of the samples showed oscillations in the transmittance magnitude, in addition to oscillations in the phase data between 95 and 100 GHz for sample 1 and between 100 and 105 GHz for sample 2 (**Figure 77**). As shown in the previous section, this had a significant effect on the

refractive index value between these frequencies even after the transmittance data was smoothed to mitigate this error.

The reason behind this is unclear and the research assistant mentioned that drift errors could be responsible for this. Another possible source of these oscillations which I read in [75] is the presence of standing waves due to the multiple reflections of the beam from the sample and its interference with the incident beam at every reflection. One measure that can be taken to reduce this error is to introduce **directional couplers**, which work to stop the occurrence of standing waves by attenuating the reflected signals. In the “Z bench” setup used for experiments 3 and 4 directional couplers weren’t present. Experiments 1 and 2 in which the phantom and 3 sound enamel samples were measured took place while the transmissometer was being used for other measurements. It is possible that the set-ups used for these measurements included directional couplers. The figure below shows another type of set-up for the quasi-optical circuit which includes directional couplers.

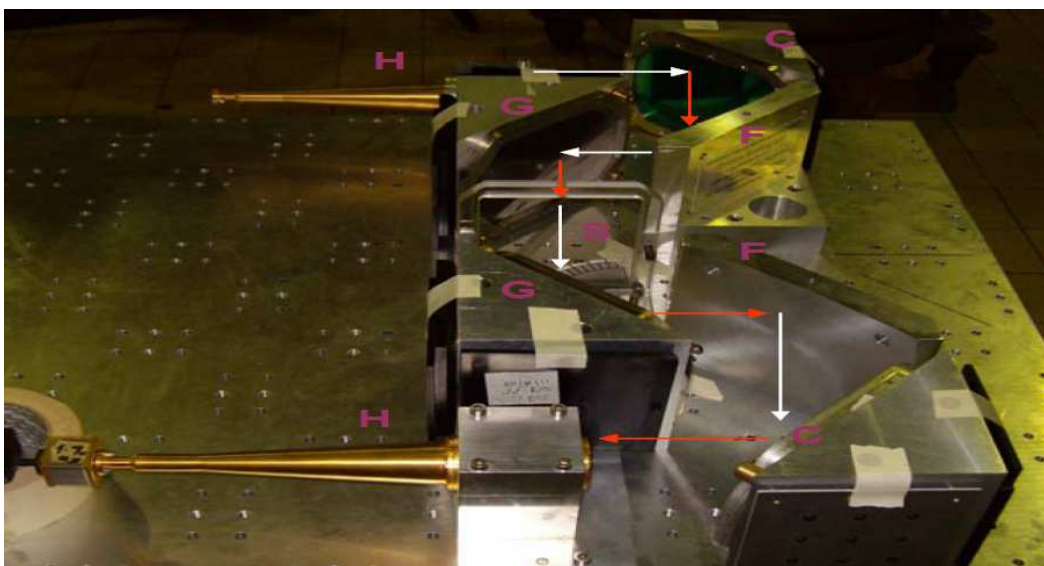


Figure 85 [75]: A photo of another quasi-optical circuit set-up used in another experiment where the material studied was a ferrite plate. **C** is a -12 dB quasi-optical directional coupler which is the component that is not present in the “Z bench” set-up used in this project (possibly present for only experiments 1 and 2). **F**, **G** and **H** are the ellipsoidal reflectors, wire grid polarisers and corrugated feed horns respectively. These components are also present in the “Z-bench” set-up used in this project.

According to [92], the VNA should be “warmed up” for a suitable amount of time before measurements take place in order for it to become stable. In experiments 3 and 4 measurements were taken soon after the VNA was switched on compared to experiments 1 and 2 in which the VNA was on for a longer amount of time due to the presence of other people using it for measurements beforehand. As mentioned in the previous section, I wasn’t present for the first 2 experiments due to the system being used for other measurements at the time. The samples were tested at the end of the day when the other measurements were finished and thus the VNA had been on for a long time before measurements took place. Not allowing the VNA to warm up and stabilise is the reason why I think that the noise in experiments 3 and 4 was present.

It may be possible to rule this out for experiment 4 in which the VNA was on for a duration of 5 hours and the last results showed the same oscillations as the first ones.

4) Polarisation:

Every material reacts differently to different polarisations of an electromagnetic signal and only experiments can tell the difference. In this experiment, a horizontal wire grid polariser was used which left the beam passing through the sample to be purely vertically polarised. It could be possible that trying a different beam polarisation would trigger a different polarisation response from the enamel which could alter its transmittance and refractive index.

5) Sample tilting/rotation:

In all the experiments I tried my best not to tilt the sample in the holder in order to not affect how the incident beam “sees” it. This includes aligning the sample with holes on the sides of the sample holder as shown in **Figure 69**. According to [72], tilting the sample only affects S_{11}/S_{22} (reflectance-based) measurements and doesn’t have an effect on transmittance based measurements (illustrated below):

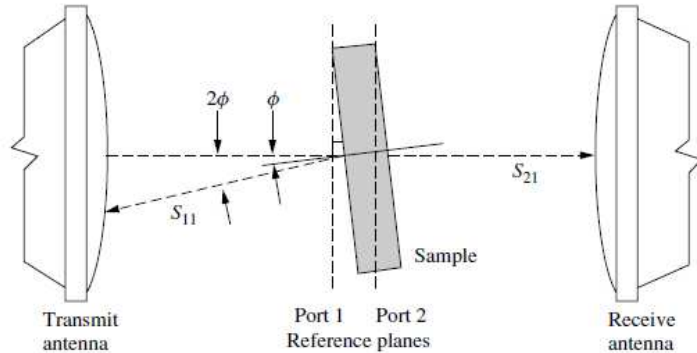


Figure 86 [93]: Schematic diagram of reflected and transmitted waves when the sample is translated and rotated from the reference planes defined during calibration.

Although this might be true for other materials, the samples which were studied in this project were not purely enamel and tilting/rotating them may change the percentage of the beam passing through the enamel (middle part) compared to the surrounding resin.

Conclusion

The final conclusion of this report is that **the transmissometer wasn't able to detect changes in the refractive index of enamel due to de-mineralisation of acid for up to 5 hours of it being left on the samples**. Due to the heavy booking of the transmissometer throughout the second semester, which according to the project plan at the start of the year was to be used entirely for multiple experiments, only 4 experiments (of which only 2 involved de-mineralisation) were carried out.

The contribution of this project to the dental erosion research into quantifying mineral loss is that the 4 experiments which were carried out have enabled potential reasons as to why the changes couldn't be detected to be identified. These reasons/opinions are detailed in the "Discussion/Analysis of Results section" and the main potential issues are summarised below. Another contribution which mainly gained the interest of the post-doctoral research assistant in the Antenna and Electromagnetics research group who supervised the experiments was the "**dispersive_perm_calc.m**" Matlab script which I wrote based on the least-squares approximation technique and thanks to other ideas and hints that he gave me. This code could possibly be used in the future for characterising materials without using Matlab's non-linear regression or curve fitting tools. I infer this from him asking me to visit his office some time to give him a brief overview on the specifications in terms of the input variables of the programs which are included in the "Supporting materials" document attached with this report.

The **main issues** which might be the reason that the transmissometer was unable to detect refractive index changes in the de-mineralised enamel samples are:

- The **samples being too thick** causing the acid to act only on the top, visible surface of the enamel and thus allowing the remaining majority of the enamel to be left unchanged.
- The **non-visibility of maxima and minima in the measured transmittance magnitude graphs** to enable the accurate measurement of the complex refractive index at the frequencies at which these peaks and troughs are present. This was due to two main reasons:
 - **Using only the W band** (75 - 110 GHz) in the experiments. Increasing the measurement bandwidth will allow the subsequent peaks and troughs to become visible.
 - The samples having a low permittivity and a relatively large thickness (≈ 4 mm) to the thickness of other materials with similar permittivity that showed visible maxima and minima. Using thinner samples will allow the subsequent peaks and troughs to become visible. A low permittivity is a property of the material and can't be changed.
- The **absence of quasi-optical directional couplers** in the test bench set-ups used for the experiments. Relatively thick samples result in more multiple reflections of the incident beam from the sample due to the presence of more "optical" layers. The "noisy" results obtained for experiments 3 and 4 played a major role in affecting the accuracy of the refractive index results. The oscillations in the transmittance graphs are most likely due to the **presence of standing waves** that result from the multiple reflections and the incident beam.

These factors are the most important factors carried on from the previous section in which other possible factors were more or less ruled out, although taking the other possible reasons which are not mentioned above into consideration is crucial if future work in this area is to be continued.

FUTURE WORK

If future work is to be conducted in this area in the future, the main reasons for the inability of the system to pick up mineral content changes which are mentioned above should be addressed first in order to find out which of the reasons is correct. If a reason is identified from these main points, the other sources of error discussed in the previous section should also be taken into account when taking measurements. The issues which are presented on the previous page could have been investigated in this project if there was more time for experiments using the QO circuit.

The first thing to be done (in my opinion) is to incorporate directional couplers in the QO circuit, obtain thinner enamel samples (preferably without the surrounding resin) and repeat the measurements across the whole 50 - 325 GHz range. In the case that resolving one or more of these issues results in the ability of the transmissometer to detect mineral content changes in enamel samples, both **repeatability** and **uncertainty analysis** should be carried out.

Repeatability is making sure that the results obtained are not “fluke” results and can be repeated to produce similar/close results whenever the process is repeated.

Uncertainty analysis comes after repeatability of the results is proven and can be done in the form of estimating the effects of all sources of error on the final refractive index results (errors can carry on through the stages) and including them in the final graphs in the form of +/- error bars.

After these two steps are completed then it will be possible to start comparing with OCT data and working towards methods of quantifying the mineral loss due to caries/erosion as accurately as possible across both systems. It will be good if the samples are studied simultaneously with both systems, i.e. taking a measurement (after the acid has acted for some time) with the transmissometer and then directly obtaining an image of it using OCT.

References

1. Hariri et al. (2012), 'Estimation of the Enamel and Dentin Mineral Content from the Refractive Index', *Caries Research*, vol. 47, pp. 18-26.
2. Top 10 Common Dental Problems. [ONLINE] Available at: <http://dentistry.about.com/od/toothmouthconditions/tp/10-Common-Dental-Problems.htm>.
3. University of Maryland Medical Centre: English Medical Reference Encyclopaedia, Dental Cavities. On-line. Available: <http://www.umm.edu/ency/article/001055.htm>
4. Tooth Decay-NHS Choices. On-line. Available: <http://www.nhs.uk/conditions/Dental-decay/Pages/Introduction.aspx>
5. Tooth decay 'third most common reason for children to be admitted to hospital' - Telegraph. [ONLINE] Available at: <http://www.telegraph.co.uk/health/healthnews/4699838/Tooth-decay-third-most-common-reason-for-children-to-be-admitted-to-hospital.html>.
6. Ouyang Yong (Dental Caries). Department of Endodontics and Operative Dentistry, Sun Yat-sen University.
7. Patricia Zuk (Dentin, Enamel, Pulp). WLAC-Human Physiology Courses
8. Nauman Bari Khan (2012), 'Early identification of carious lesions of enamel using Optical Coherence Tomography', M.Sc. thesis, Queen Mary University of London.
9. Wiley [ONLINE] Library: Oral Hygiene Products. On-line. Available: [http://\[ONLINE\]library.wiley.com/doi/10.1002/14356007.a18_209/full](http://[ONLINE]library.wiley.com/doi/10.1002/14356007.a18_209/full)
10. Steel J. & Lader D. (2003), 'Social factors and oral health in children', *National statistics*.
11. What are the Differences between Tooth Erosion and Tooth Decay? - Dental Conditions and Diseases. [ONLINE] Available at: <http://www.dental.net/tooth-erosion-and-tooth-decay/>.
12. Dental Erosion - Symptoms & Causes of Tooth Enamel Erosion. [ONLINE] Available at: <http://users.forthnet.gr/ath/abyss/Dental-Erosion-01.htm>.
13. Caring for your teeth | Bupa UK. [ONLINE] Available at: <http://www.bupa.co.uk/individuals/health-information/directory/d/caring-for-your-teeth>.
14. Lussi A. (2006), 'Dental Erosion From Diagnosis To Therapy', *Monographs in oral science*, vol. 20.
15. Fathimani K. (2009), 'Diagnosis, Risk Factors and Management of Dental Erosion: An Evidence Based Report',.
16. Amaechia B.T. & Highamb S.M. (2005), 'Dental erosion: possible approaches to prevention and control', *J. dentistry*, vol. 33, pp. 243 - 252.

17. Amaechia B.T. (2009), 'Emerging technologies for diagnosis of dental caries: The road so far', *J. app. phys.*, vol. 105.
18. Thomas S. S. (2009), 'Spectroscopic Investigation of Tooth Caries and Demineralization', *Doctoral thesis, Cochin University of Science and Technology*.
19. Tooth decay (Dental caries or cavities) - Causes-Prevention-Treatment. [ONLINE] Available at: <http://users.forthnet.gr/ath/abyss/dep1241.htm>.
20. Tell me about - Veneers . [ONLINE] Available at: <http://www.dentalhealth.org/tell-me-about/topic/cosmetic-dentistry/veneers>.
21. Tell me about - Dental erosion . [ONLINE] Available at: <http://www.dentalhealth.org/tell-me-about/topic/children-s-teeth/dental-erosion>.
22. BBC - Health: Diet and dental health . [ONLINE] Available at: http://www.bbc.co.uk/health/treatments/healthy_living/nutrition/dietary_dental.shtml.
23. E. Lynch and L. Abu-Naba'a, *Dental Products News Journal*, November 21, 2005.
24. J. Yang and V. Dutra, *Dent. Clin. North Am.* 49, 739 (2005).
25. A. T. Stodt, *Schweiz Monatsschr Zahnmed* 114, 882 (2004).
26. D. A. Young, *Gen. Dent.* 50, 320 (2002).
27. S. Keem and M. Elbaum, *IEEE Trans. Med. Imaging* 16, 653 (1997).
28. A. Schneiderman, M. Elbaum, T. Shultz, S. Keem, M. Greenebaum, and J. Driller, *Caries Res.* 31, 103 (1997).
29. D. A. Young and J. D. Featherstone, *J. Am. Dent. Assoc.* 136, 1682 (2005).
30. E. de Josselin de Jong, *Caries Res.* 29, 2 (1995).
31. S. Al-Khateeb and C. M. Forsberg, *Am. J. Orthod. Dentofacial Orthop.* 113, 595 (1998).
32. A. G. Ferreira Zandoná, R. L. Isaacs, M. H. van der Veen, and G. K. Stookey, in *Early Detection of Dental Caries II: Proceedings of the 4th Annual Indiana Conference*, Indianapolis, IN, USA, edited by G. K. Stookey (Indiana University, Bloomington, 2000), pp. 219–230.
33. J. P. van Amerongen, C. Penning, E. A. Kidd, and J. M. ten Cate, *Caries Res.* 26, 89 (1992).
34. E. H. Verdonschot, E. M. Bronkhorst, and A. Wenzel, *Community Dent. Oral Epidemiol.* 19, 329 (1991).
35. C. M. Pine and J. J. ten Bosch, *Caries Res.* 30, 381 (1996).
36. E. H. Verdonschot, E. M. Bronkhorst, R. C. Burgersdijk, K. G. Konig, M. J. Schaeken, and G. J. Truin, *Caries Res.* 26, 59 (1992).

- 37.** D. N. Ricketts, E. A. Kidd, P. J. Liepins, and R. F. Wilson, *Caries Res.* 30, 148 (1996).
- 38.** H. Ciaburro, D.M.D. and Krause & Al, *Occclusal caries detection in posterior teeth: An in vivo comparison of D-Carie and DIAGNOdent, sponsored study by NEKS Technologies, Inc.*
- 39.** B. T. Amaechi and A. Podoleanu, *J. Biomed. Opt.* 8, 642 (2003).
- 40.** B. T. Amaechi and A. Podoleanu, *Oral Health Prev. Dent.* 2(4), 377 (2004).
- 41.** B. T. Amaechi and A. Podoleanu, *Laser Phys.* 13, 703 (2003).
- 42.** B. T. Amaechi, A. G. Podoleanu, G. Komarov, S. M. Higham, and D. A. Jackson, *Proc. SPIE* 4610, 100 (2002).
- 43.** <http://www.idmos.com/>.
- 44.** L. Nicolaides, A. Mandelis, and S. H. Abrams, *J. Biomed. Opt.* 5, 31 (2000).
- 45.** F. Harter-Neto, A. Wenzel, and E. Gotfredsen, *Dentomaxillofac Radiol.* 37, 18 (2008).
- 46.** Tomlins P. H. & Wang R. K. (2005), 'Theory, developments and applications of optical coherence tomography', *J. Phys. D Appl. Phys.*, vol. 38, no. 15, pp. 2519 - 2535.
- 47.** Tomlins P. H. et al. (2011), 'Femtosecond laser micro-inscription of optical coherence tomography resolution test artifacts' *Biomedical Optics Express*, vol. 2, no. 5, pp. 1319 - 1327.
- 48.** M. R. Hee, J. A. Izatt, E. A. Swanson, D. Huang, J. S. Schuman, C. P. Lin, C. A. Puliafito, and J. G. Fujimoto, "Optical coherence tomography of the human retina," *Arch. Ophthalmol.* 113(3), 325–332 (1995)
- 49.** St. Jude Medical to Acquire LightLab Imaging for \$90M in Cash -Optical Coherence Tomography News. [ONLINE] Available at: <http://www.octnews.org/articles/2047898/st-jude-medical-to-acquire-lightlab-imaging-for-90/>.
- 50.** M. T. Tsai, H. C. Lee, C. W. Lu, Y. M. Wang, C. K. Lee, C. C. Yang, and C. P. Chiang, "Delineation of an oral cancer lesion with swept-source optical coherence tomography," *J. Biomed. Opt.* 13(4), 044012 (2008)
- 51.** P. H. Tomlins et al, *National Physical Laboratory Report OP 2* (2009)
- 52.** Woolliams P. D. and Tomlins P. H. (*The modulation transfer function of an optical coherence tomography imaging system in turbid media*). 2011. *Phys. Med. Biol.* 56, pp.2855-2871
- 53.** Costas P. et al (2000). *Optical Coherence Tomography: An Emerging Technology for Biomedical Imaging and Optical Biopsy*. *Neoplasia.* 2 (1-2), p9-25
- 54.** A F Fercher et al (2003). *Optical coherence tomography—principles and applications*. *Rep. Prog. Phys.* 66, pp.239-303

- 55.** Schmitt J M, *Optical Coherence Tomography (OCT): A Review*: *IEEE Journal of Selected Topics in Quantum Electronics*, 1999, Vol. 5 No. 4
- 56.** Knuttel A, Bonev S, Knaak W: *New method for evaluation of in vivo scattering and refractive index properties obtained with optical coherence tomography*. *J Biomed Opt* 2004; 9: 265–273.
- 57.** Khijmatgar S. (2011), 'Optical Coherence Tomography of Bone', M.Sc. thesis, Queen Mary University of London.
- 58.** Khan N. B. (2011), 'Early identification of carious lesions of enamel using Optical Coherence Tomography', M.Sc. thesis, Queen Mary University of London.
- 59.** HP Test and Measurement Application Note 95-1: S-Parameter Techniques. On-Line. Available: <http://www.sss-mag.com/pdf/an-95-1.pdf>
- 60.** Polar Instruments: An Introduction to S-Parameters. On-Line. Available: www.polarinstruments.com/support/cits/s_parameters.ppt
- 61.** Exam-Crazy: S-Parameters and the Scattering Matrix On-Line. Available: http://examcrazy.com/Engineering/Electronics-Communication/S_Parameters_and_the_Scattering_Matrix.asp
- 62.** Agilent Technologies, Products and Services: Network Analyzers On-Line. Available: <http://www.home.agilent.com/en/pd-1654283-pn-N5244A/pna-x-microwave-network-analyzer?&cc=GB&lc=eng>
- 63.** S. Chen et al, *High-Resolution High-Power Quasi-Optical Free-Space Spectrometer for Dielectric and Magnetic Measurements in Millimetre Waves*: *IEEE Transactions on Instrumentation and Measurement*, 2009, Vol. 58 No. 8
- 64.** S. Chen et al, *A High-Resolution Quasi Optical Spectrometer for Complex Permittivity and Loss Tangent Measurements at Millimetre Wavelengths*: *Instrumentation and Measurement Technology Conference Proceedings*, 2007
- 65.** Agilent Millimetre-Wave Network Analyzers 10 MHz to 110 GHz, with Extensions to 1.1 THz: Technical Overview
- 66.** Agilent Technologies, Products and Services: Millimetre-Wave Controllers On-Line. Available: <http://www.home.agilent.com/en/pd-1392552-pn-N5262A/millimeter-wave-controller-for-pna-x-network-analyzer-series-4-port-measurements?&cc=GB&lc=eng>
- 67.** Agilent Technologies N5261A and N5262A User's and Service Guide: Millimetre Head Controller
- 68.** Agilent N5244A and N5245A 2-Port and 4-Port PNA-X Microwave Network Analyzers (10 MHz - 43.5 GHz) (10 MHz - 50 GHz): Service Guide
- 69.** Dielectrics. [ONLINE] Available at: <http://hyperphysics.phy-astr.gsu.edu/%E2%80%8Chbase/electric/dielec.html>.

- 70.** Shvets G. & Urzhumov Y. A. (2005), 'Electric and magnetic properties of sub-wavelength plasmonic crystals', *J. Opt. A: Pure Appl. Opt.*, vol. 7, no. 2.
- 71.** Magnetic Materials - Microwave Encyclopedia - Microwaves101.com. [ONLINE] Available at: <http://www.microwaves101.com/encyclopedia/magneticmaterials.cfm>.
- 72.** L. F. Chen, C. K. Ong, C. P. Neo, V. V. Varadan and V. K. Varadan, (2004). *Microwave Electronics Measurement and Materials Characterization*. 1st ed. England: John Wiley & Sons Ltd.
- 73.** Agilent Basics of Measuring the Dielectric Properties of Materials: Application Note. [ONLINE] Available at: <http://www3.imperial.ac.uk/pls/portallive/docs/1/11949698.PDF>.
- 74.** Begley S., 'Electromagnetic Properties of Materials: Characterization at Microwave Frequencies and Beyond'.
- 75.** Yang B. (2008), 'Assessment of Magnetic Material for Use in Quasi-optical Non-reciprocal Devices Operating at Frequencies above 90 GHz', Ph.D. thesis, Queen Mary University of London.
- 76.** Balanis C. A. (2005). *Antenna Theory: Analysis and Design*. 3rd ed. England: John Wiley & Sons Ltd.
- 77.** Musil J. & Žáček F. (1986), 'Microwave measurements of complex permittivity by free space methods and their applications', *Elsevier-Technology and Engineering*, vol. 22.
- 78.** McGraw-Hill Encyclopaedia of Science and Technology (5th ed.). McGraw-Hill. 1993.
- 79.** Max Born, 1999. *Principles of Optics: Electromagnetic Theory of Propagation, Interference and Diffraction of Light*. 7th Edition. Cambridge University Press.
- 80.** Physics of Light and Optics. Justin Peatross and Michael Ware (2008)
- 81.** Goldsmith (1998), 'Quasioptical Systems', 1st Edition, Springer.
- 82.** [ONLINE] Available at: http://upload.wikimedia.org/wikipedia/commons/a/a9/Laser_gaussian_profile.svg.
- 83.** [ONLINE] Available at: <http://optics.hanyang.ac.kr/~shsong/27-Gaussian%20beams.pdf>.
- 84.** [ONLINE] Available at: <http://www.jimani-inc.com/Portals/68377/images/Fiber-laser-system-beam-waist-resized-600.png>.
- 85.** P. J. B. Clarricoats (1984), 'Corrugated Horns for Microwave Antennas (IEEE Electromagnetic Waves Series)', *The Institution of Engineering and Technology*.
- 86.** Corrugated Horns. [ONLINE] Available at: http://www.terahertz.co.uk/index.php?option=com_content&view=article&id=141&Itemid=444.

- 87.** *Quasi-Optics*. [ONLINE] Available at:
<http://www.eecs.qmul.ac.uk/group/antennas/facilities/Quasi-Optics.html>.
- 88.** *Agilent VNA Quasi-Optical Systems*. [ONLINE] Available at:
http://www.terahertz.co.uk/index.php?option=com_content&view=article&id=135&Itemid=438.
- 89.** *Polarisers*. [ONLINE] Available at:
http://www.terahertz.co.uk/index.php?option=com_content&view=article&id=211&Itemid=538#wire_grid.
- 90.** <http://www.voumard.ch/>
- 91.** *Understanding VNA Calibrations*. [ONLINE] Available at:
http://na.tm.agilent.com/plts/help/WebHelp/VNACalAndMeas/Understanding_VNA_Calibrations.html.
- 92.** *Vector Network Analyzer Calibration - Developer Zone - National Instruments*. [ONLINE] Available at: <http://www.ni.com/white-paper/14114/en>.
- 93.** Hollinger R. D. et al. (1991), 'Free-space, broadband measurements of high-temperature, complex dielectric properties at microwave frequencies', *IEEE Trans. Inst. Meas.*, vol. 40, no. 5, pp. 842 - 846.